THESIS FOR THE DEGREE OF DOCTOR OF PHILOSOPHY

Development of high-T_c SQUID magnetometers for on-scalp MEG

MINSHU XIE

CHALMERS

Department of Microtechnology and Nanoscience - MC2
CHALMERS UNIVERSITY OF TECHNOLOGY
Göteborg, Sweden 2017

Development of high-T_c SQUID magnetometers for on-scalp MEG
MINSHU XIE
ISBN 978-91-7597-642-6

Doktorsavhandlingar vid Chalmers tekniska högskola
Ny serie nr 4323
ISSN 0346-718X

Quantum Device Physics Laboratory
Department of Microtechnology and Nanoscience - MC2
Chalmers University of Technology
SE–412 96 Göteborg
Sweden
Telephone +46 (0)31-772-1000

ISSN 1652-0769
Technical report MC2-374

Chalmers Reproservice
Göteborg, Sweden 2017

Development of high-T_c SQUID magnetometers for on-scalp MEG

MINSHU XIE
Department of Microtechnology and Nanoscience - MC2
Chalmers University of Technology
Göteborg, Sweden 2017

Abstract

This thesis describes the development of high critical temperature superconducting quantum interference device (high-T_c SQUID) magnetometers based on bicrystal grain boundary and nanowire junctions for the potential use in on-scalp magnetoencephalography (MEG), which is a new generation MEG technique with reduced sensor-to-subject standoff distances.

MEG is a method of mapping neural dynamics in the human brain by recording the magnetic fields produced by neural currents. Its passive and non-contact nature allows doctors and neuroscientists to safely and effectively carry out clinical diagnoses and scientific research on the human brain. State-of-the-art MEG systems utilize low-T_c SQUID sensors with sensitivities of 1–5 fT/$\sqrt{}$Hz down to 1 Hz to measure the extremely tiny biomagnetic fields (∼100 fT) from the brain. However, low-T_c SQUIDs require liquid helium cooling to reach their operating temperature ($<$ 10 K). The complicated cryogenics limit the sensor-to-subject distance to 20 mm at best.

On-scalp MEG, where sensors are placed with close proximity (few millimeters) to the scalp of the subject, can be realized with the aid of helium-free MEG sensor technologies. In this thesis, we designed, fabricated and characterized high-T_c SQUID magnetometers made from $YBa_2Cu_3O_{7-x}$ (YBCO) that can operate with liquid nitrogen cooling (77 K) based on bicrystal grain boundary or nanowire junctions. Single-layer bicrystal devices with a directly connected pickup loop were demonstrated to have a magnetic flux noise of 5 $\mu\Phi_0/\sqrt{}$Hz with an effective area of 0.24 mm^2, giving a magnetic field sensitivity of 40 fT/$\sqrt{}$Hz at 77 K. For nanowire-based devices, a two-level coupling approach was implemented, where the flip-chip SQUID is connected to a washer-type pickup loop with the inner hole size matching that of a flux transformer input coil. This improved the effective area of nanowire-based SQUID magnetometers to 0.46 mm^2. Combining with the magnetic flux noise of 55 $\mu\Phi_0/\sqrt{}$Hz for this type of devices, the best magnetic field sensitivity obtained was 240 fT/$\sqrt{}$Hz at 77 K. A simulation method was developed and demonstrated to give an accurate evaluation of the effective area and inductances in the design of SQUID magnetometers. Using this method, nanowire-based SQUID magnetometers with thick washers were predicted to give an improved effective area of 2.2 mm^2.

A single-channel high-T_c MEG system housing the 40 fT/$\sqrt{}$Hz bicrystal grain boundary SQUID magnetometer was used to benchmark against low-T_c SQUIDs in a state-of-the-art MEG system (Elekta Neuromag® TRIUX, courtesy of NatMEG) based on recordings on a head phantom. It was shown that the expected amplitude gain of magnetic field signals associated with the on-scalp sensors (reduced standoff distances to ∼3 mm) can be obtained while the single-channel signal-to-noise ratio was still lower than its low-T_c counterpart. Also a systematic benchmarking procedure that is objective, fast, and feasible for application to various on-scalp MEG sensing technologies was established. The functionality of this procedure was proved with MEG recordings of auditory and somatosensory evoked fields (AEFs and SEFs, respectively) on one human subject.

Keywords: Bicrystal grain boundary, nanowire junctions, high-T_c SQUIDs, YBCO, magnetometers, magnetoencephalography, on-scalp MEG.

List of appended papers

This thesis is based on the work contained in the following papers:

I **Improvement of ultra-low field magnetic resonance recordings with a multilayer flux-transformer-based high-T_c SQUID magnetometer**
M. Chukharkin, A. Kalabukhov, J. F. Schneiderman, F. Öisjöen, M. Jönsson, M. Xie, O. V. Snigirev and D. Winkler
IEEE Trans. Appl. Supercond., **23**, 1602404 (2013).

II **High-T_c SQUID vs. low-T_c SQUID-based recordings on a head phantom: benchmarking for magnetoencephalography**
M. Xie, J. F. Schneiderman, M. Chukharkin, A. Kalabukhov, S. Whitmarsh, D. Lundqvist and D. Winkler
IEEE Trans. Appl. Supercond., **25**, 1601905 (2015)

III **Benchmarking for on-scalp MEG sensors**
M. Xie, J. F. Schneiderman, M. Chukharkin, A. Kalabukhov, B. Riaz, D. Lundqvist, S. Whitmarsh, M. Hämäläinen, V. Jousmäki, R. Oostenveld and D. Winkler
IEEE Trans. Biomed. Eng., **64**, 1270–1276 (2017)

IV **Feedback solutions for low crosstalk in dense arrays of high-T_c SQUIDs for on-scalp MEG**
S. Ruffieux, M. Xie, M. Chukharkin, C. Pfeiffer, A. Kalabukhov, D. Winkler and J. F. Schneiderman
Supercond. Sci. Technol., **30**, 054006 (2017)

V **Improved coupling of nanowire-based high-T_c SQUID magnetometers - simulations and experiments**
M. Xie, M. Chukharkin, S. Ruffieux, J. F. Schneiderman, A. Kalabukhov, M. Arzeo, T. Bauch, F. Lombardi and D. Winkler
Supercond. Sci. Technol., Accepted for publication, 2017

VI **Extraction of inductances and effective areas of single-layer and flip-chip nanowire-based high-T_c SQUID magnetometers**
M. Xie, M. Chukharkin, S. Ruffieux, J. F. Schneiderman, A. Kalabukhov, M. Arzeo, T. Bauch, F. Lombardi and D. Winkler
Manuscript to be submitted, 2017

Symbols and abbreviations

Table of symbols.

Symbol	Meaning
α_C	Asymmetry parameter of SQUID capacitances
α_R	Asymmetry parameter of SQUID resistances
α_I	Asymmetry parameter of SQUID currents
α_L	Asymmetry parameter of SQUID inductances
β_c	Stewart-McCumber parameter
β_L	Screening parameter
η	Damping coefficient
θ	XRD scattering angle
Λ	London parameter
λ_L	London penetration depth
$\lambda_L(0)$	London penetration depth at zero temperature
λ_P	Pearl penetration length
μ_0	Vacuum permeability
ξ	Coherence length
Φ	Magnetic flux
Φ_0	Magnetic flux quantum
ϕ	Phase
Ψ	Order parameter
ω_c	Characteristic frequency
τ	Normalized time
A_{eff}	Effective area

Symbol	Meaning
$\boldsymbol{B}$	Magnetic field vector
B	Magnetic field
B_c	Critical magnetic field
C	Capacitance
D_i	Inner dimension of the pickup loop
D_o	Outer dimension of the pickup loop
$\boldsymbol{E}$	Electric field vector
E	Electric field
e	Electron unit charge
G_{OS}	Benchmarking gain measure of on-scalp sensors
h	Planck constant
I_0	Maximum supercurrent
I	Current
I_n	Noise current
I_b	Bias current
I_c	Critical current
I_s	Supercurrent
i	Normalized current
$\boldsymbol{J}_S$	Superconducting current density vector
J_c	Critical current density
k_B	Boltzman constant
L	Inductance
L_J	Junction inductance
L_{SQ}	SQUID inductance
L_g	Geometric inductance
L_{in}^{FT}	Flux transformer input coil inductance
L_k	Kinetic inductance
L_{pk}^{SQ}	SQUID pickup loop inductance
L_{pk}^{FT}	Flux transformer pickup loop inductance
L_m	Galvanic mutual inductance
l	Nanowire length
M	Mass or magnetic momentum
M_i	Inductive mutual inductance
m_e	Electron mass
n_s	Number density of superconducting electrons
$\boldsymbol{Q}$	Current dipole vector

Symbol	Meaning
R	Resistance
$S_{\Phi}^{1/2}$	Amplitude spectral density of the flux noise
$S_{V}^{1/2}$	Amplitude spectral density of the voltage noise
$S_{Ve}^{1/2}$	Amplitude spectral density of the electronics voltage noise
$S_{B}^{1/2}$	Amplitude spectral density of the magnetic field noise
T	Temperature
T_c	Critical temperature
t	Nanowire thickness
U	Potential
V	Voltage
V_{Φ}	Voltage-to-flux transfer function
$\langle V \rangle$	Average voltage
v	Normalized voltage
v_{ϕ}	Normalized voltage-to-flux transfer function
w	Nanowire width

Table of abbreviations.

Abbreviation	Meaning
AEF	Acoustic evoked field
AFM	Atomic force microscope
ac	Alternating current
CMP	Chemical mechanical polishing
dc	Direct current
EEG	Electroencephalography
FLL	Flux-locked loop
fMRI	Functional magnetic resonance imaging
MEG	Magnetoencephalography
MRI	Magnetic resonance imaging
MSR	Magnetically shielded room
NatMEG	The Swedish national facility for magnetoencephalography
N20m	20 ms characteristic response in SEF
N100m	100 ms characteristic response in AEF
rf	Radio frequency
PET	Positron emission tomography
PLD	Pulsed laser deposition
SEF	Somatosensory evoked field
SEM	Scanning electron microscopy
SIS	Superconductor-insulator-superconductor
SNR	Signal-to-noise ratio
SPECT	Single-photon emission computed tomography
SQUID	Superconducting quantum interference device
STO	$SrTiO_3$
UV	Ultraviolet
YBCO	$YBa_2Cu_3O_{7-x}$

Contents

CHAPTER 1

Introduction

The development of modern neuroscience strongly relies on the progress of new instrumentation and functional neuroimaging techniques, such as functional magnetic resonance imaging (fMRI), electroencephalography (EEG), magnetoencephalography (MEG), positron emission tomography (PET) and single-photon emission computed tomography (SPECT) [1–3]. Among these methods, EEG and MEG are particularly suited to study cortical neuronal events thanks to their millisecond temporal resolution and noninvasive feature [4–6]. While EEG measures the electric potential differences on the scalp, MEG measures the weak magnetic field (∼50–500 fT) outside the brain generated by the same synchronous postsynaptic currents in the pyramidal neurons of the cerebral cortex [7, 8]. As compared to EEG signals, one most important advantage of MEG signals is that they are relatively undistorted and attenuated by the skull and scalp, especially for shallow sources [9, 10]. As a result, MEG can achieve millimeter spatial resolution.

The first MEG recording was carried out by David Cohen in 1968 with an induction-coil magnetometer to record the field produced by alpha-rhythm (∼10 Hz) neural currents [11]. However, the insufficient magnetometer sensitivity resulted in a poor signal-to-noise (SNR) ratio and therefore the MEG signals needed to be extracted by averaging with respect to the simultaneously recorded EEG signals as reference. The timely discovery of the flux quantization [12] and Josephson tunnelling [13] led to the advent of superconducting quantum interference devices (SQUIDs), which are extremely sensitive magnetic flux sensors [14, 15]. Using the much more sensitive SQUID magnetometer, Cohen managed in 1972 to record directly

alpha-rhythm without noise averaging [16]. Since then, SQUID-based MEG evolved quickly from single-channel instruments to multi-channel systems during the following two decades [17]. In 1992, the first whole-head MEG systems emerged [18–21]. Nowadays, state-of-the-art MEG systems incorporating several hundred SQUID sensors in helmet-shaped arrays are available from commercial suppliers like CTF MEG technology, Elekta (Neuromag® TRIUX) and Tristan Technologies (BabySQUID). These commercial MEG systems utilize SQUID sensors made from low critical-temperature (low-T_c) superconducting materials, such as niobium (T_c∼9 K). With the whole-wafer Nb/Al-AlO_x/Nb junction processes, integrated low-T_c SQUIDs containing multilayer structures can be fabricated on a large scale with high reproducibility and narrow spread of device parameters [22]. The typical spectral density of magnetic field noise for low-T_c SQUID magnetometers in state-of-the-art MEG systems is below 5 fT/$\sqrt{}$Hz down to 1 Hz [7].

However, low-T_c SQUIDs have to be operated at liquid helium temperatures (∼4 K) resulting in more complicated cryogenics and typically large sensor-to-scalp distances (>20 mm) [8]. Because the neuromagnetic field decays rapidly as a function of the distance to the source (i.e., neural currents in the brain), sensors are preferably placed as close as possible to the head. Recently, on-scalp MEG [23–29], in which sensors are placed in close proximity (few millimeters) to a subject's scalp, has received much attention. Potential on-scalp MEG sensor technologies include the high-T_c SQUID working at liquid nitrogen temperatures (∼77 K) [30–35], optically pumped magnetometer (OPM) [36–39] and diamond N-V center magnetometers [40]. These helium-free MEG sensor technologies are also economically desirable because commercial whole-head MEG systems boil off roughly 100 liters of liquid helium per week, the price for which is high and continues to grow [41]. The installation of re-liquefier systems can reduce the consumption of liquid helium. Nevertheless, this adds substantial investment costs and the liquefier may introduce both mechanical and magnetic noise.

In the scope of this thesis, the focus of developing sensors for the new-generation on-scalp MEG is put on high-T_c dc SQUID magnetometers. The most widely studied and used material for producing high-T_c SQUIDs is $YBa_2Cu_3O_{7-x}$ (YBCO). Practically used high-T_c SQUIDs are mainly fabricated from four types of Josephson junctions: bicrystal grain boundary junctions, step-edge grain boundary junctions, step-edge SNS junctions and ramp-edge Josephson junctions [22, 42–44]. While some of these technologies were shown to produce high-T_c SQUID magnetometers with sensitivities close to their low-T_c counterparts (<10 fT/$\sqrt{}$Hz at a few Hz at 77 K) [33, 45–47], the spread and application of high-T_c SQUIDs in MEG or general biomagnetism research are still limited. The main reason is that these high-T_c

junctions are relatively easy to fabricate on a small scale but mass production with a good reproducibility is challenging [48]. As stated, a whole-head MEG system typically consists of several hundred SQUID channels, where all channels should be roughly identical in performance.

At this stage, we shall introduce another type of Josephson junctions, i.e., constriction-type Josephson junctions (nanowires). Preceding attempts to fabricate high-T_c dc SQUIDs based on YBCO nanowires date back to the 1990s, where serveral groups demonstrated that these constriction-type junctions could show Josephson-like behavior provided that the nanowire dimensions (length l, width w and thickness t) are smaller than the Pearl penetration length $\lambda_P = \lambda_L^2/t$, where λ_L is the London penetration depth [49–51]. However, the reported flux noise level was about 80 $\mu\Phi_0/\sqrt{\text{Hz}}$ for a dc SQUID with 240 nm wide YBCO nanowires at 4.2 K [49], which was far from being adequate for biomagnetic applications. Recently, high-quality YBCO nanowires [52, 53] and high-T_c nanowire-based SQUIDs with magnetic flux noise <1 $\mu\Phi_0/\sqrt{\text{Hz}}$ at 8 K were realized [54]. This improved nanopatterning process is promising to be a scalable technology suitable for whole-head MEG systems. While such magnetic flux noise properties are impressive, the small size of the SQUID loop makes them very poor magnetic field sensors. The application areas of nanowire-based SQUIDs have mostly been limited to measuring magnetization reversal in small spin systems (e.g. magnetic nanoparticles) [55–57]. For practical applications that go beyond magnetic field sensitivity on the microscopic scale, coupling methods to achieve a larger effective sensing area ($A_{eff,SQ} = \Phi_{SQ}/B_a$, where Φ_{SQ} is the flux coupled into the SQUID in response to the applied field B_a) are required. The field coupling here is more challenging than for traditional grain boundary high-T_c SQUIDs due to e.g., small SQUID loop sizes, high kinetic junction inductances and thin SQUID washer thicknesses. In 2016, it was shown that introducing a pickup loop to a high-T_c nanowire-based SQUID can increase the effective area to 62 μm^2 while still having the magnetic flux noise below 2 $\mu\Phi_0/\sqrt{\text{Hz}}$ at 5 K, which corresponds to a magnetic field sensitivity of below 66 pT/$\sqrt{\text{Hz}}$ [58]. This field sensitivity can be further improved by enlarging the pickup loop dimension and the mutual inductance, L_m, between the SQUID and pickup loops. Beyond single-layer devices, multilayer/flip-chip devices with an inductively coupled flux transformer, similar to existing multilayer SQUID magnetometers [43, 47, 59], can also be implemented. As thus, nanowire-based high-T_c SQUID magnetometers are competitive candidate sensors for future generations of on-scalp MEG systems.

Thesis outline

The aim of this thesis is to demonstrate the developments made on approaching a new generation of on-scalp MEG system based on high-T_c SQUIDs. In Chapter 2, a brief overview of the background to superconductivity and SQUIDs is presented. The design, fabrication and performance characterization of our bicrystal high-T_c SQUID magnetometers are introduced. Chapter 3 continues to describe the research on designs and coupling methods to bring the sensitivity of nanowire-based high-T_c SQUID magnetometers toward the level of MEG applications. Results from both simulation and experiment are provided. Chapter 4 includes the relevant background to MEG and our benchmarking experiments on phantoms and humans with a bicrystal high-T_c SQUID-based MEG system and low-T_c SQUIDs in a state-of-the-art MEG system (Elekta Neuromag® TRIUX, courtesy of NatMEG) to reveal the benefits given by the reduced sensor-to-scalp distance allowed by high-T_c sensors. Chapter 5 summarizes the main results of the thesis and provides an outlook for future work.

CHAPTER 2

High-T_c SQUIDs

2.1 Superconductivity

Superconductivity was first discovered in 1911 by H. K. Onnes, soon after helium had been liquefied in the same laboratory in Leiden [60]. When it was cooled down to below 4.2 K, the electrical resistance of mercury abruptly dropped and disappeared. This transition temperature to a superconducting state with zero resistance is known as the critical temperature T_c, which is a characteristic property of superconducting materials. Later it is confirmed that about half the metals of the periodic table are superconductors, among which niobium has the highest $T_c \sim 9$ K [61–63]. In 1993, W. Meissner and R. Ochsenfeld observed that superconductors are not only perfect zero-resistance conductors but also perfect diamagnets, i.e., any magnetic field (less than the critical field B_c) originally present in a superconductor should be completely expelled when the sample is cooled down to below T_c [64]. This phenomenon is usually referred to as the Meissner effect.

Then in 1935, the brothers F. and H. London proposed two basic equations governing the electrodynamic properties of superconductors [65]:

$$\frac{\partial(\Lambda \boldsymbol{J}_S)}{\partial t} = \boldsymbol{E}, \tag{2.1}$$

$$\nabla \times (\Lambda \boldsymbol{J}_S)) = -\boldsymbol{B}, \tag{2.2}$$

where $\Lambda = m_e/n_s e^2$ is the London parameter (m_e is the electron mass, e is the unit charge and n_s is the number density of superconducting electrons),

$\boldsymbol{J}_S$ is the superconducting current density, $\boldsymbol{E}$ and $\boldsymbol{B}$ are respectively the electric and magnetic fields in the superconductor. The first London equation 2.1 describes the perfect conductivity, i.e., any electric field accelerates the superconducting electrons without resistance. The second London equation 2.2 can explain the perfect diamagnetism. Combining Eq. 2.2 with Ampere's law $\nabla \times \boldsymbol{B} = \mu_0 \boldsymbol{J}_S$ gives:

$$\nabla^2 \boldsymbol{B} = \frac{\boldsymbol{B}}{\lambda_L^2}, \tag{2.3}$$

where $\lambda_L = (m_e/\mu_0 n_s e^2)^{1/2}$ is the London penetration depth. Equation 2.3 implies that any applied magnetic field is completely excluded from the interior of a superconductor by screening currents flowing in a thin depth region near the sample surface and the London penetration depth describes the exponential decay length from the surface. The temperature dependence of λ_L can be empirically described by [66]:

$$\lambda_L(T) \approx \lambda_L(0)[1 - (T/T_c)^4]^{-1/2}, \tag{2.4}$$

where $\lambda_L(0)$ is the London penetration depth at zero temperature.

In the 1950s and 1960s, both the macroscopic Ginzburg-Landau theory [67] and the microscopic BCS theory [68] were developed, forming a complete theoretical picture of the conventional superconductors. According to the BCS theory, electrons with opposite spin and equal momentum near the Fermi surface can form bound pairs (Cooper pairs) through interaction with lattice vibrations (electron-phonon interaction) below the critical temperature. Because Cooper pairs are bosons, they may condense into the same quantum state through a Bose condensation and be described by a single wave function $\Psi(\boldsymbol{r})$ (the order parameter). The density of Cooper pairs is $n_s = |\Psi(\boldsymbol{r})|^2$. The properties of all known superconductors at that time can be well described by the BCS theory and a maximum critical temperature of about 30 K is predicted for elementary metals and binary compounds (low-T_c superconductors).

An important breakthrough in the field of superconductivity happened in 1986, when J. G. Bednorz and K. A. Müller discovered the first high-T_c superconductor Ba–La–Cu–O with a T_c of in the 30 K range [69]. Soon later the superconductivity in YBCO was discovered at $T_c = 93$ K [70], which aroused great enthusiasm as practical applications of superconductivity using liquid nitrogen as the refrigerant became possible. Since then many other similar cuprate materials have been found to be superconducting with T_c up to 135 K [71]. Among all the discovered high-T_c superconductors, YBCO has been studied the most and its physical properties and growth mechanisms are well understood. Most of the practical applications rely on YBCO and we also use it throughout this thesis work.

2.2 Josephson junctions

A Josephson junction is a weak link between two superconductors where the wave functions of the two superconductors slightly overlap and Cooper pairs can tunnel through. The weak links can be formed by insulating barriers, metal or semiconductor links, grain boundaries, narrow constrictions and damaged superconductors. In 1962, B. D. Josephson theoretically predicted that a superconducting current can flow through a superconductor-insulator-superconductor (SIS) junction without dissipation (no potential difference required) [13], which is known as the dc Josephson effect:

$$I_s = I_c sin\phi, \tag{2.5}$$

where I_c is the critical current (the maximum superconducting current that can sustain in the junction) and ϕ is the superconducting phase difference across the junction. He also predicted that when a dc voltage V is applied to a junction, the superconducting phase difference across the junction varies with time according to:

$$\frac{d\phi}{dt} = \frac{2e}{\hbar}V = \frac{2\pi}{\Phi_0}V, \tag{2.6}$$

where $\Phi_0 = h/2e \approx 2.07 \times 10^{-15}$ Wb is the flux quantum and $h = 2\pi\hbar \approx 6.63 \times 10^{-34}$ J·s is the Planck constant. Integrating Eq. 2.6 and substituting this phase-time dependence into Eq. 2.5 shows that an alternating current of amplitude I_c and frequency $2eV/h$ is present in the junction, which is known as the ac Josephson effect. Both effects were proved experimentally soon after the prediction of Josephson [72, 73].

The current–voltage (I–V) characteristics of Josephson junctions can be well described by the resistively and capacitively shunted junction (RCSJ) model [74, 75]. The equivalent circuit of this model is shown in Fig. 2.1 and the total current through the junction is a sum of the superconducting current I_s, the current V/R through the resistor R, the displacement current CdV/dt through the shunting capacitance C and the noise current I_n. Combining with Eq. 2.5 and Eq. 2.6, one can write:

$$I = C\frac{\Phi_0}{2\pi}\ddot{\phi} + \frac{1}{R}\frac{\Phi_0}{2\pi}\dot{\phi} + I_c sin\phi + I_n. \tag{2.7}$$

This equation describes the dynamics of the phase difference ϕ in analogy to the damped motion of a particle of mass $M = C \cdot (\Phi_0/2\pi)$ and damping coefficient $\eta = (1/R) \cdot (\Phi_0/2\pi)$ in the tilted washboard potential $U = (\Phi_0 I_c/2\pi) \cdot (1 - cos\phi - I/I_c \cdot \phi - I_n/I_c \cdot \phi)$ along the coordinate x, which is [76]:

$$M\ddot{x} + \eta\dot{x} = -\nabla U. \tag{2.8}$$

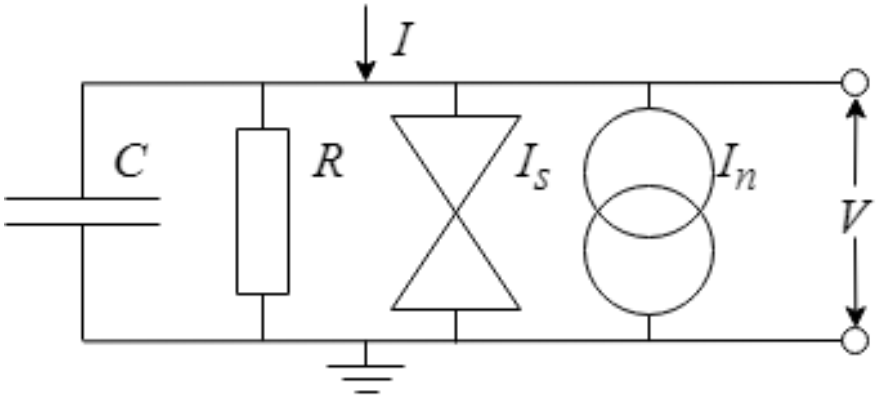

Figure 2.1: Equivalent circuit of the resistively and capacitively shunted junction.

By introducing the Stewart-McCumber parameter $\beta_c = 2\pi I_c R^2 C/\Phi_0$ and characteristic frequency $\omega_c = 2\pi I_c R/\Phi_0$, Eq. 2.7 can be written as [75]:

$$\beta_c \frac{\ddot{\phi}}{\omega_c^2} + \frac{\dot{\phi}}{\omega_c} = I/I_c - sin\phi - I_n/I_c. \tag{2.9}$$

In the absence of noise, the motion of the particle in the washboard potential can be discussed for the limits of $\beta_c \ll 1$ (overdamped) and $\beta_c \gg 1$ (underdamped).

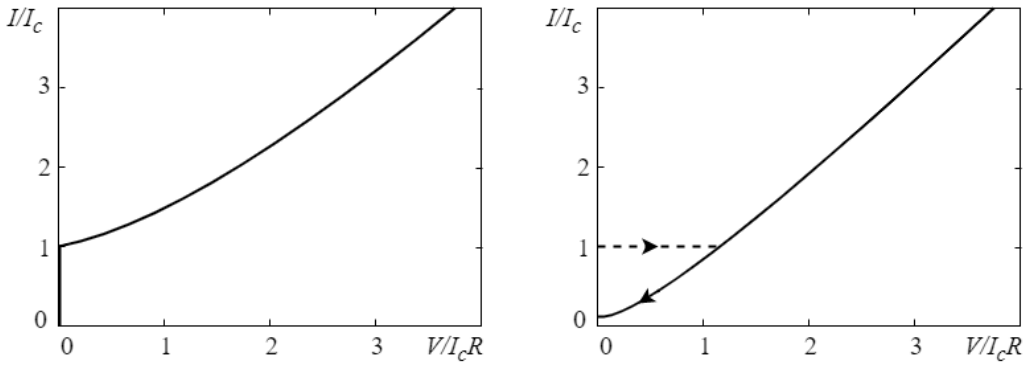

Figure 2.2: Normalized I–V characteristics: (a) non-hysteretic for an overdamped junction ($\beta_c \ll 1$) and (b) hysteretic for an underdamped junction ($\beta_c \gg 1$).

When $\beta_c \ll 1$, the inertial term in Eq. 2.9 is negligible and therefore the particle gets trapped in one of the potential minima as soon as the driving force is removed ($I < I_c$). This corresponds to a junction with a negligible capacitance and a non-hysteretic I–V characteristic, which is important for the application of SQUIDs. The actual I–V relationship can be derived as $\langle V \rangle = 0$ for $I \leq I_c$ and $\langle V \rangle = R\sqrt{I^2 - I_c^2}$ for $I \geq I_c$, in which $\langle V \rangle$ is

the time averaged voltage (see Fig. 2.2(a)) [22]. When $\beta_c \gg 1$, the particle is not immediately trapped after removing the driving force because of the low damping. This corresponds to a large junction capacitance shunting the oscillating junction voltage and thus $V(t) \approx \langle V \rangle$. When increasing I from zero, the junction voltage will stay at zero and suddenly jump to a finite value at $I \geq I_c$. When reducing I, the phase difference $\phi(t) = 2e/\hbar\langle V \rangle t + const.$ is linear with time according to Eq. 2.6. Combining with Eq. 2.5 leads to $\langle I_s(t) \rangle = \langle I_c sin(2e/\hbar\langle V \rangle t + const.) \rangle = 0$. As a result, the current through the junction is almost completely carried by the resistance ($I = \langle V \rangle / R$) and a finite voltage stays even when I is reduced to below I_c, which results in a hysteretic I–V characteristic (see Fig. 2.2(b)). The actual I–V dependence for a finite β_c can be obtained from numerical solutions, more details can be found in Ref. [22].

2.3 The dc SQUID

2.3.1 Basic equations

A dc SQUID is a superconducting ring interrupted by two Josephson junctions and the configuration is schematically illustrated in Fig. 2.3. At the presence of an externally applied magnetic field B, $\Phi_a = A_{eff} \cdot B$ is the magnetic flux through the SQUID loop with the effective area A_{eff}. The total bias current through the SQUID is I and the circulating current around the loop is J. The currents through the two Josephson junctions are $I/2 \pm J$ and can be written following the RCSJ model Eq. 2.7:

$$I/2 - J = C_1 \frac{\Phi_0}{2\pi} \ddot{\phi}_1 + \frac{1}{R_1} \frac{\Phi_0}{2\pi} \dot{\phi}_1 + I_{c1} sin\phi_1 + I_{n1}, \tag{2.10}$$

$$I/2 + J = C_2 \frac{\Phi_0}{2\pi} \ddot{\phi}_2 + \frac{1}{R_2} \frac{\Phi_0}{2\pi} \dot{\phi}_2 + I_{c2} sin\phi_2 + I_{n2}. \tag{2.11}$$

Meanwhile, as for any superconducting rings, the total flux enclosed in the SQUID loop follows the fluxoid quantization [66]:

$$2\pi n = \phi_1 - \phi_2 + 2\pi \frac{\Phi_a + LJ + (L_1 - L_2)I/2}{\Phi_0}, \tag{2.12}$$

in which L_1 and L_2 are the inductances of the two SQUID branches and $L = L_1 + L_2$ is the SQUID loop inductance.

For convenience, Eqs. 2.10–2.12 can be rewritten in dimensionless units by normalizing currents to the average SQUID critical current $I_c = (I_{c1} + I_{c2})/2$,

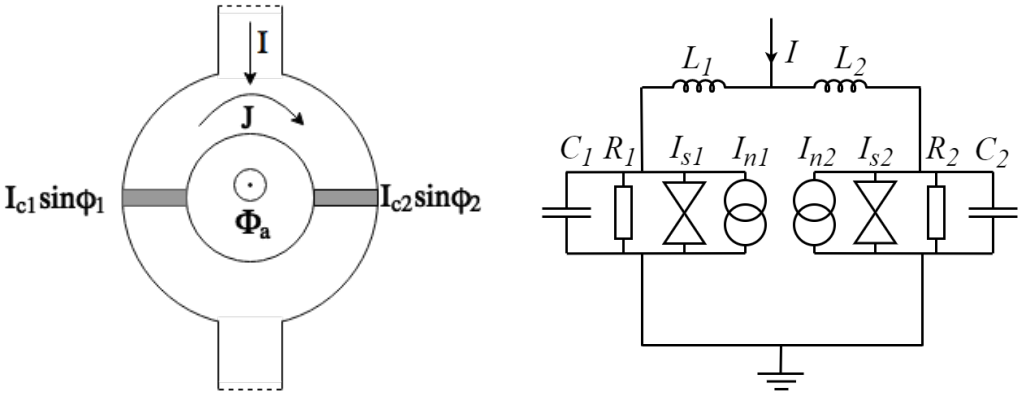

(a) (b)

Figure 2.3: (a) A schematic drawing of the dc SQUID. (b) The equivalent circuit of a dc SQUID.

capacitances to the parallel SQUID capacitance $C = (C_1 + C_2)/2$, resistances to $R = 2R_1R_2/(R_1 + R_2)$, time to $\tau = 1/\omega_c = \Phi_0/(2\pi I_c R)$, voltage to $I_c R$ and magnetic flux to Φ_0 [22]:

$$i/2 - j = \beta_c(1 + \alpha_C)\ddot{\phi}_1 + (1 + \alpha_R)\dot{\phi}_1 + (1 + \alpha_I)sin\phi_1 + i_{n1}, \tag{2.13}$$

$$i/2 + j = \beta_c(1 - \alpha_C)\ddot{\phi}_2 + (1 - \alpha_R)\dot{\phi}_2 + (1 - \alpha_I)sin\phi_2 + i_{n2} \tag{2.14}$$

and

$$\phi_1 - \phi_2 = 2\pi\phi_a + \pi\beta_L j + \pi\beta_L\alpha_L i/2, \tag{2.15}$$

where $i = I/I_c$, $j = J/I_c$ and $i_{n1,2} = I_{n1,2}/I_c$ are the normalized bias, circulating and noise currents, respectively. Parameters α_C, α_R, α_I and $\alpha_L \in [0, 1]$ describe the asymmetries in the junction capacitances, resistances, critical currents and inductances, respectively (zero means no asymmetry). The Stewart-McCumber parameter $\beta_c = 2\pi I_c R^2 C/\Phi_0$ is introduced before and $\beta_L = 2LI_c/\Phi_0$ is the screening parameter. These equations fully characterize the behavior of a dc SQUID.

In the case of zero voltage state (time derivatives are zero) with no noise ($i_{n1} = i_{n2} = 0$), Eqs. 2.13–2.15 reduce to:

$$i = (1 + \alpha_I)sin\phi_1 + (1 - \alpha_I)sin\phi_2, \tag{2.16}$$

$$2j = -(1 + \alpha_I)sin\phi_1 + (1 - \alpha_I)sin\phi_2 \tag{2.17}$$

and

$$\phi_2 = \phi_1 - 2\pi\phi_a - \pi\beta_L j - \pi\beta_L\alpha_L i/2. \tag{2.18}$$

These equations can be numerically solved to obtain the critical current modulation curve $i_c(\phi_a)$ with the applied flux under the selection of α_I, α_L and

β_L [77, 78]. Fig. 2.4a shows $i_c(\phi_a)$ modulation curves for variable β_L with identical junctions ($\alpha_I = \alpha_L = 0$) and Fig. 2.4b plots the critical current modulation versus β_L. It is indicated that the critical current modulation approaches the maximum value as long as the SQUID inductance L drops down to below a certain magnitude corresponding to $\beta_L \approx 0.1$.

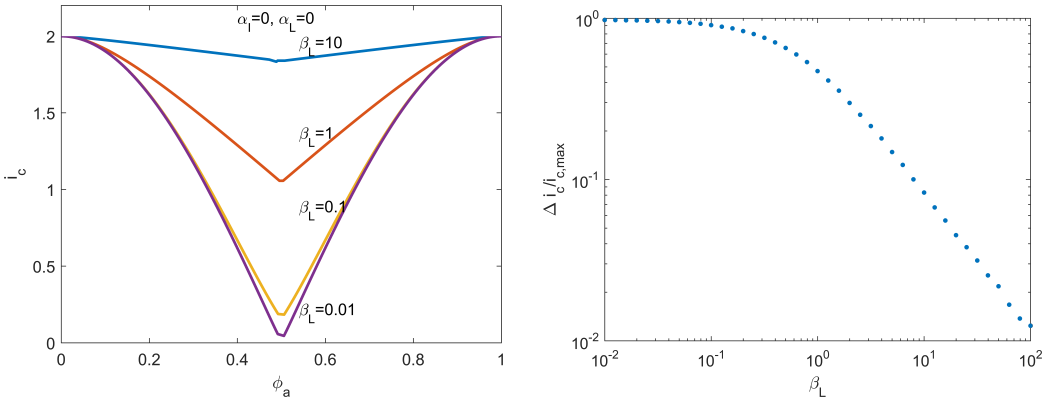

Figure 2.4: (a) Simulated normalized critical current as a function of normalized magnetic flux in the SQUID loop for $\alpha_I = \alpha_L = 0$ with $\beta_L = 0.01$, 0.1, 1 and 10. (b) Simulated normalized critical current modulation depth $\Delta i_c/i_{c,max}$ vs. β_L. (See also Ref. [77])

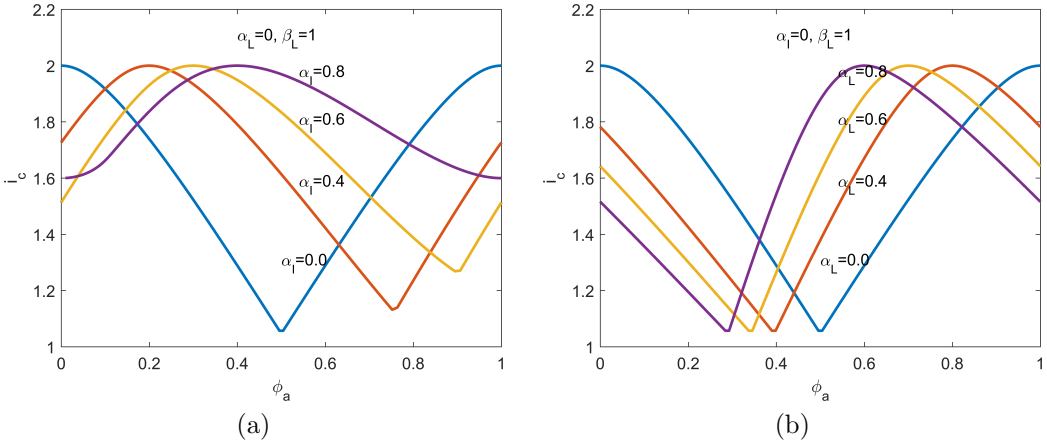

Figure 2.5: Simulated critical current modulation curves for (a) variable α_I with $\alpha_L = 0, \beta_L = 1$ and (b) variable α_L with $\alpha_I = 0, \beta_L = 1$. (See also Ref. [77])

Fig. 2.5a and 2.5b show $i_c(\phi_a)$ modulation curves for variable α_I and α_L with $\beta_L = 1$. The critical current modulation depth Δi_c decreases with α_I and is independent of α_L. For a more comprehensive discussion on the influence from stochastic noise currents, see Ref. [22].

In the case of nonzero dc voltage state, neglecting the junction capacitance ($\beta_C = 0$, practical SQUIDs are made from junctions with negligible capacitances for a non-hysteretic I–V curve) and noise currents ($i_{n1} = i_{n2} = 0$), the system of differential equations to be solved are:

$$v_1 = \dot{\phi}_1 = \frac{i/2 - j - (1+\alpha_I)sin\phi_1}{1+\alpha_R}, \tag{2.19}$$

$$v_2 = \dot{\phi}_2 = \frac{i/2 + j - (1-\alpha_I)sin\phi_2}{1-\alpha_R}, \tag{2.20}$$

$$j(\tau) = \frac{\phi_1 - \phi_2 - 2\pi\phi_a - \pi\beta_L\alpha_L i/2}{\pi\beta_L}, \tag{2.21}$$

$$v(\tau) = \frac{1+\alpha_L}{2}v_1 + \frac{1-\alpha_L}{2}v_2. \tag{2.22}$$

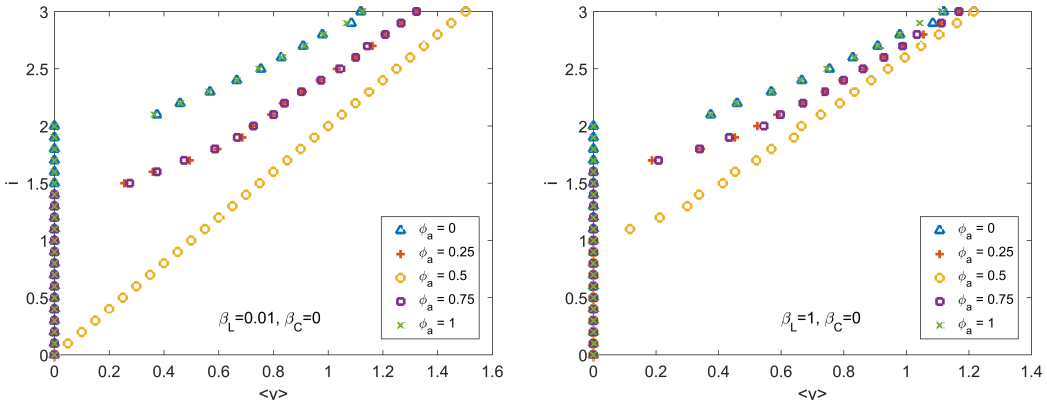

(a) (b)

Figure 2.6: Simulated normalized I–V characteristics of symmetric SQUIDs as a function of applied flux with (a) $\beta_C = 0$, $\beta_L = 0.01$ and (b) $\beta_C = 0$, $\beta_L = 1$. (See also Ref. [22])

After solving for $v(\tau)$, we can obtain the time-averaged voltage $\langle v \rangle$ by averaging $v(\tau)$ over the period of oscillation and plot I–V characteristics for selected SQUID parameters. Fig. 2.6a and 2.6b show the I–V characteristics of symmetric SQUIDs ($\alpha_R = \alpha_I = \alpha_L = 0$) with $\beta_L = 0.01$ and $\beta_L = 1$, respectively. The I–V curves are modulated by the applied flux with a period of ϕ_0 and when the SQUID is biased at some current higher than the SQUID critical current $2i_c$, a voltage–flux (V–Φ) modulation $v(\phi_a)$ is observed. Fig. 2.7a and 2.7b illustrate V–Φ modulations for two SQUIDs with $\beta_L = 0.01$ and $\beta_L = 1$, respectively, at various values of bias currents. For the discussion of the effect from nonzero capacitances, asymmetric junctions and finite noise currents, see Ref. [22].

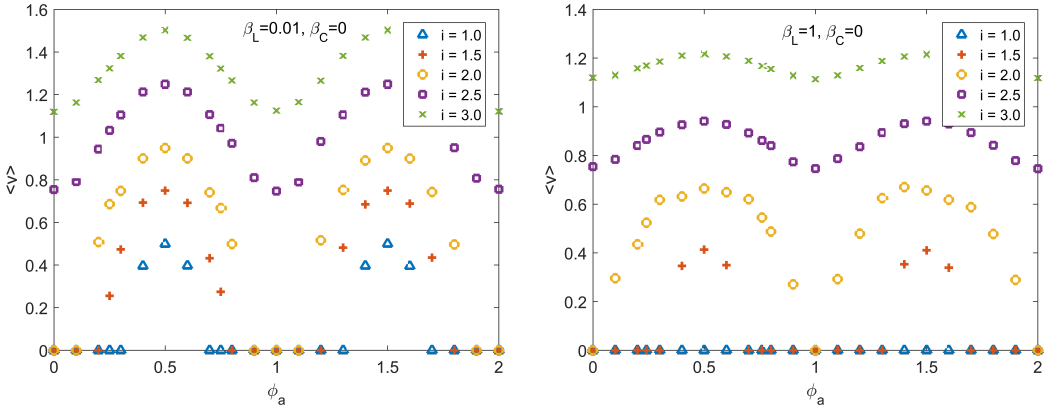

(a) (b)

Figure 2.7: Simulated voltage–flux characteristics $v(\phi_a)$ of symmetric SQUIDs at different bias current values with (a) $\beta_C = 0$, $\beta_L = 0.01$ and (b) $\beta_C = 0$, $\beta_L = 1$. (See also Ref. [22])

As such, a SQUID works as a flux-to-voltage converter and its normalized transfer function $v_\phi = max(|\partial v/\partial \phi_a|)$ is defined as the maximum slope on the V–Φ curve. A commonly used expression of v_ϕ is [79–81]:

$$v_\phi = \frac{4}{1+\beta_L} exp(-\frac{3.5\pi^2 k_B T L}{\Phi_0^2}). \tag{2.23}$$

2.3.2 Noise in dc SQUIDs

In a noise power spectrum of dc SQUIDs, two regimes can be distinguished: the white noise (Nyquist noise) and the $1/f$ noise ("flicker" noise). The white noise is due to thermal fluctuations in the Josephson junctions and is not frequency dependent. This thermal noise results in rounding of the I–V curve at low voltages [77, 82]. With a spectral density of voltage noise S_{Ve} from the preamplifier, the spectral density of equivalent magnetic flux noise of the SQUID can be written as [83]:

$$S_\Phi^{1/2} = \frac{S_V^{1/2}}{V_\Phi} \approx \frac{\sqrt{\frac{12 k_B T}{R}[\frac{R^2}{2} + \frac{(LV_\Phi)^2}{4}] + S_{Ve}}}{V_\Phi}, \tag{2.24}$$

in which $V_\Phi = v_\phi \cdot I_c R/\Phi_0$ is the transfer function. For a proper SQUID operation, the thermal energy should be lower than the Josephson coupling energy $k_B T/E_J = 2\pi k_B T/(I_c \Phi_0) < 0.2$ ($I_c > 17\mu A$ at 77 K) and the SQUID inductance should be smaller than the fluctuation threshold inductance $L < L_F = (\Phi_0/2\pi)^2/k_B T$ ($L \lesssim 100$ pH at 77 K) [22]. Fig. 2.8a and 2.8b show the dependence of SQUID white flux noise on the SQUID inductance for a variety

of I_c and R values with and without the preamplifier noise, respectively. For a smaller I_cR product, the SQUID has a more significant influence from the preamplifier noise.

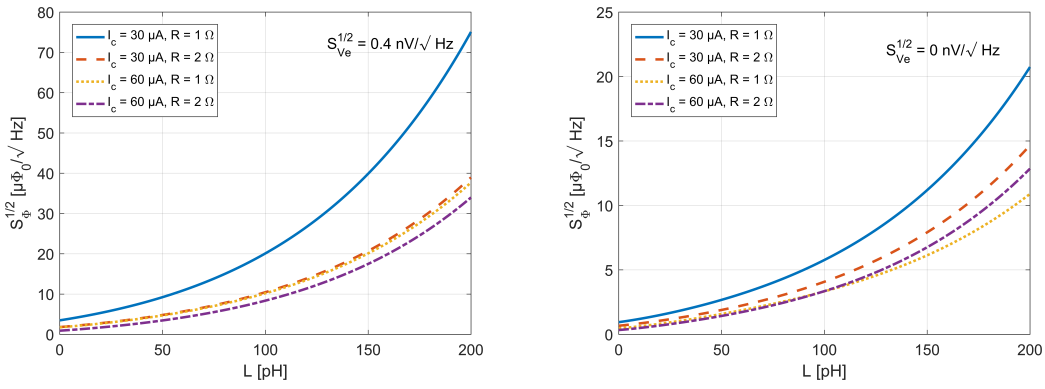

Figure 2.8: SQUID white flux noise as a function of the inductance for various values of I_c and R with (a) $S_{Ve}^{1/2}$=0.4 nV/$\sqrt{}$Hz and (b) no preamplifier noise.

The $1/f$ noise of SQUIDs refers to the low-frequency range on the noise power spectrum where the flux noise scales as $1/f$. This noise originates from two main sources: fluctuations of junction critical currents and thermally activated motion of trapped flux (vortices). Fluctuations of critical currents in the two junctions can occur in both in-phase and out-of-phase modes, which contribute to the SQUID noise through different ways [84, 85]. The in-phase mode produces a voltage noise across the SQUID and the out-of-phase mode produces a noise current circulating around the SQUID loop. Both contributions can be substantially eliminated by utilizing the bias reversal scheme, in which the bias current is reversed periodically at some frequency above the $1/f$ corner frequency [84, 86].

The other source of $1/f$ noise is due to thermally activated motion of vortices. During cooling the superconducting circuits to below T_c, flux can be trapped in defects (pinning centers) in the film and form vortices. When the thermal energy is high enough to overcome the pinning energy, a vortex can hop between two or more adjacent pinning centers and induce a random telegraph signal in the SQUID output. This noise source cannot be treated by the bias reversal scheme, but can be reduced by approaches like improving the pinning of vortices (film quality control [87]) and/or preventing vortex entry (active field cancellation [88–91]; narrow linewidth structures [92–94]; flux dams [95]) during the cooling.

For low-T_c SQUIDs, the white flux noise is typically below 1 $\mu\Phi_0\sqrt{}$Hz and the $1/f$ noise is usually not a big issue. On the contrary, high-T_c SQUIDs

usually exhibit higher white flux noise levels around 10 $\mu\Phi_0\sqrt{\text{Hz}}$ and require more sophisticated methods to keep the $1/f$ corner frequency below 10 Hz because of the higher operation temperature (77 K) [43]. For applications where the low-frequency signal measurements are essential, e.g., MEG, it is important to characterize the noise behavior when benchmarking the performance of high- and low-T_c sensors.

2.3.3 SQUID readout

As can be seen in Fig. 2.7, the $\partial v/\partial\phi$ slope (flux-to-voltage transfer coefficient) is different along a V–Φ modulation curve and thus the SQUID readout is nonlinear and depends on the magnetic flux. To linearize the readout, practical SQUIDs are operated in a flux-locked loop (FLL), in which a feedback loop is included to lock the SQUID at the point with the maximum slope on a V–Φ curve (the transfer function v_ϕ) that gives the highest sensitivity [86]. The diagram of such a circuit is shown in Fig. 2.9. Starting from the $v_\phi = max(|\partial v/\partial\phi_a|)$ point on the V–Φ modulation curve, a tiny change in the flux through the SQUID loop will shift the working point away from the original position and result in a large change in the voltage across the SQUID. This voltage change is amplified and fed back as a current through a feedback coil sitting close to the SQUID. A feedback flux is induced to compensate the applied flux and bring the working point back to the original position. Because the short segment nearby the maximum-slope point is almost linear, the voltage across the feedback resistor becomes the linearized SQUID readout.

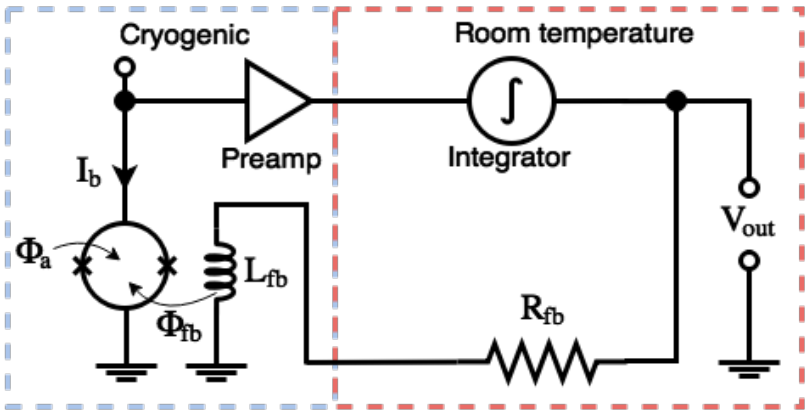

Figure 2.9: Sketch of the FLL SQUID readout circuit. An applied flux signal in the SQUID loop induces a voltage signal across the SQUID, which is amplified, integrated and fed back as a current through the feedback coil to counterbalance the applied flux. As a result, the voltage across the feedback resistor is the linearized output signal.

2.4 High-T_c SQUID magnetometers

2.4.1 High-T_c superconductor: YBCO

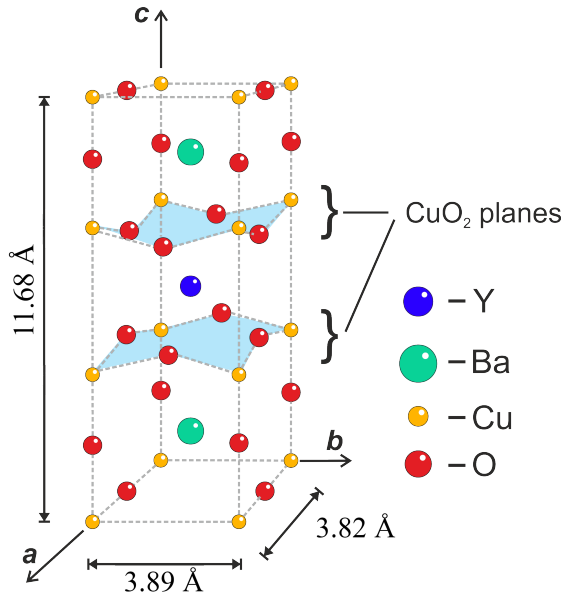

Figure 2.10: Sketch of a unit cell of YBCO. (Adapted from [96])

As introduced earlier, most practical high-T_c SQUIDs are produced from the high-T_c superconductor $YBa_2Cu_3O_{7-x}$ (YBCO). YBCO has an oxygen deficient structure consisting of layers and a sketch of the crystal structure is shown in Fig. 2.10. The lattice parameters are $a = 3.82$ Å, $b = 3.89$ Å and $c = 11.68$ Å. The transport properties of YBCO are very dependent on the oxygen content ($n = 7 - x$) per unit cell and the hole doping (p): YBCO is an antiferromagnetic insulator when the hole doping is close to zero ($0 < n < 6.4$, $0 < p < 0.05$); under-doped ($6.4 < n < 6.9$, $0.05 < p < 0.16$) YBCO becomes superconducting and its T_c depends on the oxygen stoichiometry; optimally doped YBCO ($n \approx 6.9$, $p \approx 0.16$) has the maximum T_c of 94 K for bulk crystals; slightly over-doped ($6.9 < n < 7$, $0.16 < p < 0.19$) YBCO has a reduced T_c [63]. Fig. 2.11a and 2.11b show the XRD analysis of two YBCO films grown with optimally doped and under-doped conditions. The 2θ values of peaks can be used to calculate the c lattice parameter using Bragg's law ($n\lambda = 2dsin\theta$, in which n is the index of peak, λ is the wavelength of the incident X-ray and θ is the scattering angle). The c lattice parameter is related to the oxygen content per unit cell in the film [96]. In this thesis, we mainly work with optimally doped or slightly over-doped YBCO films

because a high transition temperature is desired for SQUID applications.

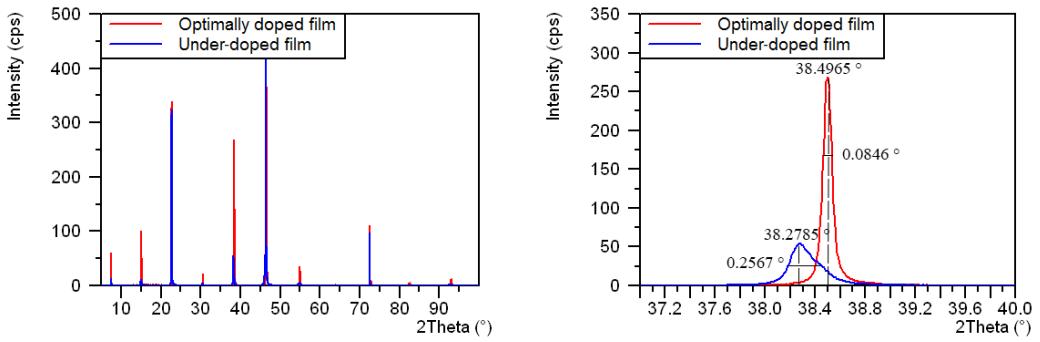

(a) (b)

Figure 2.11: (a) X-ray diffraction analysis of an optimally doped film and an under-doped film. (b) Zoom-in on the YBCO (0 0 5) reflections with the 2θ values and peak widths indicated.

YBCO films can be deposited using pulsed laser deposition (PLD) or sputtering on several different substrates including $SrTiO_3$ (STO), MgO, $LaAlO_3$ (LAO) and $NdGaO_3$ (NGO) [43]. In our work, the film is deposited with PLD on either STO or MgO substrates. Fig. 2.12a and 2.12b show the picture and sketch of our PLD system, respectively. In the PLD, a laser beam of 248 nm wavelength and 20 ns pulse duration is generated at a certain frequency by a Kr/F excimer laser. The laser beam is regulated by an aperture, reflected by a mirror, focused by a lens into the PLD chamber on to the target, which in turn is positioned just below the substrate. In the presence of background oxygen, the target material is ablated by the pulsed laser beam and forms a plasma plume approaching the substrate which is heated up to the deposition temperature in advance. Given the proper growth conditions (Table 2.1 lists the relevant parameters and reference values for our system), a stoichiometric growth of YBCO film on the substrate can be achieved. During the deposition, substrate rotation and scanning are utilized to improve the uniformity of the film. After deposition, the film is annealed in oxygen at the post annealing pressure and temperature for 60–120 min and then slowly cooled down to room temperature. If needed, an optional *in situ* Au capping layer can be sputtered on the film.

Fig. 2.13 shows the transition temperature measurement of two 250 nm films on STO (0 0 1) (optimally doped and under-doped, respectively) and one 50 nm film on MgO (1 1 0) (optimally doped). The shape of the transition indicates the quality of the film and a uniform film usually has a sharp transition. For a 50 nm film, five orders of magnitude lower post annealing pressure is enough to achieve an optimally or slightly over-doped status as

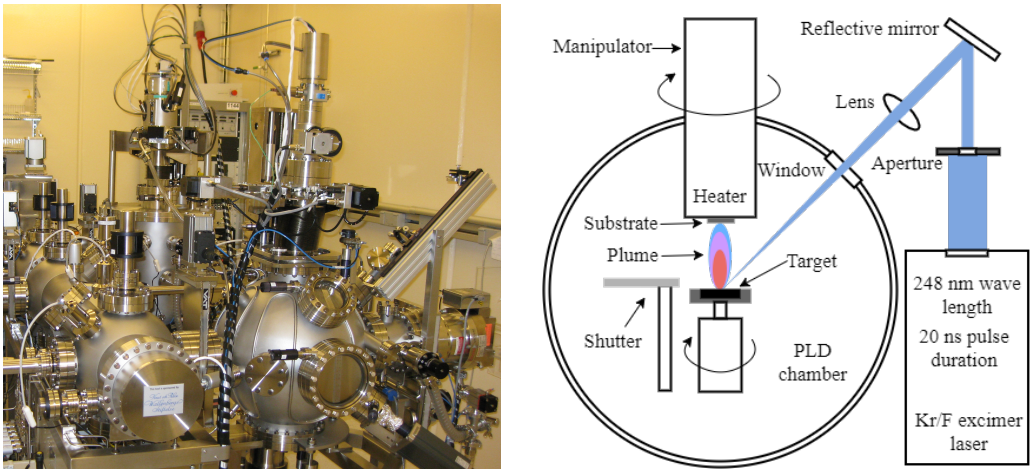

(a) (b)

Figure 2.12: Pulsed laser deposition (PLD) system: (a) A picture of the PLD chamber with the transfer and loading line and (b) a sketch showing the internal composition and working status of the PLD. Note, that the PLD system is one of the chambers in a cluster system with two additional sputtering systems connected to the transfer and loading line (the long buffer chamber to the left in the picture).

compared to a 250 nm film. Fig. 2.14 presents the atomic force microscopy (AFM) images showing the surface morphology of the optimally doped and under-doped 250 nm films and the average roughness is around 2 nm in both cases. The surface of optimally doped film shows presence of characteristic *c*-axis spiral-like islands.

Table 2.1: Deposition parameters of YBCO films on STO and MgO substrates with PLD.

Growth conditions	250 nm film on STO substrate	50 nm film on MgO substrate
Substrate temperature	760 °C	760 °C
Energy density on the target	1.68 J/cm^2	1.60 J/cm^2
Depositing oxygen pressure	1.6 mbar	1.2 mbar
Target-to-substrate distance	52 mm	54 mm
Pulse frequency	10 Hz	6 Hz
Number of pulses	4500	900
Post annealing temperature	550 °C	550 °C
Post annealing pressure	640 Torr	1.3 mTorr
Post annealing time	60 min	60 min

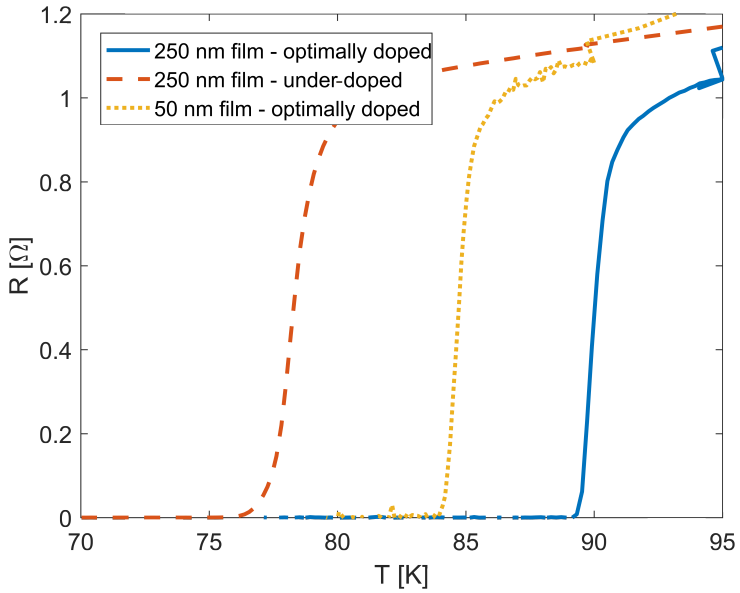

Figure 2.13: Resistance–temperature measurements of YBCO films. The optimally doped and under-doped 250 nm films are deposited on STO and correspond to those films in Fig. 2.11 and Fig. 2.14. The optimally doped 50 nm film is deposited on MgO. These resistance–temperature curves were taken with the Physical Property Measurement System (PPMS®).

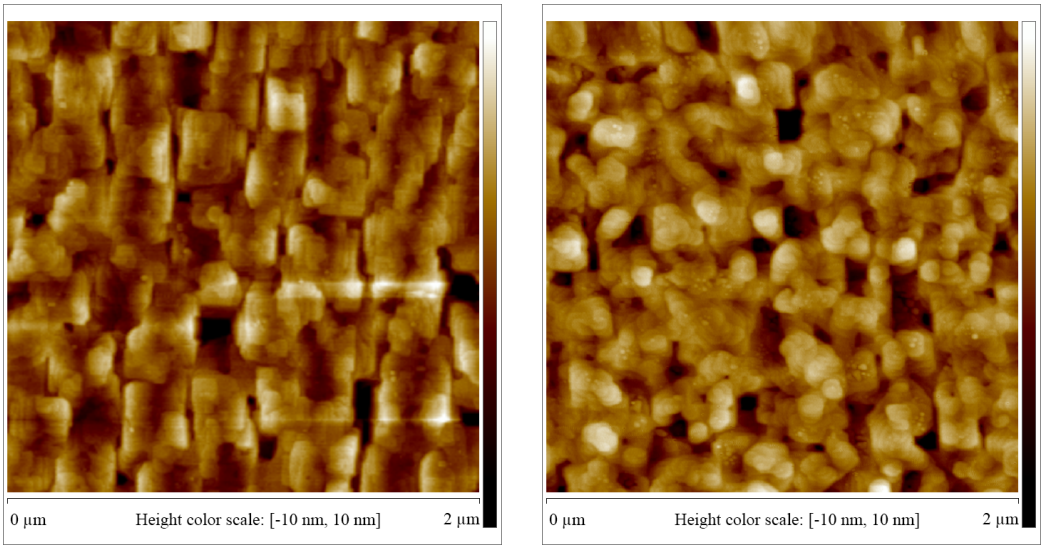

(a) (b)

Figure 2.14: AFM pictures of (a) an optimally doped and (b) an under-doped film. The scan areas are 2 μm × 2 μm and the color scales represent the height. The optimally doped film has well-defined c-axis spiral-like islands.

2.4.2 Magnetometers based on dc SQUIDs

A dc SQUID has been demonstrated to be a sensitive flux-to-voltage converter. However, a bare (uncoupled) SQUID is usually a poor magnetic field sensor because the effective area $A_{eff} = \Phi_a/B$ is limited by the geometric dimension of the SQUID hole, which needs to be small in order for L_{SQ} to be below 100 pH at 77 K [22]. To improve the magnetic field resolution (or the effective area), coupling methods like introducing a galvanically coupled pickup loop in single-layer devices [97–101] or introducing an inductively coupled flux transformer in flip-chip or integrated devices [43, 46, 47, 59, 102–104] need to be implemented. The equivalent circuits of these two coupling methods are illustrated in Fig. 2.15.

SQUID magnetometers with a directly connected pickup loop can be fabricated by depositing a single YBCO layer and only one step of lithography is needed for patterning. A magnetic field sensitivity of 93 fT/$\sqrt{}$Hz down to 1 Hz was demonstrated with this type of high-T_c SQUID magnetometers with a 47 mm^2 pickup loop in an early work [99]. A state-of-the-art device with a 64 mm^2 pickup loop was reported to have a magnetic field sensitivity of $\sim$30 fT/$\sqrt{}$Hz at 77 K [105]. As can be understood from the circuit diagram of Fig. 2.15a, a change of external magnetic field δB will induce a change of magnetic flux $\delta\Phi_{SQ}$ inside the SQUID loop. The effective area of the SQUID magnetometer A_{eff}^{Mag} is therefore:

$$A_{eff}^{Mag} = \delta\Phi_{SQ}/\delta B = (-\delta\Phi_{SQ}^{SQ} + \delta\Phi_{SQ}^{cp})/\delta B, \tag{2.25}$$

in which $\delta\Phi_{SQ}^{SQ} = \delta B \cdot A_{eff}^{SQ}$ is the self-induced term of the SQUID loop and $\delta\Phi_{SQ}^{cp} = L_m \cdot I_{pk}$ is the coupling term through the galvanically connected pickup loop (L_m is the inductance of the SQUID-loop section shared with the pickup loop). The current I_{pk} is induced by the flux change inside the pickup loop: $\delta\Phi_{pk} = \delta B \cdot A_{eff}^{pk} = I_{pk} \cdot L_{pk}^{SQ}$. As such, Eq. 2.25 can be derived as:

$$A_{eff}^{Mag} = -\frac{\delta\Phi_{SQ}^{SQ}}{\delta B} + \frac{\delta\Phi_{SQ}^{cp}}{\delta B} = -A_{eff}^{SQ} + \frac{L_m}{L_{pk}^{SQ}} A_{eff}^{pk} \approx \frac{L_m}{L_{pk}^{SQ}} A_{eff}^{pk}. \tag{2.26}$$

The last approximation is valid because the inductance and effective area of the SQUID loop are usually much smaller than those of the pickup loop.

A_{eff}^{Mag} can be improved by increasing the mutual inductance L_m or the ratio A_{eff}^{pk}/L_{pk}^{SQ}. Inside the SQUID loop, the shared section with the pickup loop (L_m) is connected through two junctions ($2 \times L_J$) to the rest part of the loop, which is connected to the bias lead and refered to as the electrode

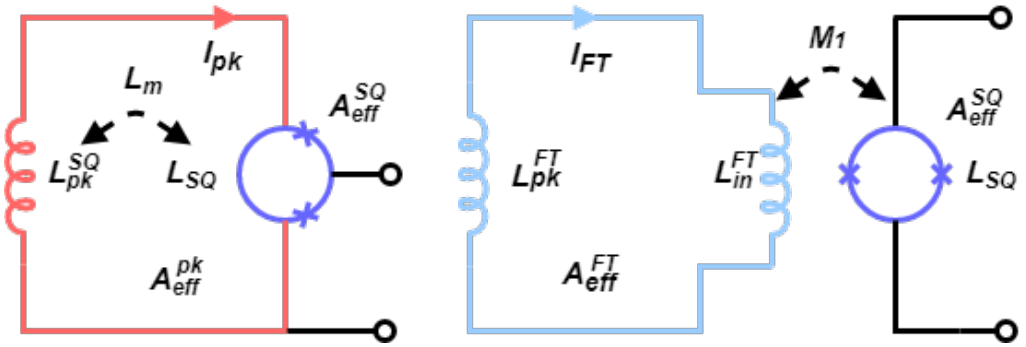

(a) (b)

Figure 2.15: Equivalent circuits of SQUID magnetometers with (a) a directly connected pickup loop and (b) an inductively coupled flux transformer.

(L_{el}). Therefore, $L_{SQ} = L_m + 2 \times L_J + L_{el}$. As shown earlier, upper limits of L_{SQ} are set by the SQUID modulation performance ($\beta_L \sim 1$) and the noise performance ($L_{SQ} < L_F$), which also limit L_m. The ratio A_{eff}^{pk}/L_{pk}^{SQ} has been shown to achieve a maximum when the pickup loop linewidth is $(D_o - D_i)/2$, in which D_o and D_i are the outer and inner dimensions of the pickup loop [100, 101]. At the limit $D_o - D_i > 2D_i$, $A_{eff}^{pk} = D_o D_i$ and $L_{pk,geo}^{SQ} = 1.25\mu_0 D_i$. $L_{pk,geo}^{SQ}$ is the geometric part of the pickup loop inductance and when the film gets thinner, a kinetic part $L_{pk,kin}^{SQ}$ also needs to be taken into account. As such, combining with Eq. 2.24, one can write the spectral density of equivalent magnetic field noise of SQUID magnetometers with a directly connected pickup loop as: $S_B^{1/2} = S_\Phi^{1/2}/A_{eff}^{Mag} = 1.25\mu_0 S_\Phi^{1/2}/L_m D_o$. Fig. 2.16a and 2.16b show $S_B^{1/2}$ as a function of L_{SQ} for a number of $2 \times L_J$ values with $I_c = 60\mu$ A, $R = 2\ \Omega$, $L_{el} = 0$ pH, $L_{pk,kin}^{SQ} = 0$ pH and $D_0 = 8$ mm in the cases of 0.4 nV/$\sqrt{\text{Hz}}$ and no preamplifier noise, respectively. It can be seen that the $2 \times L_J$ values limit the achievable field sensitivity, which is more significant in the case of finite preamplifier noise.

The other type of coupling approach includes an inductively coupled superconducting flux transformer (as shown in Fig. 2.15b). The flux transformer is a closed superconducting circuit consisting of a large-area pickup loop and a small multiturn input coil matching the dimension of the SQUID washer. To realize such a structure, multi-layer fabrication technology is required. The flux transformer can be integrated on the SQUID chip [106] while for high-T_c applications the flux transformer is more often fabricated separately and mounted face-to-face to the SQUID chip in a flip-chip configuration [47, 104]. The change of flux sensed by the flux transformer pickup loop is $\delta\Phi_{FT} = \delta B \cdot A_{eff}^{FT} = I_{FT} \cdot (L_{pk}^{FT} + L_{in}^{FT})$, where L_{pk}^{FT} and L_{in}^{FT} are the

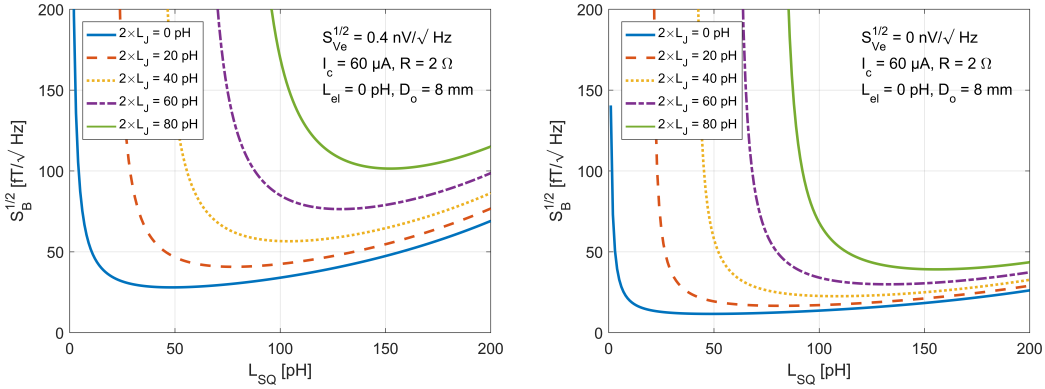

(a) (b)

Figure 2.16: SQUID field sensitivity as a function of the inductance for various values of $2 \times L_J$ with (a) $S_{Ve}^{1/2}$=0.4 nV/$\sqrt{}$Hz and (b) no preamplifier noise.

inductances of the pickup loop and input coil of the flux transformer, respectively. The effective area of the magnetometer can also be written as the sum of a self-induced term and a coupling term as in Eq. 2.25. The difference from the directly coupled device is that the coupling here is through the inductively coupled flux transformer: $\delta\Phi_{SQ}^{cp} = M_1 \cdot I_{FT}$, in which $M_1 = k_{M1} \cdot \sqrt{L_{in}^{FT} L_{SQ}}$ is the mutual inductance between the flux transformer input coil and the SQUID washer. As a result, the effective area of this type of magnetometers is:

$$\begin{aligned} A_{eff}^{Mag} &= \frac{\delta\Phi_{SQ}^{SQ}}{\delta B} + \frac{\delta\Phi_{SQ}^{cp}}{\delta B} = A_{eff}^{SQ} + k_{M1} \frac{\sqrt{L_{in}^{FT} L_{SQ}}}{L_{pk}^{FT} + L_{in}^{FT}} A_{eff}^{FT} \\ &\approx \frac{k_{M1}}{2} \sqrt{\frac{L_{SQ}}{L_{in}^{FT}}} A_{eff}^{FT}. \end{aligned} \tag{2.27}$$

Again the last approximation is valid because the effective area of the SQUID loop is much smaller than that of the flux transformer. L_{pk}^{FT} is designed equal to L_{in}^{FT} for the maximum A_{eff}^{FT} [107].

2.4.3 Bicrystal grain boundary SQUIDs

There are three predominant types of high-T_c Josephson junction technologies used for making SQUIDs: bicrystal grain boundary junctions, step-edge grain boundary junctions and ramp-edge junctions [22, 43]. Among these, many successful practical SQUID magnetometers were realized on bicrystal grain boundary junctions [32, 45, 46, 99, 100, 107–109]. Bicrystal grain boundary junctions rely on the epitaxial growth of high-T_c films on

bicrystal substrates, which typically have a misorientation angle of 24°, 30° or 36° [22]. Junctions can be obtained by patterning microbridges crossing the grain boundary formed in the film. We use 24° STO bicrystal substrates in this work and typical critical current densities of junctions on this type of substrates are 10^4–10^5 A/cm^2 [110]. This technology is relatively reproducible and the fabrication procedure is straightforward. The limit of bicrystal grain boundary junctions lies in the lack of freedom in design, i.e., junctions can only be placed at the position of the grain boundary given by the bicrystal substrate.

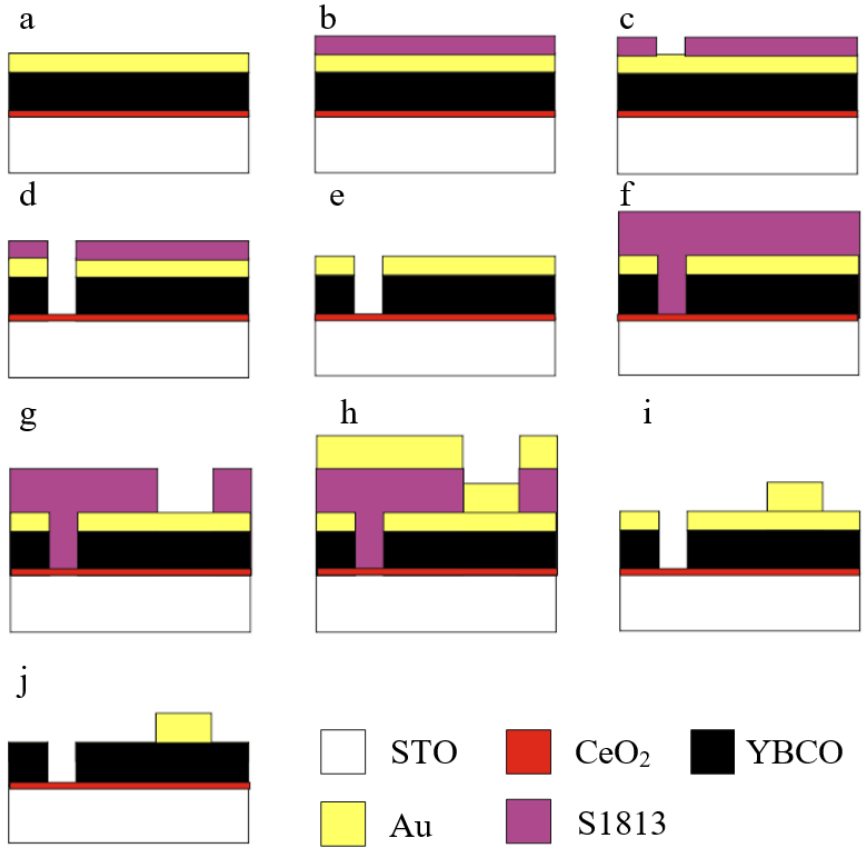

Figure 2.17: A step-by-step illustration of the fabrication process for bicrystal grain boundary SQUIDs. a) A layer of 50 nm CeO_2 is sputtered on the substrate and 250 nm YBCO film is deposited. Upon that around 20 nm gold film is grown *in-situ*. b) A layer of S1813 photoresist is spun on top of the sample and baked on a hot plate at 95 °C for 3 min. c) The photoresist is exposed by UV light through a chromium mask and developed in MF-319 followed by 15 s O_2 plasma ashing. d) Ar^+ ion milling with the control by secondary ion mass spectrometry (SIMS) is used to etch the sample. e) The sample is cleaned in acetone and isopropanol to remove the photoresist. f) A thicker layer of S1813 is spun onto the sample. g) Photolithography is used to open the contact windows. h) A layer of 400 nm gold is sputtered. i) Lift-off in acetone and an ultrasonic bath is carried out to release the pattern. j) The protective gold layer is removed using Ar ion milling.

The fabrication procedure of the bicrystal grain boundary SQUID is il-

lustrated in Fig. 2.17. Before the deposition of the YBCO film, a seed layer of 50 nm CeO_2 is sputtered on the bicrystal substrate using an oxide sputter system (DCA instruments) in order to improve the quality of the deposited film in the vicinity of the grain boundary. After that, a 250 nm YBCO film is deposited with the UHV-PLD system (DCA instruments). A 20 nm protective gold layer is deposited *in-situ* using a metal sputter system (DCA instruments). This gold layer helps to reduce the degradation of the YBCO film quality caused by direct contact with water and atmosphere in the following processing steps.

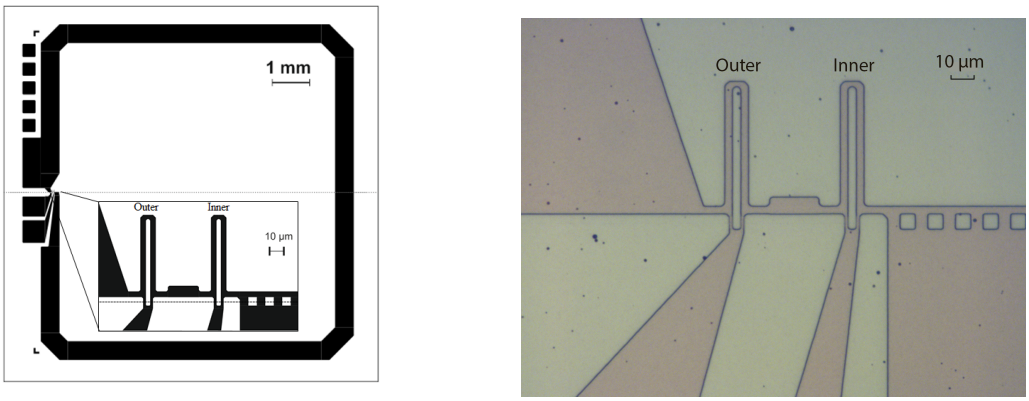

(a) (b)

Figure 2.18: (a) The layout of a bicrystal grain boundary SQUID magnetometer with a 9 mm × 9 mm pickup loop. The dashed line represents the grain boundary and the close-up shows the two SQUIDs and the flux dams. (b) The optical microscopic picture of the fabricated SQUID magnetometer.

The thin film of YBCO is then patterned using photolithography. The photoresist S1813 is spun onto the sample with a photoresist spinner at the speed of 6000 rpm, giving a thickness around 1.3 μm. A mask aligner with UV light (400 nm wavelength) is used to expose the photoresist through a chromium mask. The developer MF-319 is then used for development. The photolithography includes three steps: while the substrates usually have sharp square edges, the first step is a soft contact lithography through the frame mask to remove thicker edges of the photoresist layer; The second step is a hard contact lithography to pattern scales on the four edges of the chip. These scales are useful to make alignment of the grain boundary with the SQUID structure; The last step is a hard contact lithography to pattern the SQUID structure. After the patterning, the film is etched with the ion beam milling system – CAIBE Oxford Ionfab 300 Plus. The high current grid and 7.5 mm aperture are chosen for the operation. The beam energy for etching is set to 500 eV and the current density is 0.2 mA/cm^2. During etching the sample holder is tilted with an angle of 30° and kept rotating. Following

the etching is another photolithography for opening the contact windows. A thicker layer of S1813 is spun with the speed of 4000 rpm for the purpose of the following lift-off process. After defining the contact windows, a 400 nm layer gold is deposited using a Metal Sputter system. The lift-off is carried out in acetone and ultrasonic bath to release the pattern of contact pads. As the last step, the whole sample is put back into the Ion Beam Milling system and a short ($\sim$ 5 min) etching is performed to remove the protective layer of gold from the top of the YBCO structure.

Fig. 2.18a and 2.18b show the layout and optical microscopic picture of our bicrystal grain boundary SQUID magnetometers, respectively. In this design, two adjacent hairpin-shaped SQUIDs with a slit length of 60 μm, a slit width of 3 μm and a loop line width of 3 μm are directly connected to a pickup loop with an outer dimension of 9 mm $\times$ 9 mm and a loop line width of 0.5 mm. Flux dams are formed nearby the SQUID loops to help pinning the flux motion during the practical operation and reducing the flux noise.

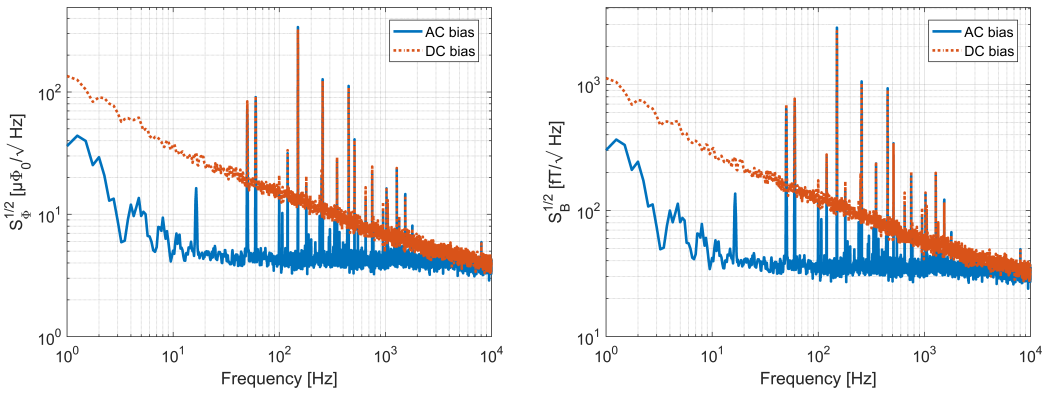

(a) (b)

Figure 2.19: (a) The spectral density of equivalent magnetic flux noise and (b) the spectral density of equivalent magnetic field noise of one of bicrystal grain boundary SQUIDs with and without AC bias reversal. The SQUID is operated inside a magnetically shielded room at Chalmers. The spectral density of magnetic field noise is calculated using measured effective area of the magnetometer of 0.24 mm^2.

The SQUIDs are operated in a flux-locked loop with a DC SQUID electronics (Magnicon GmbH SEL-1). The effective area of the SQUIDs is measured to be 0.24 mm^2 utilizing a Helmholtz coil. The noise is characterized with and without an AC bias reversal mechanism using an SR785 dynamic signal analyzer (Stanford Research Systems Inc.) while the SQUIDs are placed inside a magnetically shielded room (MSR) at Chalmers. One of the best devices fabricated shows a flux noise of 5 $\mu\Phi_0/\sqrt{\text{Hz}}$ and a field noise of 40 fT/$\sqrt{\text{Hz}}$ down to 10 Hz, which are presented in Fig. 2.19.

2.4.4 Nanowire-based SQUIDs

High-T_c nanowire is another junction technology that can be used to fabricate SQUIDs. In theory, nanowires with dimensions (length l, width w and thickness t) much smaller than the material coherence length ξ (i.e., $l, w, t \ll \xi$) show the typical sinusoidal current-phase relationship: [111]:

$$I_s = I_c sin\phi, \quad I_c = \frac{\Phi_0}{2\pi\mu_0\lambda_L^2\xi}\frac{wt}{l}. \tag{2.28}$$

When $l \gg \xi$, $w, t \ll \xi$ and $wt \ll \lambda_L^2$, the current phase dependence becomes [112, 113]:

$$\begin{aligned} I_s &= \frac{\Phi_0}{2\pi\mu_0\lambda_L^2\xi} wt \left[\frac{\xi}{l}\phi - (\frac{\xi}{l}\phi)^3\right] \\ &= \frac{\Phi_0}{2\pi L_k}\left[\phi - (\frac{\xi}{l})^2\phi^3\right], \end{aligned} \tag{2.29}$$

where $L_k = \mu_0\lambda_L^2 l/wt$ is the kinetic inductance of the nanowire. The critical current is characterized by the depairing current I_d determined by maximizing Eq. 2.29:

$$I_c = I_d = \frac{\Phi_0}{3\sqrt{3}\pi\mu_0\lambda_L^2\xi} wt, \tag{2.30}$$

which corresponds to the breaking of Cooper pairs at $\phi_d = l/\sqrt{3}\xi$.

In practice for YBCO ($\xi_{ab} \sim 2$ nm), Josephson-like behavior can be observed as long as $t \ll \lambda_L$ and $w \ll \lambda_P$, where $\lambda_P = \lambda_L^2/t$ is the Pearl penetration depth [49–51]. Here the behavior is characterized by the coherent Abrikosov vortex motion across the nanowire. The limits $t \ll \lambda_L$ and $w \ll \lambda_P$ ensure that the current in the nanowire is homogeneous and therefore Eq. 2.29 still applies for the current phase relationship, except that the critical current is now determined by the vortex entry phenomenon. The critical phase gradient at which an Abrikosov vortex is allowed to overcome the energy barrier at the edge of nanowires is $\phi_v = l/2.718\xi \simeq 0.64\phi_d$ [114] and thus the corresponding critical current is $I_c = I_v \simeq 0.826 I_d$ using Eq. 2.29.

It is a challenge to fabricate YBCO nanowires with a good quality. Because of this, the reported flux noise of nanowire-based SQUIDs was about 80 $\mu\Phi_0/\sqrt{\text{Hz}}$ at 4.2 K [49]. Recently, high-quality YBCO nanowires [52, 53] and high-T_c nanowire-based SQUIDs with magnetic flux noise <1 $\mu\Phi_0/\sqrt{\text{Hz}}$ at 8 K [54] were demonstrated with an improved fabrication procedure. Such a magnetic flux noise is impressive for high-T_c devices and makes them useful in measuring magnetization reversal in small spin systems (e.g. magnetic

nanoparticles) [55–57]. It is then natural to investigate whether practical applications that go beyond magnetic field sensitivity on the microscopic scale can also benefit from these nanowire-based SQUIDs. Like the bicrystal grain boundary SQUID magnetometers introduced earlier, coupling methods are required to transform SQUIDs from magnetic flux sensors to magnetic field sensors. In the case of nanowire-based SQUIDs, the challenges of achieving a good coupling originate from the small size of the SQUID loop, the much higher junction inductances and the very thin SQUID washer thickness. The details of developing YBCO high-T_c nanowire-based SQUID magnetometers are presented in the next chapter.

CHAPTER 3

Nanowire-based high-T_c SQUID magnetometers

3.1 Design

In this thesis work, SQUID magnetometers based on nanowire junctions (l = 200 nm, w = 50 nm and t = 50 nm) have been designed and tested with several coupling approaches. Single-layer devices with a directly connected pickup loop were first studied. The dependence of the effective area on the SQUID and pickup loop dimensions was investigated. A concept of fabricating devices with different thicknesses, i.e., the SQUID part is 50 nm and the pickup loop part is 200 nm, was proposed and tested. After that, flip-chip devices implementing an inductively coupled flux transformer were studied. A poor coupling was found due to the small thickness of the SQUID washer, which could not provide an efficient flux focusing. To address this issue, a two-level coupling approach was introduced. In such a design, the SQUID is connected to a washer-type pickup loop with an inner hole matching the size of the flux transformer input coil. This design allows the best achieved effective area of 0.46 mm^2 and magnetic field sensitivity of 240 fT/$\sqrt{\text{Hz}}$ on nanowire-based SQUID magnetometers. Methods to further enhance the effective area and magnetic field sensitivity were analyzed by numerical simulations.

3.1.1 Nanowire-based SQUIDs with a directly connected pickup loop

The concept of this type of SQUID magnetometers was introduced in Section 2.4.2. The effective area of such a device can be evaluated as $A_{eff} \approx A_{eff}^{pk} L_m / L_{pk}^{SQ}$. The main difference when replacing bicrystal grain boundary junctions with nanowire junctions is that the two inductances $2 \times L_J$ are no longer negligible because the kinetic inductance per unit length of a nanowire scales with λ_L^2/wt [115]. For the 200 nm × 50 nm × 50 nm junctions, $2 \times L_J$ are ∼70 pH at 77 K. According to Fig. 2.16a, an optimal magnetic field sensitivity is expected for a SQUID with L_{SQ} in the range of 120 to 180 pH considering the 0.4 nV/$\sqrt{\text{Hz}}$ preamplifier noise from the SQUID electronics (Magnicon SEL-1). More details regarding the SQUID and pickup loop designs are covered below.

3.1.1.1 The SQUID loop

An evolution of the SQUID loop design from the original nanoSQUIDs described in the literature [49, 54, 58, 116] to a version optimized for the coupling as needed in a magnetometer is shown in Fig. 3.1. The first one (Type I, see Fig. 3.1a) had a nanoscale SQUID loop similar to those original nanoSQUIDs while an arch was introduced for increasing the mutual inductance L_m. Such a device had a relatively small SQUID inductance L_{SQ} (∼65 pH from simulation), which resulted in a large voltage modulation depth $\triangle V$ (23.7 μV) and low magnetic flux noise $S_\Phi^{1/2}$ (10 $\mu\Phi_0/\sqrt{\text{Hz}}$) that was only limited by the preamplifier noise. The coupling between the SQUID and pickup loops was poor due to the large inductance mismatch, which gave an effective area A_{eff} of 0.5 $\times 10^{-3}$ mm^2 for a 400 μm × 400 μm pickup loop. To enhance the coupling, The next generation design (Type II, see Fig. 3.1b) with a micron-level SQUID loop and a larger L_m was introduced. In this design, the two nanowire junctions were placed at the two sides of the bottom electrode and therefore the SQUID slit width was defined by the bottom electrode width. For the same pickup loop dimension, the increase of A_{eff} to 2.9 $\times 10^{-3}$ mm^2 came along with a drop of $\triangle V$ to 9.6 μV and an increase of $S_\Phi^{1/2}$ to 30 $\mu\Phi_0/\sqrt{\text{Hz}}$. Type III (Fig. 3.1c) was designed to further increase L_m and for this, the two nanowire junctions were placed side by side with a separation of 500 nm. As a result, A_{eff} was 5.9 $\times 10^{-3}$ mm^2 while $\triangle V$ was 4.4 μV and $S_\Phi^{1/2}$ was 55 $\mu\Phi_0/\sqrt{\text{Hz}}$ for the same 400 μm × 400 μm pickup loop dimension. Here the magnetic flux was not only the preamplifier noise but also the intrinsic SQUID noise due to the large L_{SQ}. For comparison, the SQUID loop design of our bicrystal grain boundary SQUID is illustrated

in Fig. 3.1d (a 10 mm × 10 mm pickup loop was used in this case). The parameters of some selected devices are listed in Table. 3.1.

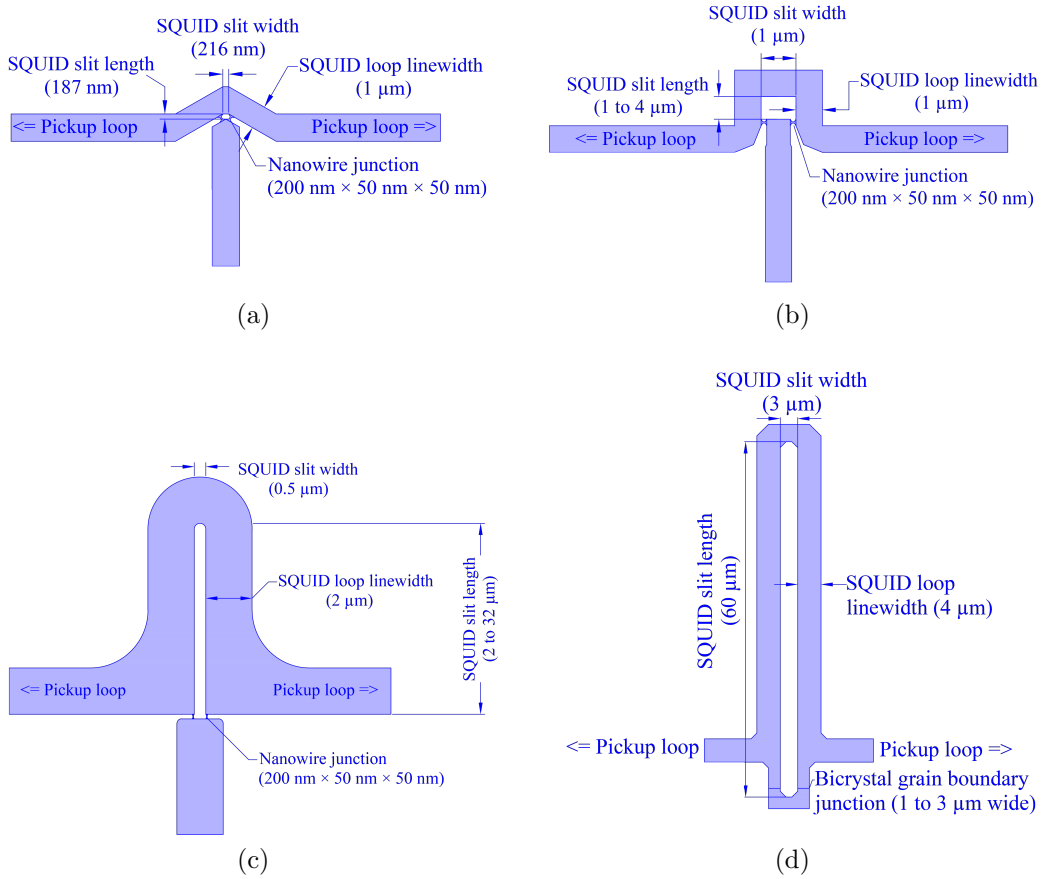

Figure 3.1: Sketches of the SQUID loop designs of three nanowire-based magnetometers and the original bicrystal grain boundary junction SQUID magnetometer. (a) Type I nanowire-based SQUID with a nanoscale SQUID loop. (b) Type II nanowire-based SQUID with nanowire junctions placed on the two sides of the bottom electrode (SQUID slit width equals to the bottom electrode width). (c) Type III nanowire-based SQUID with nanowire junctions placed close to each other (SQUID slit width fixed as 500 nm). (d) Bicrystal grain boundary SQUID.

Table 3.1: Measured and simulated parameters of SQUIDs with a directly connected pickup loop.

SQUID type	Type I	Type II	Type III	Bicrystal
SQUID loop dimension	216 nm × 187 nm	1 μm × 1 μm	500 nm × 8 μm	3 μm × 60 μm
SQUID loop linewidth	1 μm	1 μm	2 μm	4 μm
Pickup loop dimension	400 μm × 400 μm	400 μm × 400 μm	400 μm × 400 μm	10 mm × 10 mm
I_c [μA]	100	100	100	50
R [Ω]	2	2	2	3.5
$\triangle V$ [μV]	23.7	9.6	4.4	43.8
Simulated L_{SQ} [pH]	65	102	178	60
Simulated A_{eff} [mm^2]	0.6 $\times 10^{-3}$	3.3 $\times 10^{-3}$	6.1 $\times 10^{-3}$	0.24
Measured A_{eff} [mm^2]	0.5 $\times 10^{-3}$	2.9 $\times 10^{-3}$	5.9 $\times 10^{-3}$	0.24
Measured $S_\Phi^{1/2}$ [$\mu\Phi_0/\sqrt{\text{Hz}}$]	10	30	55	5
Measured $S_B^{1/2}$ [fT/$\sqrt{\text{Hz}}$]	4 $\times 10^4$	2.1 $\times 10^4$	1.9 $\times 10^4$	40

A systematic study of the dependence of the effective area on the SQUID slit length ($\sim L_m$) was performed based on the Type III design. Here the devices under test had the same pickup loop dimension of 7 mm × 7 mm and pickup loop linewidth of 50 μm. The SQUID loops had the same slit width of 0.5 μm and loop linewidth of 2 μm while the SQUID slit lengths were 2, 4, 8, 16 and 32 μm, respectively. A linear dependence in agreement with the expression $A_{eff} \approx A_{eff}^{pk} L_m / L_{pk}^{SQ}$ was observed as shown in Fig. 3.2. With increasing SQUID slit length, L_m increased but β_L also increased much above optimal value 1, which led to a small voltage modulation depth for the SQUID. With a voltage modulation depth lower than 2 μV, it is difficult to lock the SQUID with FLL using Magnicon SEL-1 SQUID electronics. For lockable devices we calibrated the effective areas by measuring the field generated by a Helmholtz coil while SQUIDs were locked at the working point with the maximum flux-to-voltage transfer coefficient. For unlockable devices we estimated the effective areas by evaluating the field needed to generate one flux quantum in the SQUIDs, which was less accurate because

the flux-to-voltage transfer coefficient was not fixed.

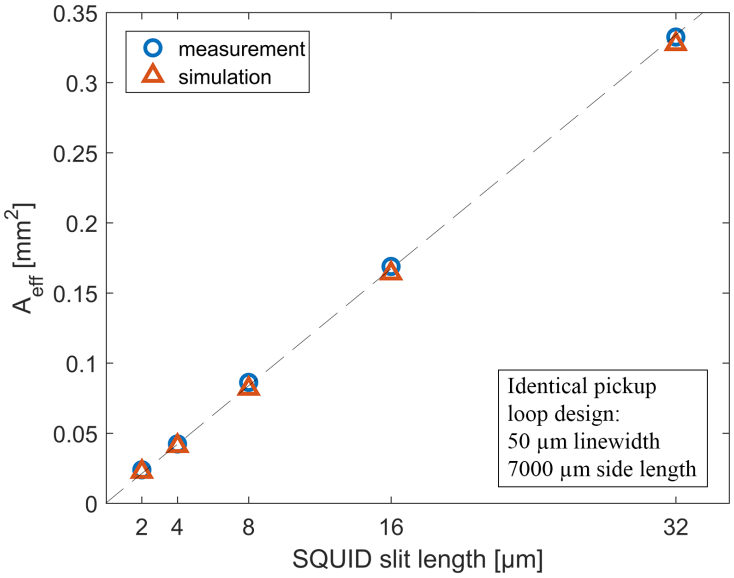

Figure 3.2: The measured (blue circle) and simulated (red triangle) effective areas of nanowire-based SQUID magnetometers with different SQUID slit lengths and the same pickup loop design (parameters shown in the inset). The dashed line serves as a guide to the eye.

3.1.1.2 The pickup loop

A similar study of the dependence of the effective area on the pickup loop side length was performed based on the Type III design (design shown in Fig. 3.3a). Here the tested devices had the same SQUID loop design with the slit width of 0.5 μm, slit length of 8 μm and loop linewidth of 2 μm. The pickup loops had a linewidth of 50 μm and side length of 300, 400, 2000, 4000, 7000, and 7500 μm, respectively. The linear dependence found in Fig. 3.3a also agrees with $A_{eff} \approx A_{eff}^{pk} L_m / L_{pk}^{SQ}$ because A_{eff}^{pk} is proportional to the square of the side length and L_{pk}^{SQ} is proportional to the side length. However, the pickup loop side length cannot be infinitely increased because of the substrates size limit and the sensor array layout requirements for optimal full-head coverage when it comes to MEG applications. The best achieved effective area of lockable nanowire-based SQUID magnetometers with a directly connected pickup loop was 0.09 mm^2 with the SQUID slit length of 8 μm and pickup loop side length of 7500 μm. With a flux noise of 55 $\mu\Phi_0/\sqrt{\text{Hz}}$, the magnetic field sensitivity of this device was 1.2 pT/$\sqrt{\text{Hz}}$.

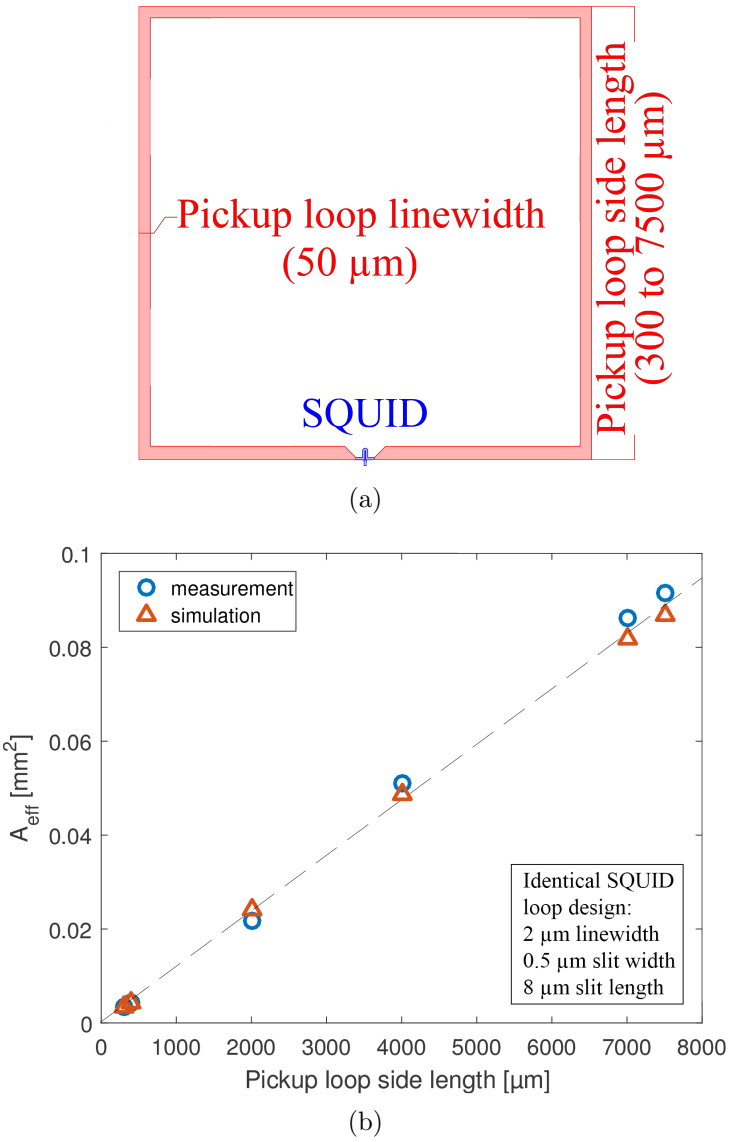

Figure 3.3: (a) Sketch of the SQUID magnetometer with a directly connected pickup loop. (b) The measured (blue circle) and simulated (red triangle) effective areas of nanowire-based SQUID magnetometers with different pickup loop side lengths and the same SQUID loop design (parameters shown in the inset). The dashed line serves as a guide to the eye.

3.1.1.3 Nanowire-based SQUIDs with different film thicknesses

As discussed above, the kinetic inductance gives an important contribution when dimensions become extremely small. In order to alleviate some of the design problems, we investigated the possibilities in using structures of different film thicknesses, i.e., only specific parts in the design are 50 nm thick (preferably just the nanowire junctions) and the rest of the structures

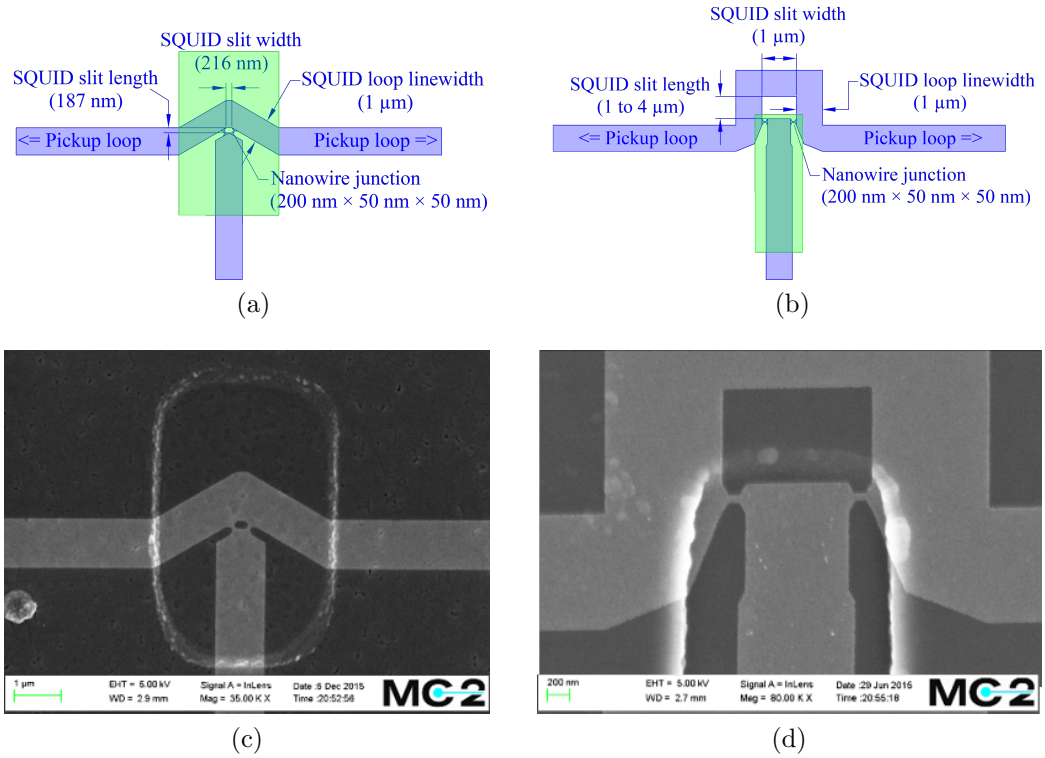

Figure 3.4: Sketches and SEM pictures of the SQUID loop areas of the type I ((a) and (c)) and type II ((b) and (d)) nanowire-based SQUID magnetometers with different thicknesses, respectively. The green shadowing parts in (a) and (b) indicate the trenches opened for etching down the 200 nm thick films to 50 nm.

are 200 nm thick or more. The local 50 nm area/trench was etched down from a 200 nm film through an S1813 photoresist mask using a low-rate Ar^+ ion milling process with liquid nitrogen cooling. The aim of this design was to eliminate the influence of kinetic inductance and thus enhance the coupling. For example, as shown in Fig. 3.4a and 3.4c, the Type I SQUID loop was 50 nm thick and the pickup loop was 200 nm thick. With this design, the kinetic inductance of the pickup loop could be reduced by a factor of two at 77 K. However, unlike the nanostructures, the geometric inductance of wide structures (e.g., pickup loop with a loop linewidth of 50 μm) is 10 times greater than the kinetic inductance, which made the reduction of kinetic inductance not important for the effective area. Another example on the Type II SQUID is shown in Fig. 3.4b and 3.4d, only the nanowire junctions and the bottom electrode were 50 nm thick and the rest of the structures were 200 nm thick. Through this way, the kinetic term in the mutual inductance L_m was dramatically decreased and led to a smaller total SQUID inductance L_{SQ}. However, the coupling and the effective area also

dropped correspondingly. From this experiment, it was proved that both the kinetic and geometric inductances serve the same way for the coupling.

From these experiments, the concept and fabrication process developed for SQUIDs with different thicknesses is not promising. However, as it will be discussed in the Section 3.4, a nanowire-based SQUID with a thick washer is the most promising way to increase the magnetic field sensitivity. Nevertheless, a more systematic study and optimization are necessary to achieve a controllable processing technique for this type of devices.

3.1.2 Nanowire-based SQUIDs with an inductively coupled flux transformer

For this type of magnetometers, a multilayer flux transformer is implemented. Fig. 3.5 shows the design of the flux transformer used in this work, which is an updated version of those presented in Ref. [117]. With the use of chemical-mechanical polishing and a low angle Ar^+ ion beam milling in the fabrication, this flux transformer exhibits an 1/f noise corner below 10 Hz. The flux transformer pickup loop has an outer dimension of 10 mm $\times$ 10 mm and a linewidth of 1 mm. The flux transformer input coil has 12 turns with a linewidth of 7.5 μm and a line-to-line separation of 4 μm. The surface of the flux transformer chip is protected by a 1 μm Parylene layer. The backside of the flux transformer chip is polished to be transparent for the flip-chip alignment.

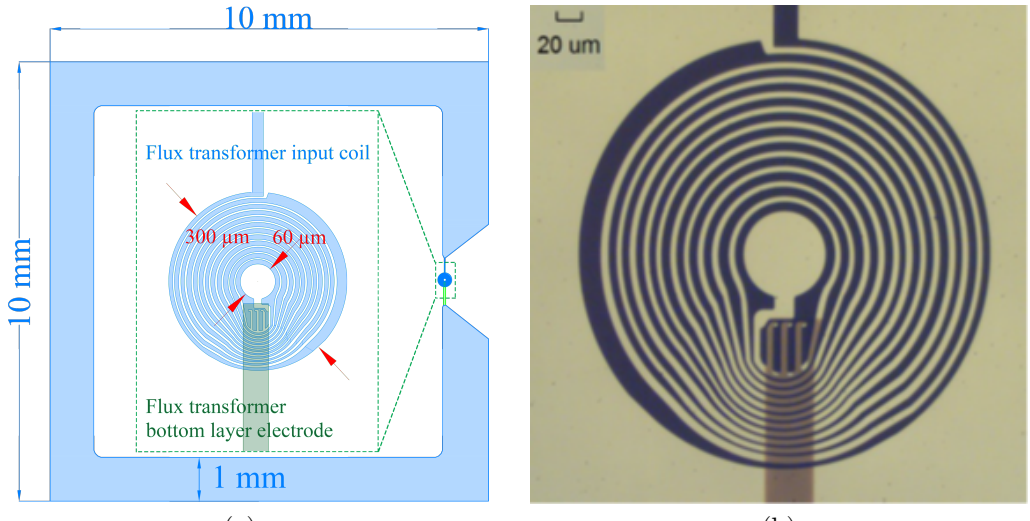

(a) (b)

Figure 3.5: (a) The design of the multilayer flux transformer with a close-up of the input coil region. (b) A microscopic picture of the flux transformer input coil region.

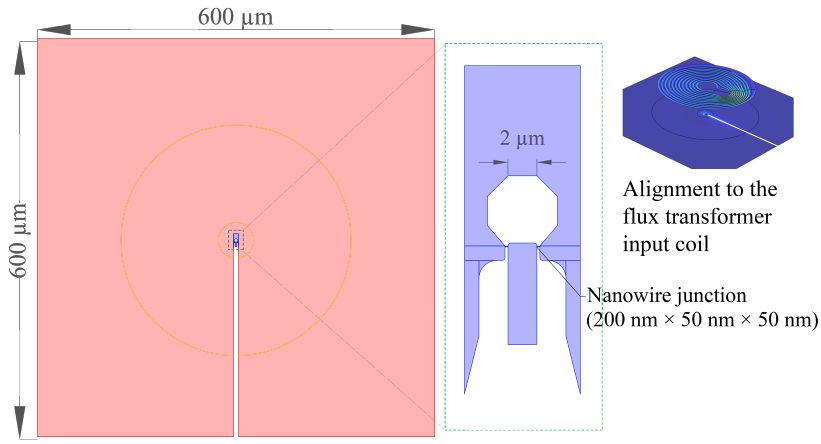

Figure 3.6: The design of a nanowire-based SQUID with washer to be used for the flux transformer. The green dashed box shows the close up of the SQUID region. The yellow circles are guidelines for the meshing process in the simulation. The inner and outer diameters of the flux transformer input coil are 60 μm and 300 μm, respectively.

The design of the nanowire-based SQUID is shown in Fig. 3.6. The SQUID washer was 600 μm × 600 μm. The SQUID hole diameter had a perimeter of 8 μm and a diameter of 5 μm, which resulted in a SQUID inductance of 144 pH from simulation. When mounting the flip-chip devices, the flux transformer chip was flipped and attached to the SQUID chip with BF2 glue. The separation between the two chips was estimated to be 3 μm (1 μm Parylene layer on the flux transformer chip and 1.3 μm protective S1813 layer on the SQUID chip, together with some gap).

Table 3.2: Measured and simulated parameters of a nanowire-based SQUID with an inductively coupled flux transformer.

Coupling approach	L_{SQ} [pH]	Flip-chip separation [μm]	k_{M1}	Measured A_{eff} [mm^2]	Simulated A_{eff} [mm^2]
Inductively coupled flux transformer	144	3	0.05	0.16	0.15

The measured and simulated parameters are summarized in Table. 3.2. The effective area was characterized to be 0.16 mm^2, which was not significantly better than the 0.09 mm^2 reached for devices with a directly connected pickup loop. The reason is that the 50 nm SQUID washer could not provide an efficient flux focusing effect as λ_L of our films is ~520 nm at 77 K [118, 119]. As a result, the coupling coefficient k_{M1} in Eq. 2.27 had a very small value (k_{M1} = 0.05 in this specific case). Note that k_{M1} is typically

0.8–0.9 for conventional high-T_c SQUIDs with thicker washers, the difficulty of coupling to the flux transformer is a unique problem for nanowire-based SQUIDs with thin washers. The flux noise of this device was 35 $\mu\Phi_0/\sqrt{\text{Hz}}$ with the low-frequency excess noise below 10 Hz, which gave a field sensitivity of 480 fT/$\sqrt{\text{Hz}}$.

3.1.3 Nanowire-based SQUIDs with a two-level coupling approach

To address the limits of the conventional magnetometer configurations for nanowire-based SQUIDs as discussed above, a two-level coupling approach is introduced. A sketch of the equivalent circuit is shown in Fig. 3.7. The idea behind this approach is that a better inductive coupling can be achieved between the SQUID chip and the flux transformer chip by connecting the SQUID to a washer-type pickup loop with an inner hole matching the inner diameter of the flux transformer input coil. As such, most of the flux generated by the input coil will go through the inner hole of the washer-type pickup loop. Note again that for the devices described in the previous section, i.e., SQUIDs with an inductively coupled flux transformer (one-level coupling), it relies on the film underneath the input coil to focus the flux into the SQUID hole. Also the two-level coupling has a smaller inductance mismatch in the inductive coupling than that in the one-level coupling (the washer-type pickup loop has a much larger inductance than the SQUID loop).

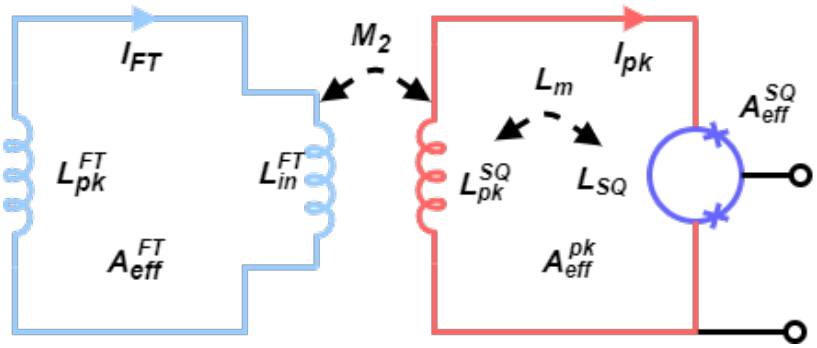

Figure 3.7: Equivalent circuit of the nanowire-based SQUID magnetometer with a two-level coupling approach. The SQUID has a directly connected washer-type pickup loop that is inductively coupled to a flux transformer.

The effective area of the two-level coupling devices is derived as below. The change of flux inside the SQUID loop with respect to the change of external magnetic field is $\delta\Phi_{SQ} = \delta B \cdot A_{eff}^{Mag} = -\delta\Phi_{SQ}^{SQ} + \delta\Phi_{SQ}^{cp}$ with $\delta\Phi_{SQ}^{SQ} = \delta B \cdot A_{eff}^{SQ}$ and $\delta\Phi_{SQ}^{cp} = L_m \cdot I_{pk}$. The change of flux inside the washer-type

pickup loop is $\delta\Phi_{pk} = \delta\Phi_{pk}^{pk} + \delta\Phi_{pk}^{cp} = I_{pk} \cdot L_{pk}^{SQ}$, where $\delta\Phi_{pk}^{pk} = \delta B \cdot A_{eff}^{pk}$ is the self-induced term and $\delta\Phi_{pk}^{cp} = M_2 \cdot I_{FT}$ is the inductively coupling term from the flux transformer. $M_2 = k_{M2} \cdot \sqrt{L_{in}^{FT} L_{pk}^{SQ}}$ is the mutual inductance between the flux transformer input coil and the washer-type pickup loop. The change of flux sensed by the flux transformer is $\delta\Phi_{FT} = \delta B \cdot A_{eff}^{FT} = I_{FT} \cdot (L_{pk}^{FT} + L_{in}^{FT})$. Combining these equations gives the effective area expression of SQUID magnetometers with the two-level coupling approach:

$$\begin{aligned} A_{eff}^{Mag} &= -\frac{\delta\Phi_{SQ}^{SQ}}{\delta B} + \frac{\delta\Phi_{SQ}^{cp}}{\delta B} = -A_{eff}^{SQ} + \frac{L_m}{L_{pk}^{SQ}} A_{eff}^{pk} \\ &+ k_{M2} \sqrt{\frac{L_{in}^{FT}}{L_{pk}^{SQ}}} \frac{L_m}{L_{pk}^{FT} + L_{in}^{FT}} A_{eff}^{FT} \approx \frac{k_{M2}}{2} \frac{L_m}{\sqrt{L_{in}^{FT} L_{pk}^{SQ}}} A_{eff}^{FT}. \end{aligned} \tag{3.1}$$

The last approximation is valid because the effective areas of the SQUID and washer-type pickup loops are much smaller than that of the flux transformer.

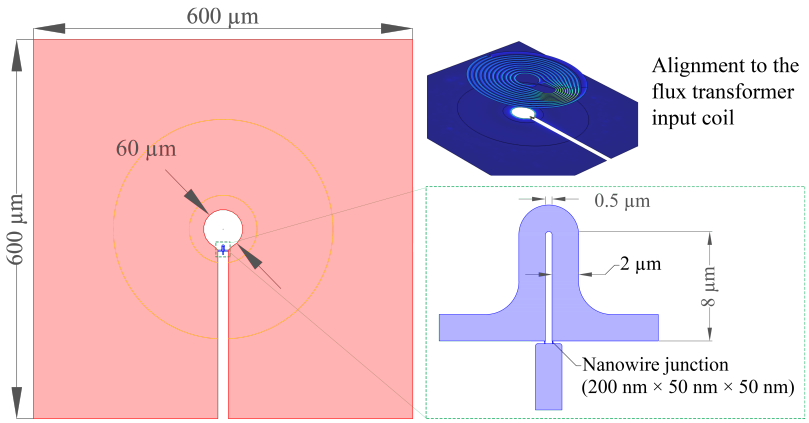

Figure 3.8: The design of a nanowire-based SQUID with the two-level coupling. The green dashed box shows the close up of SQUID region. The yellow circles are guidelines for the meshing process in the simulation. The inner and outer diameters of the flux transformer input coil are 60 μm and 300 μm, respectively.

The design of this type of SQUIDs is shown in Fig. 3.8. The SQUID was connected to a washer-type pickup loop with a dimension of 600 μm × 600 μm, which was chosen for comparing with the flip-chip device having a one-level coupling to the flux transformer described in the previous section. The SQUID loop design was the same as the Type III device with a directly connected pickup loop, i.e., 0.5 μm slit width, 8 μm slit length and 2 μm loop linewidth. The SQUID inductance was 178 pH from simulation. The measured and simulated parameters of this device are summarized in Table. 3.3.

As seen, the two-level coupling approach allowed the flip-chip device to have an effective area of 0.46 mm^2, which was about 2.6 times higher than that of the one-level coupling (0.16 mm^2) and 1.7 times higher than that of the single-layer bicrystal grain boundary SQUID magnetometer we fabricated (0.24 mm^2). With a flux noise of 55 $\mu\Phi_0/\sqrt{\text{Hz}}$, the magnetic field sensitivity of this device was 240 fT/$\sqrt{\text{Hz}}$.

Table 3.3: Measured and simulated parameters of a nanowire-based SQUID with the two-level coupling.

Coupling approach	L_{SQ} [pH]	L_{pk}^{SQ} [pH]	L_m [pH]	Flip-chip sep. [μm]	k_{M2}	Measured A_{eff} [mm^2]	Simulated A_{eff} [mm^2]
Two-level coupling	178	240	57	3	0.37	0.46	0.4

The dependence of the effective area on the pickup loop dimension was performed as well and the results are shown in Fig. 3.9. The devices exhibited similar effective areas (the higher measured value for the device with a 300 μm $\times$ 300 μm pickup loop might be due to a stronger pressing during flip-chip mounting and thus a smaller gap in between chips), which is because the inductance of a washer-type pickup loop L_{pk}^{SQ} depends mainly on the inner hole dimension. As a result, the effective area is not a function of the pickup loop side length according to Eq. 3.1.

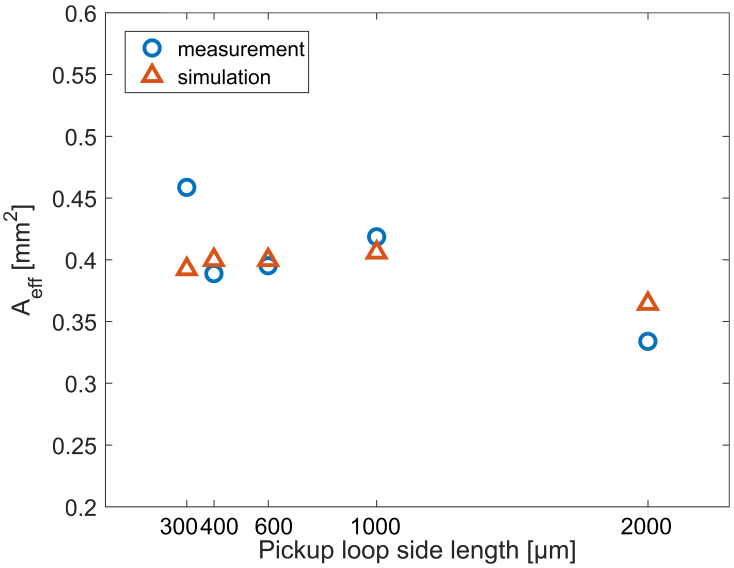

Figure 3.9: The measured (blue circle) and simulated (red triangle) effective areas of nanowire-based SQUID magnetometers utilizing the two-level coupling approaches with different pickup loop dimensions.

3.2 Fabrication of nanowire-based high-T_c SQUIDs

It is a challenge to prepare YBCO nanostructures with the superconducting properties close to the bulk because YBCO is extremely sensitive to the chemicals used in the patterning procedure and the oxygen content in the structures can be varied through the fabrication procedure due to sample heating. Several technologies have been reported to fabricate YBCO structures at the nanoscale, which include focused ion beam (FIB) milling [116, 120], atomic force microscopy (AFM) plowing [121], and e-beam lithography [122, 123]. Our method to fabricate the high-quality nanowire junctions with a critical current density approaching the Ginzburg-Landau (GL) theoretical depairing limit utilizing e-beam lithography was the same as reported in Ref. [52–54, 58, 124, 125]. In this thesis work, the fabrication process was adapted with minor changes to fabricate our nanowire-based SQUID magnetometers. The process is summarized as below and the modifications include a dual-exposure process to reduce the proximity effect in the e-beam lithography exposure and a liquid nitrogen cooling option introduced in the Ar^+ ion milling, which will be covered in more details in the following text.

Fig. 3.10 illustrates the main steps in the fabrication of the nanowire-based high-T_c SQUID magnetometers. First, a 50 nm YBCO film is deposited on an MgO (1 1 0) single crystal substrate using PLD (DCA instruments). After the deposition, the YBCO film is covered *in situ* with a 50 nm gold layer using magnetron sputtering (DCA instruments). Then an 80 nm diamond-like carbon layer was deposited on the sample in another PLD system. The carbon layer is patterned to form an ion milling mask using electron-beam lithography and oxygen plasma etching. Finally, a low-rate Ar^+ ion milling process ($\sim$ 5 Å/min) is used to etch the final device structures in the YBCO. The 50 nm capping gold is left on the structures.

This process works well for patterning nanostructures which do not have other larger structures close by. When it comes to nanowire-based SQUID magnetometers, larger structures (SQUID loop and pickup loop) need to be exposed nearby the nanowire junctions and the back scattering electrons from the substrate can cause the proximity effect problem. As a result, the patterned nanowire dimensions can be larger than designed. This effect is 10 times worse on an STO substrate than on an MgO substrate because of the stronger back scattering from heavy ions. To resolve this issue, a dual-exposure process is introduced when patterning the carbon mask, i.e., the e-beam lithography (steps (b) to (e) in Fig. 3.10) is executed twice.

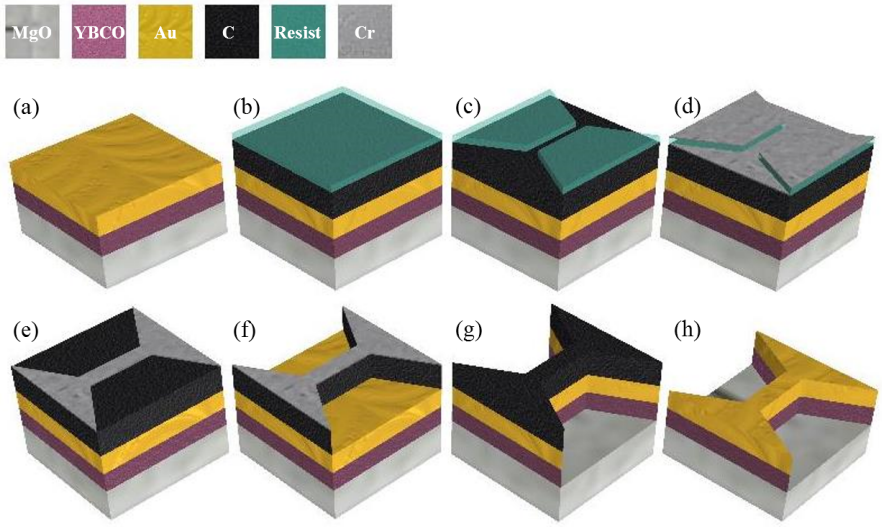

Figure 3.10: A sketch of the fabrication procedure of nanowire-based SQUID magnetometers. (a) On an MgO (1 1 0) single crystal substrate, a 50 nm YBCO film is deposited with PLD. After the deposition, a 50 nm capping Au layer is sputtered *in situ*. (b) An 80 nm diamond-like-carbon layer is deposited on the Au layer by PLD. Then a double layer of e-beam resist is spun on the chip (50 nm bottom layer of PMMA EL4 and 50 nm top layer of ARP 6200.13 1:1). Each sub-layer of the resist is baked at 95 °C for 5 min. (c) The pattern is exposed using an e-beam lithography. The top layer resist is developed in Hexyl acetate 99% for 25 s and rinsed in IPA. The bottom layer resist is developed in MIBK:IPA 1:3 for 40 s and rinsed in IPA. (d) A 12 nm Cr layer is deposited on the sample with e-beam evaporation at a rate of 1 Å/s. (e) A lift-off process of Cr is carried out in the remover 1165 at 60 °C. (f) A low-pressure O_2 plasma etching (30 W and 2 mTorr) is performed to strip the C that is not protected by the Cr layer. As such, a carbon mask is formed. (g) A low-rate Ar^+ ion milling process ($\sim$ 5 Å/min) is used to etch the structure with the C mask. (h) The remaining C layer is etched by a low-pressure O_2 plasma process (30 W and 2 mTorr).

The first lithography is for all the large structures in the design and the second lithography is purely for nanowire junctions with a small amount of surrounding structures ($\sim$a few μm, for alignment). With this method, nanowire junctions can be fabricated with almost 100% accuracy.

In the Ar^+ ion milling process (step (g) in Fig. 3.10), the 50 nm capping gold layer is essential for releasing the heat generated during the etching. When etching structures without the capping gold or preparing the trenches in YBCO films for the nanowire-based SQUIDs with different thickness (described in subsection 3.1.1.3), another way is required to avoid the degrading of superconducting properties in the films/structures due to heating. As an in-house solution, a liquid nitrogen cooling stage is implemented to allow cooling of the sample from the backside through thermally conductive vacuum grease. With this method, nanostructures preserving good superconducting properties without the capping gold layer can be fabricated.

3.3 Simulation of the inductances and effective areas

As shown, estimating the inductances is an essential task in the design of SQUID magnetometers. While it is convenient to rely on empirical formulas to calculate the inductances in a bicrystal grain boundary SQUID (film thickness is 250 nm, SQUID loop linewidth is a few μm and junctions are wider than 1 μm, i.e., the geometric inductance terms dominate and junction inductances are negligible), getting the right numbers for a nanowire-based SQUID is more complicated as the kinetic inductance terms need to be taken into account as well (film thickness is 50 nm, SQUID loop linewidth is ~ 1 μm and junctions are 50 nm wide). When it comes to estimating the coupling strength and effective area of the flip-chip devices, another difficulty arises from the fact that both the SQUID and the flux transformer are of complex and irregular geometries. To address these problems, a simulation method for numerically calculating the inductances and effective areas of multilayer superconducting devices using the COMSOL Multiphysics® software was developed. This method relies on the stream function formulation of the software package 3D-MLSI [126–129] that will be introduced below.

Assume there are N_s superconducting layers separated by insulating layers in a multilayer superconducting system and the m^{th} superconducting layer has a height of h_m, a thickness of t_m and occupies a space domain $V_m = S_m \times [h_m - t_m/2, h_m + t_m/2]$ (see Fig. 3.11), each superconducting layer can be treated as 2-dimensional if $t_m \lesssim \lambda_L^m$ and $t_m \ll l$ with λ_L^m as the London penetration depth of the m^{th} superconducting layer and l as the characteristic length of the device structure. As such, the current density $\boldsymbol{j}_{V_m}$ can be replaced with the sheet current density $\boldsymbol{j}_{S_m}(r) = t_m \cdot \boldsymbol{j}_{V_m}(r)$. A stream function $u_m(r)$ is defined for $\boldsymbol{j}_{S_m}(r)$:

$$j_{S_m,x} = \frac{\partial u_m(r)}{\partial y}, j_{S_m,y} = -\frac{\partial u_m(r)}{\partial x}. \tag{3.2}$$

Introducing the Pearl penetration length $\lambda_P^m = \lambda_L^{m2}/t_m$, the London equation $\lambda_L^{m2} \nabla \times \boldsymbol{j}_{V_m} + \boldsymbol{H} = 0$ and Maxwell equation $\nabla \times \boldsymbol{H} = \boldsymbol{j}_{V_m}$ can be combined and rewritten as:

$$\begin{aligned} -\lambda_P^m \triangle u_m(r_0) + \frac{1}{4\pi} \sum_{n=1}^{N_s} \iint_{S_n} (\nabla u_n(r), \nabla_{xy} G_{mn}(r, r_0))\, ds_n \\ = -H_{z,ext}(r_0), \end{aligned} \tag{3.3}$$

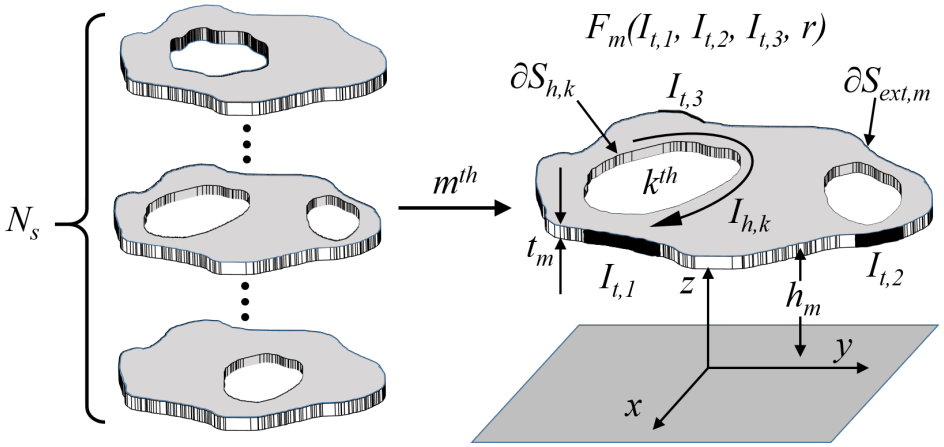

Figure 3.11: A sketch of a multilayer superconducting system with N_s superconducting layers and a close-up of the m^{th} layer showing boundary conditions.

in which the kernels $G_{mn}(r, r_0)$ have the forms:

$$G_{mn}(r, r_0) = \begin{cases} \left[|r - r_0|^2 + (h_m - h_n)^2\right]^{-\frac{1}{2}}, & n \neq m. \\ \frac{1}{2}\left(\frac{1}{|r-r_0|} + \frac{1}{\sqrt{|r-r_0|^2 + t_m^2}}\right), & n = m. \end{cases} \tag{3.4}$$

There are two types of boundary conditions: a circulating current $I_{h,k}$ around the k^{th} hole and a current distribution function $F_m(I_{t,1}, ..., I_{t,N_t}, r)$ defined by the excited currents through terminals on the m^{th} superconducting layer:

$$u_m(r) = \begin{cases} I_{h,k}, & r \in \partial S_{h,k}, k = 1, ..., N_h, \\ F_m(I_{t,1}, ..., I_{t,N_t}, r), & r \in \partial S_{ext,m}, m = 1, ..., N_s, \end{cases} \tag{3.5}$$

in which $\partial S_{h,k}$ is the boundary of the k^{th} hole, $S_{ext,m}$ is the external boundary of the structure on the m^{th} superconducting layer, N_h and N_t are the number of holes and terminals, respectively. The total energy functional of the system is a sum of the kinetic energy E_k and the geometric magnetic energy E_g for all the superconducting layers:

$$E = E_k + E_g = \frac{1}{2}\sum_{n=1}^{N_s} \iiint_{V_n} (\mu_0 \lambda_L^{n\,2} \boldsymbol{j}_{V_n}{}^2 + \boldsymbol{j}_{V_n} \cdot \boldsymbol{A}) dv_n, \tag{3.6}$$

in which $\boldsymbol{A}$ is the vector potential. E_k and E_g can be written with the stream function as:

$$E_k = \frac{\mu_0}{2}\sum_{n=1}^{N_s} \iint_{S_n} \lambda_P^n (\nabla u_n)^2 ds_n, \tag{3.7}$$

$$E_g = \frac{\mu_0}{8\pi} \sum_{n=1}^{N_s} \sum_{m=1}^{N_s} \iint_{S_n} \iint_{S_m} (\nabla u_n, \nabla u_m) G_{mn} ds_n ds_m, \tag{3.8}$$

Since the boundary problem (i.e., Eq. 3.3–3.5) is linear, the energy functional is positive quadratic with respect to the vector of current conditions $\boldsymbol{I} = (I_{h,1}, ..., I_{h,N_h}, I_{t,1}, ..., I_{t,N_t})$. Let $N = N_h + N_t$, then there exists an $N \times N$ inductance matrix $\boldsymbol{L}$ fulfilling:

$$E = \frac{1}{2}(\boldsymbol{LI}, \boldsymbol{I}). \tag{3.9}$$

By using proper boundary conditions, the elements of $\boldsymbol{L}$ can be extracted. First, the diagonal element L_{ii} (the self-inductance correlated with the i^{th} boundary condition) can be calculated by setting the i^{th} boundary condition to I_i and all other conditions to zero. The total energy E can be numerically solved with Eq. 3.6 and thus $L_{ii} = 2E/I_i^2$. Then the off-diagonal element L_{ij} (the mutual inductance between the i^{th} and j^{th} boundary conditions) can be calculated by setting the i^{th} and j^{th} boundary conditions to I_i and I_j, respectively, and all other conditions to zero. Again the total energy E can be numerically solved with Eq. 3.6 and $L_{ij} = (2E - L_{ii}I_i^2 - L_{jj}I_j^2)/2I_iI_j$. Since E_k and E_g in the energy functional can be separated, the kinetic and geometric inductances can also be calculated individually.

For the i^{th} hole on the m^{th} superconducting layer (e.g. the SQUID loop or the pickup loop), the field sensing effective area can be calculated by solving the magnetic moment with the stream function:

$$M = \frac{1}{2} \iint_{S_m} (x \cdot j_{s_m,y} - y \cdot j_{s_m,x}) dxdy = I_i \cdot A_{eff,i}. \tag{3.10}$$

Here the circulating current around the i^{th} hole is set to I_i and all other boundary conditions are set to zero.

Using this simulation method, we can calculate the inductances (kinetic and/or geometric), effective areas and current distributions of single-layer and/or multilayer devices. In particular, variable separation and rotation can be conveniently introduced to the simulation of multilayer flip-chip devices. Fig. 3.11a to 3.11d show the simulation of the two-level coupling approach with different flip-chip separations, where the magnetic field and currents on the washer-type pickup loop of the SQUID chip is induced by a current running in the flux transformer input coil. This models the actual coupling situation and the value of the stream function (color scale) represents the induced current distribution, i.e., the washer is mirroring the shape of the input coil when the flip-chip separation decreases. Another effect caused by

putting the two chips closer is that the inductance of the flux transformer input coil drops from the stand-alone value of 26 nH to around 20 nH when the separation gets down to a few μm. Since the flux transformer pickup loop inductance is designed to be 20 nH, the maximum effective area of the flux transformer is reached because the inductances of its input coil and pickup loop are equal now.

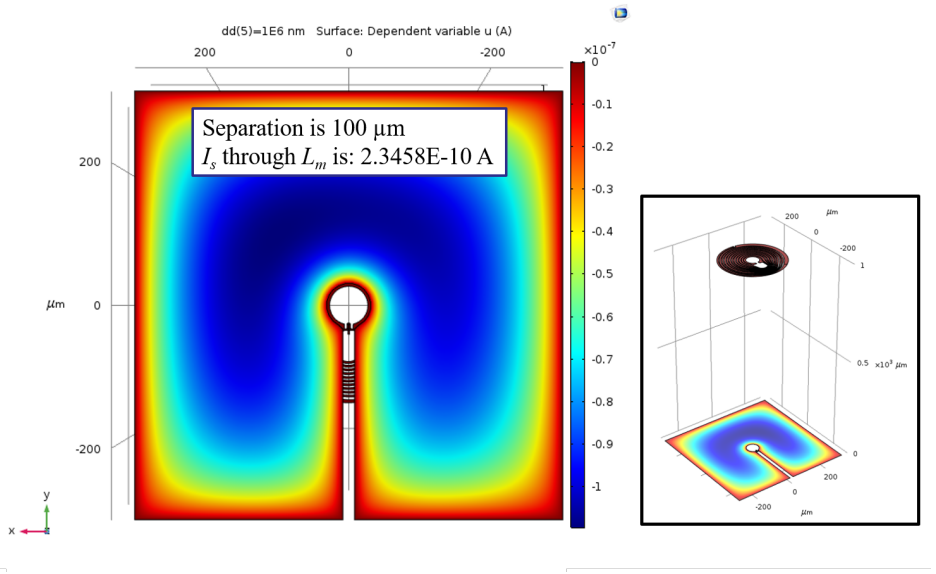

(a)

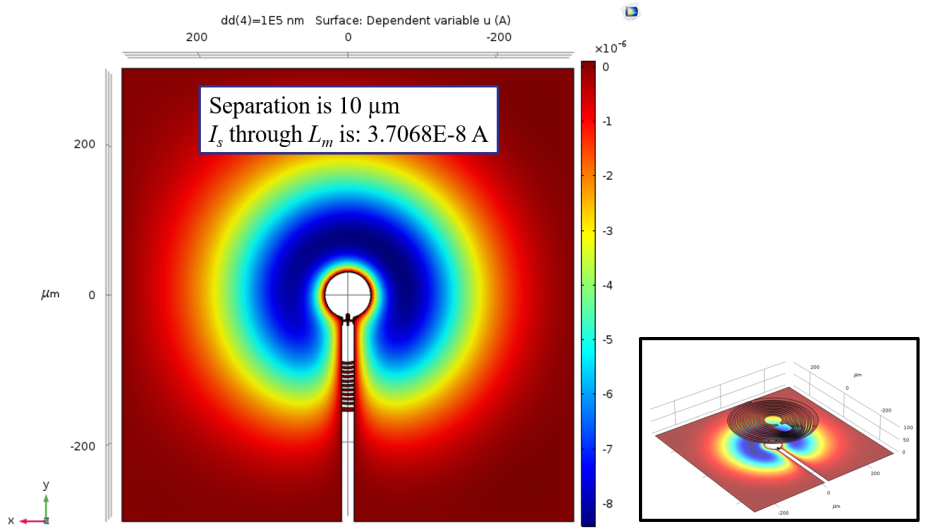

(b)

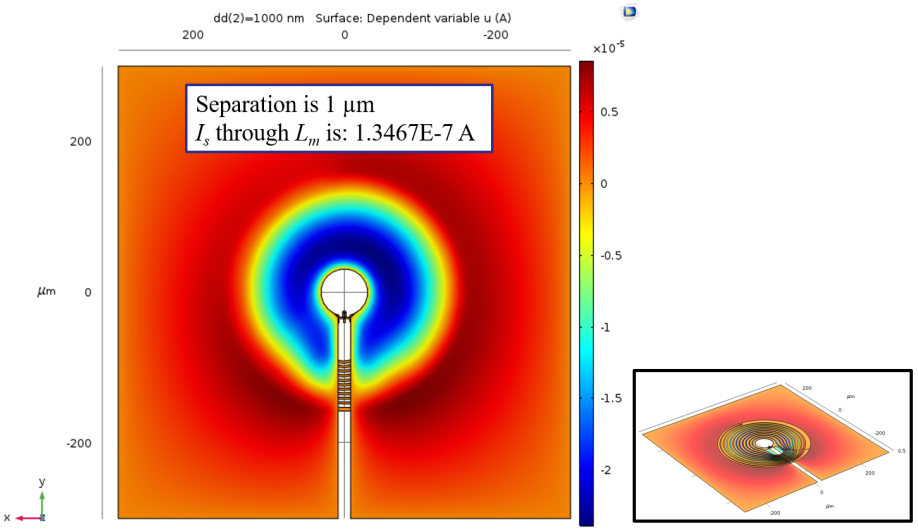

(c)

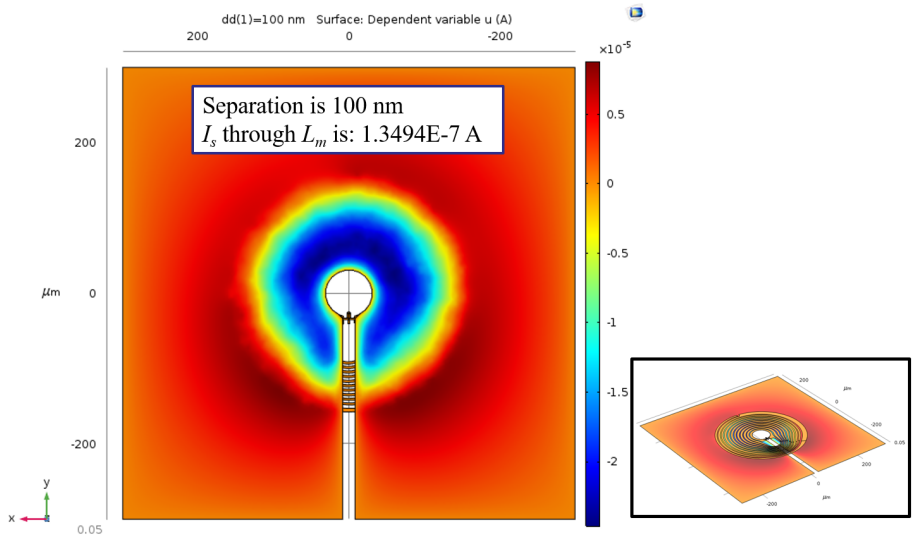

(d)

Figure 3.11: Simulations of the two-level coupling approach with different flip-chip separations. (a)–(d) are for 100 μm, 10 μm, 1 μm and 100 nm separations, respectively. The color scales represent the stream function values.

3.4 Results and discussion

To demonstrate and compare the performances of high-T_c nanowire-based SQUID magnetometers from the three coupling methods, one device from each method is picked out and the recordings of their magnetic flux and field noises are presented in Fig. 3.12. For the SQUID magnetometer with a directly connected pickup loop, the SQUID loop (L_{SQ} = 178 pH) is Type III in Fig. 3.1 with the slit width of 0.5 μm, slit length of 8 μm and loop linewidth of 2 μm and the pickup loop side length is 7500 μm. For the SQUID magnetometer with an inductively coupled flux transformer, the SQUID (L_{SQ} = 144 pH) is the one shown in Fig. 3.6 with an inner hole diameter of $\sim$ 5 μm and washer side length of 600 μm. For the SQUID magnetometer with a two-level coupling, the SQUID loop (L_{SQ} = 178 pH) is also Type III in Fig. 3.1 with the slit width of 0.5 μm, slit length of 8 μm and loop linewidth of 2 μm and it is connected to a washer-type pickup loop with the inner hole diameter of 60 μm and side length of 600 μm. The flux transformer utilized is the one shown in Fig. 3.5. The presented noise recordings were all taken inside an MSR at Chalmers using the bias reversal FLL mode of Magnicon SEL-1 SQUID electronics at 77 K. These flux noise levels match the L_{SQ} dependence plotted in Fig. 2.8. For the present configuration, i.e., the SQUID washer is of the same thickness as the nanowire junctions (50 nm), the best magnetic field sensitivity that can be achieved is 240 fT/$\sqrt{\text{Hz}}$ with the two-level coupling approach.

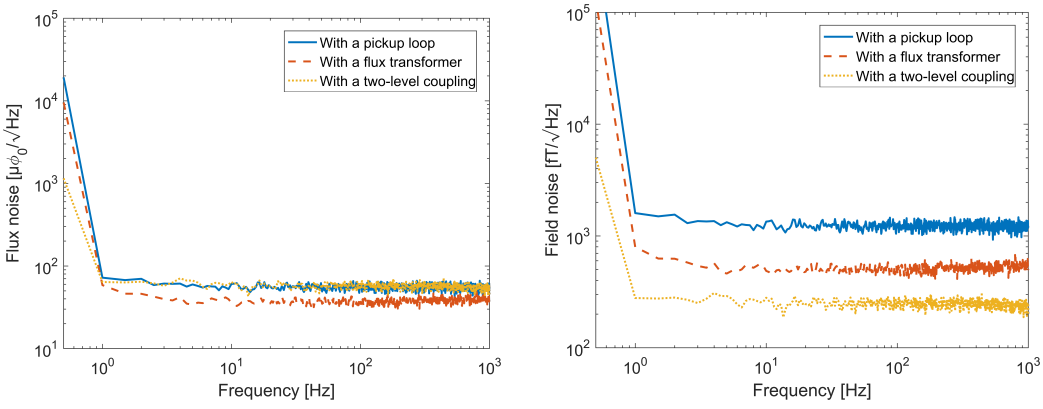

Figure 3.12: The noise performances at 77 K of selected devices from the three coupling methods. (a) The magnetic flux noise and (b) the magnetic field noise taken inside an MSR at Chalmers using the bias reversal FLL mode of Magnicon SEL-1 SQUID electronics.

Further enhancement of the magnetic field sensitivity can be pursuit from two aspects, i.e. reducing the flux noise by increasing the SQUID I_cR (see

Fig. 2.8) and increasing the effective area by having a thicker SQUID washer. A possible way to increase the SQUID I_cR product is to remove the capping gold layer on top of the nanowire junctions. This requires liquid nitrogen cooling to preserve the nanowire properties during the Ar^+ ion milling and some preliminary results at Chalmers showed that a four times higher I_cR product and a detectable flux noise limited by the preamplifier noise level were observed. The other approach to enhance the magnetic field sensitivity is to make nanowire-based SQUIDs with thicker washers (devices with different thicknesses). The coupling of flip-chip devices with the one-level coupling (only flux transformer) and two-level coupling (washer-type pickup loop and flux transformer) were simulated for 300, 1000, 3000, 1×10^4, 1×10^5, 1×10^6 nm flip-chip separations and 50, 200, 400 nm washer/washer-type pickup loop side length. The simulated effective areas and coupling coefficients (k_{M1} and k_{M2} for one and two-level coupling, respectively) are plotted in Fig. 3.13. As seen, the effective area of the one-level coupling devices can be increased from the present 0.15 mm^2 (3 μm separation with 50 nm washer) to 2.2 mm^2 (300 nm separation with 400 nm washer) while that of the two-level coupling devices does not improve too much with the increasing washer thickness. This is because the one-level coupling devices rely more on the flux focusing of the SQUID washer than the two-level coupling devices. By increasing the washer thickness, the one-level coupling coefficient k_{M1} increases by one order of magnitude (from 0.05 to 0.7) while the two-level coupling coefficient k_{M2} is less affected by it. The reason is again that k_{M1} is the coupling coefficient between the SQUID and the flux transformer input coil (a large inductance mismatch) while k_{M2} is the coupling coefficient between the washer-type pickup loop and the flux transformer input coil (a relatively smaller inductance mismatch). Combing the potential enhancements from these two aspects (a reduced flux noise of $\sim 10\ \mu\Phi_0/\sqrt{\text{Hz}}$ and an increased effective area of 2.2 mm^2), a field sensitivity of ~ 10 fT$/\sqrt{\text{Hz}}$ can be projected. This could make nanowire-based high-T_c SQUID magnetometers very promising in the biomagnetic applications, e.g., on-scalp MEG as will be introduced in the next chapter.

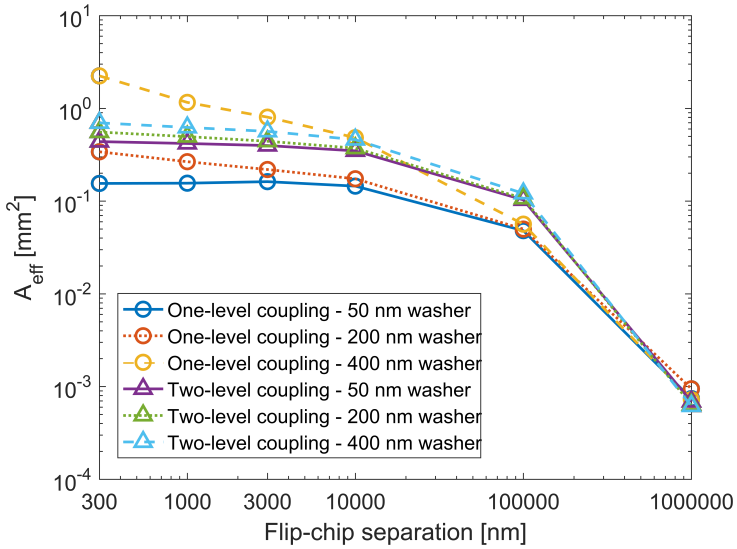

(a)

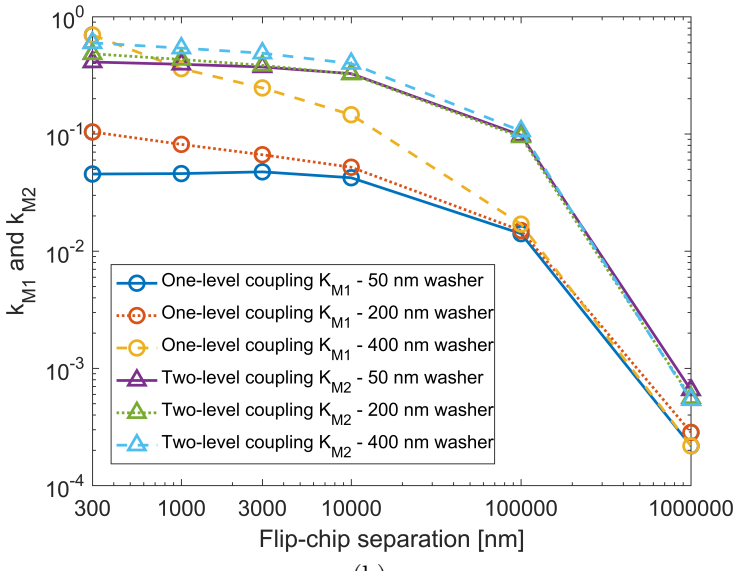

(b)

Figure 3.13: The simulation of flip-chip devices with the one-(circles) and two-level (triangles) coupling approaches with 50, 200 and 400 nm washers (solid, dotted, dashed lines, respectively) versus different flip-chip separations. (a) The effective areas and (b) the corresponding coupling coefficients k_{M1} and k_{M2}.

CHAPTER 4

On-scalp magnetoencephalography (MEG)

4.1 Introduction

Magnetoencephalography (MEG) is a technique to map the dynamics of neural activities in the human brain by measuring the weak magnetic fields generated by the currents flowing in the neural system [8, 130]. When a high enough number of aligned neurons ($\sim 5 \times 10^4$) are activated together, the current dipole strength is of the order of 10 nAm and a measurable signal ($\sim$100 fT) can be produced outside the head. The typical biomagnetic signals at the scalp are in the range of 50–500 fT [7], which require the use of ultra-sensitive magnetic field sensors. The pioneering work of MEG recording was carried out by David Cohen in 1968 with an induction-coil magnetometer [11] and in 1972 with a SQUID magnetometer [16]. The first multi-channel MEG systems were developed in the late 1980s and early 1990s [18–21]. State-of-the-art MEG systems these days typically consist of a helmet-shaped array of several hundred SQUID sensors (e.g. CTF MEG technology, Elekta (Neuromag® TRIUX) and Tristan Technologies (BabySQUID)). The SQUID sensors in the commercial MEG systems are generally low-T_c SQUIDs with a magnetic field sensitivity of 1–5 fT/$\sqrt{\text{Hz}}$ down to below 10 Hz [21].

MEG has the advantages of being noninvasive and passive, having reasonably high spatial accuracy ($\sim$mm) and excellent temporal accuracy ($\sim$ms). Electroencephalography (EEG) and functional magnetic resonance imaging (fMRI) have been widely used for both scientific and clinical purposes. EEG is a technique to detect the electric fields generated by the neural activities

with electrodes on the scalp [131], which provides a millisecond temporal resolution. However, the measured electric fields tend to be strongly distorted by the anisotropic conductivities in the skull and scalp, which makes the source localization more complicated and leads to a poor spatial resolution. On the contrary, magnetic fields have negligible effect from the surrounding head tissue and enable MEG to have a better spatial resolution in the millimeter range. fMRI is a technique to map neural activities by imaging the change in blood flow (hemodynamic response) [132], which also provides source localization power with a spatial resolution in the millimeter range. Nevertheless, the temporal resolution of fMRI is limited to around one second as it is an indirect measure of neuronal activities.

Despite the advantages of MEG, its clinical and neuroscience research utilization is limited because of the low-T_c SQUID sensors on which it is presently based, which require liquid helium (4 K) to reach the operating temperature. The large temperature difference between the low-T_c sensors and the room-temperature environment places a critical requirement on thermal insulation that results in a separation between the sensors and the neuron sources of interest to roughly 30 mm or more ($\sim$10 mm below the subject's scalp). In addition, it is costly to maintain and operate a commercial whole-head MEG as it boils off roughly 100 L of liquid helium per week. The present-day price for liquid helium is high and is expected to keep growing [41]. The consumption of liquid helium can be reduced by the installation of re-liquefier systems. However, this adds substantial investment costs and the liquefier may introduce both mechanical and magnetic noise.

Our aim has been to initiate what we hope will be a paradigm shift towards high-T_c SQUID-based MEG in which the sensors record the neuromagnetic field in close proximity to the subject's scalp. The main motivation for this is that such a system can be more cost effective and better than MEG systems of today. High-T_c sensors can be cooled by liquid nitrogen (77 K) and therefore the operation and maintenance costs can be lowered. Because of the decreased thermal isolation demand, the sensor-to-subject standoff distance can be reduced by more than one order of magnitude. This improved proximity opens the way for on-scalp MEG that will be discussed in the coming section.

4.2 On-scalp MEG

As introduced, state-of-the-art MEG systems do not support recording directly on the subject's scalp due to the heavy thermal insulation. The concept of "on-scalp" MEG, i.e., performing MEG recordings by placing sensors

in close proximity (few millimeters) to a subject's scalp, was recently proposed as the sensitivities of several helium-free sensor technologies reached the sensitivity level needed for MEG applications. Possible on-scalp MEG sensor technologies include high-T_c SQUIDs [35], optically pumped magnetometers (OPMs) [133], diamond nitrogen-vacancy center (NV center) magnetometers [134], giant magnetoresistance (GMR) magnetometers [135] and kinetic inductance magnetometers (KIMs) [136]. Among these technologies, recordings of spontaneous brain activities, auditory evoked fields (AEFs) and somatosensory evoked fields (SEFs) have been demonstrated with high-T_c SQUIDs [30–34] and OPMs [26, 36–39].

Reducing the sensor-to-subject distance leads to higher measurable signal amplitudes for MEG sensors as the neuromagnetic field decays rapidly as a function of the distance between the sources and sensors. Further to this, a variety of metrics quantifying the advantages of hypothetical on-scalp sensor arrays have been studied, which include the SNR, sensor lead fields, total information, source reconstruction accuracy, spatial resolution and spatial information density [23–25, 29, 137]. Several benchmarking experiments have been carried out to verify these metrics [26, 34, 37]. In this thesis work, benchmarking experiments utilizing high-T_c SQUID magnetometers were performed and are presented below.

4.3 Equivalent current dipole source model

The source localization problem of MEG is referred to as the inverse problem, which generally has no unique solution and relies on the models, constraints and corresponding assumptions. A popular source model in MEG research is the equivalent current dipole (ECD), which describes the synchronous postsynaptic currents in the dendrites of neurons in a cortical region. Here the current dipole is a point source with a moment $\boldsymbol{Q}$ at a location $\boldsymbol{r_0}$. The magnetic field $\boldsymbol{B}$ at a location $\boldsymbol{r}$ generated by such an ECD in an unbounded homogeneous conductor is given by the Biot-Savart law [138]:

$$\boldsymbol{B} = \frac{\mu_0}{4\pi}\boldsymbol{Q} \times \frac{\boldsymbol{r} - \boldsymbol{r_0}}{|\boldsymbol{r} - \boldsymbol{r_0}|^3}. \tag{4.1}$$

A MEG sensor at a location $\boldsymbol{r}$ only detects the magnetic field that is perpendicular to the sensor plane, which is the radial component of $\boldsymbol{B}$:

$$B_r = \boldsymbol{B} \cdot \frac{\boldsymbol{r}}{|r|}. \tag{4.2}$$

To simplify the problem without loss of generality, we can assume that the current dipole is on the z-axis at a height of a (i.e., $\boldsymbol{r_0} = (0,\ 0,\ a)$) with

a moment oriented along the x-axis (i.e., $\boldsymbol{Q}$ = (Q, 0, 0)). The geometry is shown in Fig. 4.1. As such, Eq. 4.2 can be rewritten with a spherical coordiante (r, θ, ϕ) [139]:

$$B_r = \frac{\mu_0}{4\pi} \cdot \frac{Qsin(\phi)}{r^2} \cdot \rho \cdot \frac{sin(\theta)}{(1 - 2\rho cos(\theta) + \rho^2)^{3/2}}, \tag{4.3}$$

in which $\rho = a/r$ and θ is the angle between the sensor position and the z-axis. The maximum value of B_r can be found at $\phi = \pm\pi/2$ and θ given by [140]:

$$cos(\theta) = \frac{1}{2\rho}(\sqrt{1 + 14\rho^2 + \rho^4} - (1 + \rho^2)). \tag{4.4}$$

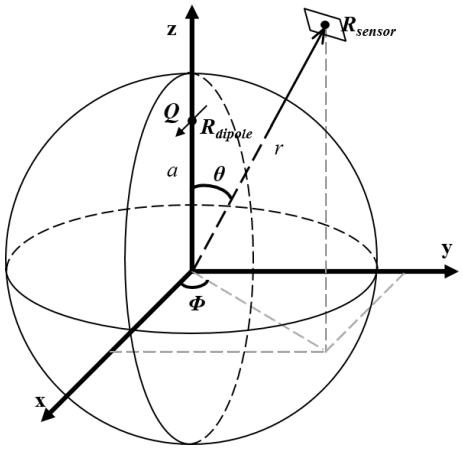

Figure 4.1: Sketch of the geometry of dipole source and sensor.

4.4 High-T_c SQUID-based MEG

Single-channel high-T_c SQUID-based MEG systems were developed. A zero field cooling environment is critical to the noise performance of the high-T_c SQUID operation and therefore the cooling of high-T_c SQUIDs was carried out inside a 2-layer magnetically shielded room (MSR) (Vacuumschmelze GmbH) at Chalmers. Fig. 4.2a shows the alignment of the high-T_c MEG system to the scalp of a seated subject in the MSR. The system was mounted on an arm of a wooden stand, which enabled it to be moved to arbitrary locations on the subject's scalp. A U-shaped headrest was utilized to help stabilize the head position of the subject. The internal design of the cryostat (ILK-Dresden) made of glass fiber reinforced epoxy is illustrated in Fig. 4.2b. The SQUID magnetometer was mounted onto a sapphire rod thermally connected to the 0.7 liter liquid nitrogen bath. A 200 μm

thick sapphire window separated the vacuum isolation inside the cryostat from the room temperature environment. After cooling down, three precise adjustment screws were used to manually bring the SQUID magnetometer close to the window and enable a sensor-to-subject separation of within 1 mm. Fig. 4.2c shows the front view of the sapphire window with the high-T_c SQUID magnetometer sitting underneath.

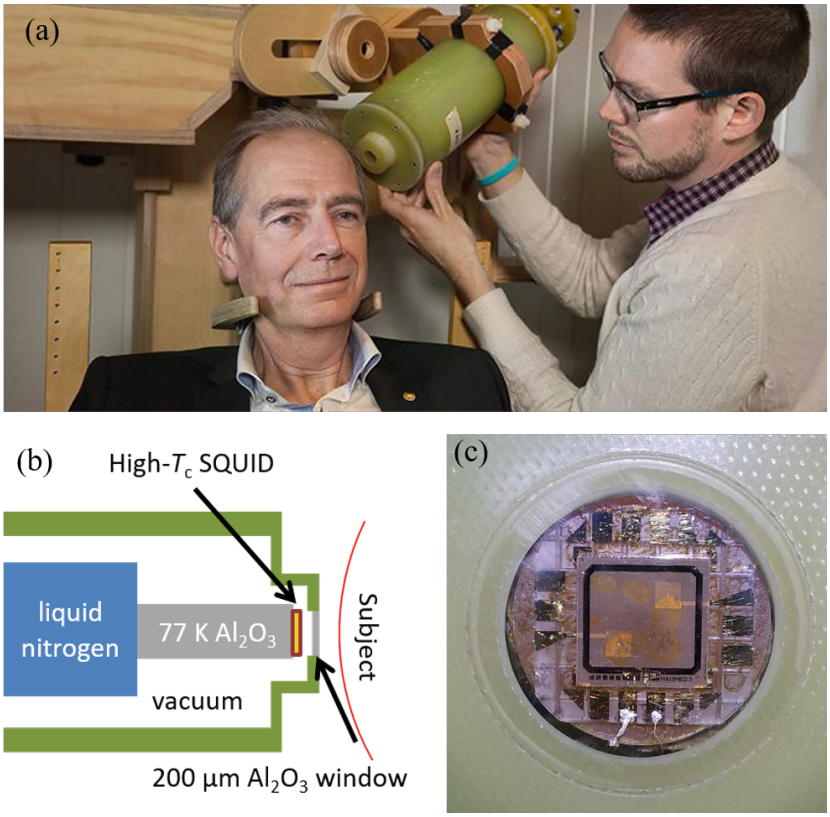

Figure 4.2: (a) A picture showing the alignment of the high-T_c SQUID-based MEG system to a subject's head in the MSR at Chalmers. (b) The inner configuration of the cryostat. (c) The front view at the sapphire window with the high-T_c SQUID magnetometer sitting underneath.

The sensor housed in the high-T_c SQUID-based systems was a single-layer thin film SQUID magnetometer with the hairpin-shaped design as described in Section 2.4.3. The pickup loop dimension of the SQUID magnetometer is 9 mm × 9 mm and the magnetic field noise is around 40 fT/$\sqrt{\text{Hz}}$ down to 10 Hz when operated in a flux-locked loop under bias reversal mode with Magnicon SEL-1 electronics. During MEG recordings, the liquid nitrogen bath was pumped by a PIAB COAX® vacuum pump to bring the temperature further below 77 K, typically 74 K.

LabVIEW programs were developed to perform the data acquisition using a data acquisition unit, NI-DAQ 6251. A SR560 low-noise voltage preampli-

fier was hooked up to enhance the signal before it was feed into the DAQ. Recorded data were processed using either the EEGLAB [141] or the FieldTrip [142] toolbox.

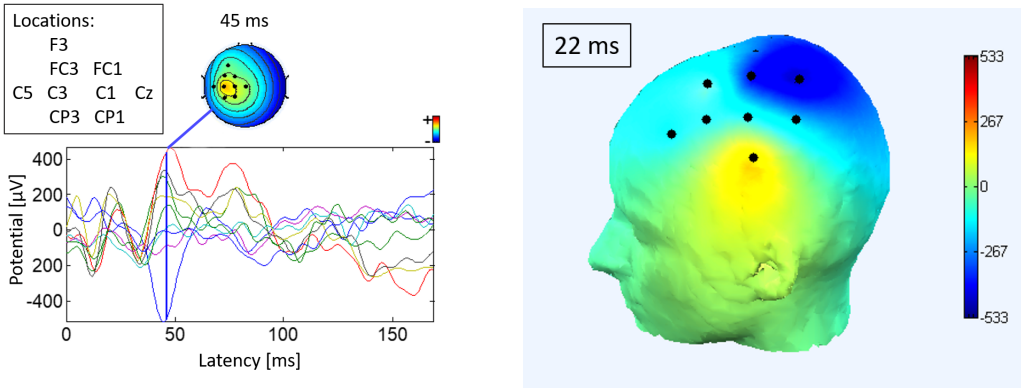

(a) (b)

Figure 4.3: (a) Recorded time traces (averaged over 400 trials) for SEF responses from nine measurement locations. The field distribution at 45 ms after the stimulus trigger is plotted. (b) The measured field distribution at 22 ms after the stimulus trigger is plotted on a 3-D head model.

SEF recordings were performed using the high-T_c SQUID-based MEG system. A GRASS S48 finger-shock stimulator was utilized to apply electrical stimuli to the median nerve of the subject. The stimuli were 10% below minimum thumb-twitching current and were applied in constant-current mode with a repetition frequency of 5 Hz and a duration of 2 ms. The nine measurement locations (see Fig. 4.3a) were chosen based on the International 10-20 EEG placement system. The recording on each location included around 400 stimuli and the high-T_c MEG system was manually moved to the next measurement location after each recording. The DAQ sampling rate was set to 1 kHz, the preamplifier gain was set to 1000 and a band pass filter of 0.1–300 Hz was applied. The recorded data were band-pass filtered at 1–100 Hz, segmented into trials according to the stimuli triggers and averaged. Fig. 4.3a shows the recorded time trace (averaged over 400 trials) of all the nine channels and Fig. 4.3b shows the reconstructed magnetic field distribution on the scalp.

4.5 Benchmarking experiments

To demonstrate the power of on-scalp MEG systems based on high-T_c SQUID magnetometers, we performed a series of benchmarking experiments with our system and a commercial low-T_c SQUID-based 306-channel MEG

system (Elekta Neuromag® TRIUX, courtesy of the National Infrastructure for Magnetoencephalography (NatMEG), Karolinska Institutet, Sweden). First, two phantoms with embedded artificial dipoles were utilized to characterize the performance of our high-T_c SQUID-based MEG system and to compare the signal-to-noise ratio (SNR) of our system and the NatMEG system. After that, we demonstrated the recordings of two types of stimulation evoked activities on a human subject with our system and the NatMEG system. Based on the results, we proposed an effective and general benchmarking protocol for sensor technologies at the developing stage, which usually have a limited number of channels and performing a full-head mapping can take a large amount of time [26, 34].

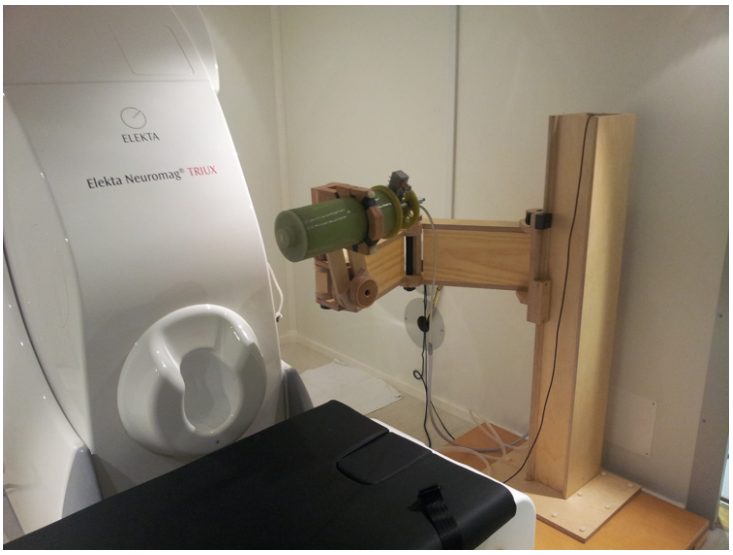

Figure 4.4: Elekta Neuromag® TRIUX together with the single channel high-T_c SQUID-based MEG system mounted on a wooden stand.

Fig. 4.4a shows the two MEG systems we benchmarked against each other. The low-T_c SQUID-based MEG system in the experiments was an Elekta Neuromag TRIUX, a widely used state-of-the-art MEG platform. A total number of 102 sensor chips (each with three low-T_c SQUIDs: one magnetometer with a 21 mm $\times$ 21 mm pickup loop and two orthogonal gradiometers with a 17 mm base length) were aligned in a helmet-shaped array. As discussed earlier, the shortest achievable sensor-to-subject distance for such a system was limited to 20 mm due to the sophisticated thermal isolation required. The system was located in a 2-layer MSR (Vacuumschmelze GmbH) at NatMEG. An integrated 128-channel EEG system could be operated simultaneously when performing full-head recordings.

4.5.1 Phantoms

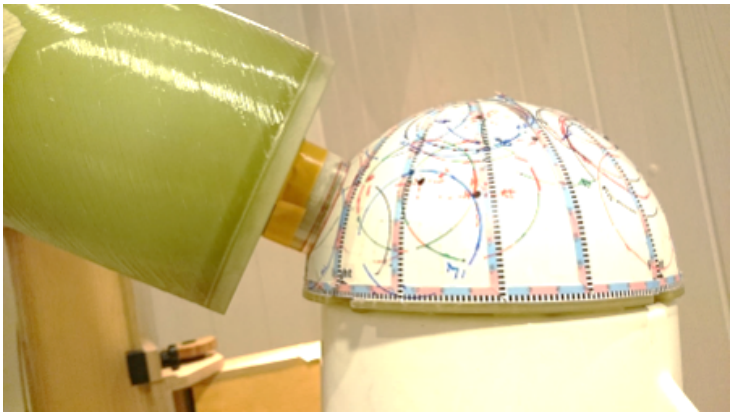

(a)

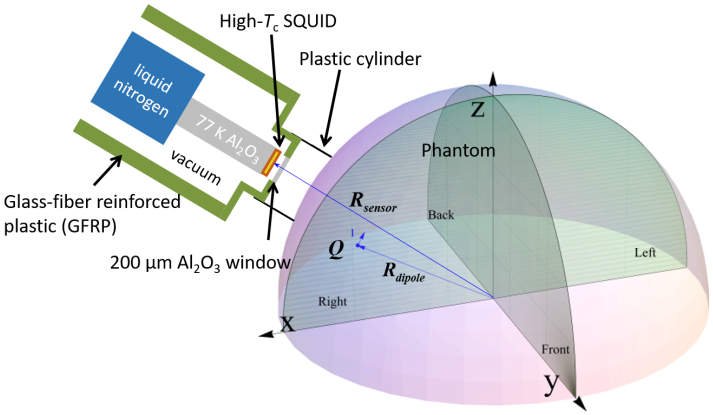

(b)

Figure 4.5: (a) Picture and (b) sketch of the experimental setup of phantom A and the high-T_c SQUID-based MEG system. The plastic cylinder surrounding the top end of the cryostat is used to define the sensor-to-subject separation and guarantee that the sensing axis of the high-T_c SQUID is radial with respect to the phantom's coordinate system.

The subjects under this study were phantoms provided by Elekta, which are half-spherical plastic models with an outer-shell radius of 87.5 mm (a typical value for a human adult). In the coordinate system of the phantom, two printed circuit boards (PCB) are placed on the xz- and yz-planes, respectively. Each PCB contains a series of artificial current dipoles tangentially aligned with respect to the phantom's origin. The length of the dipoles is 5 mm and the distances to the origin of four dipoles along the same radial direction are 34, 44, 54 and 64 mm, respectively. Such a system is designed to mimic the neural activities in human brains [143]. Four head-

position-indicator coils with fixed locations are used to register the phantom's coordinates before measurements.

Depending on the coordinates and momentum of a dipole, the location of the peak magnetic field on the phantom surface for each dipole can be calculated and marked (see Fig. 4.5. These measurement locations were registered using a 3-D digitizer with the head-position-indicator coils. Dipoles were activated in serial with an identical activation paradigm: 100 times with two periods of a 1000 nA·m (peak-to-peak) sinusoidal signal at 20 Hz with a 0.5 s repetition time. For the high-T_c MEG recordings, we manually moved the cryostat to the measurement location for each dipole activation. For the low-T_c MEG recordings, all channels were recording and the dipoles were activated sequentially in the same run.

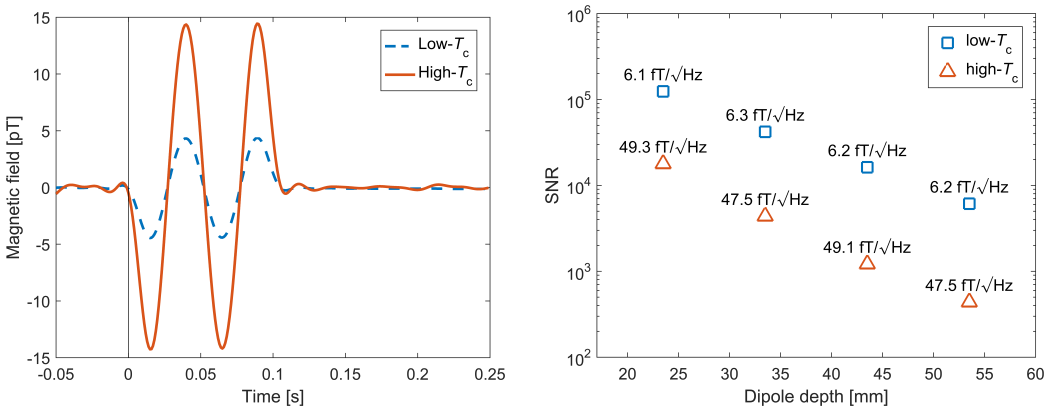

(a) (b)

Figure 4.6: (a) Comparison of signals (averaged over 100 trials) from a dipole (24 mm underneath the phantom shell) recorded by the high- (red solid) and low-T_c (blue dashed) MEG systems. The vertical black solid line indicates the trigger of dipole activation at 0 ms. (b) SNRs of the high- (red triangle) and low-T_c (blue square) MEG systems for different dipole depths.

An overall offset of less than 3% between the calculated and measured magnetic field values verified the performance of our high-T_c SQUID-based MEG system. As compared to the low-T_c recordings, the expected amplitude gain from the improved proximity was observed. Fig. 4.6a shows the comparison of signals from a dipole with a depth of 24 mm under the phantom shell. The SNRs of the high- and low-T_c SQUID-based phantom recordings with respect to the depths of the dipoles are presented in 4.6b. Because of the ∼8 times higher intrisic noise level, the high-T_c SQUID had lower SNRs compared with those of the low-T_c SQUIDs despite the 1–3 times higher measured field signals. While this is true for the single channel benchmarking, a denser array of high-T_c SQUID sensors with reduced standoff distances is expected to outperform the low-T_c array by providing higher total infor-

mation from brain activity as described in Ref. [23]. More details about the benchmarking experiments on phantoms can be found in appended paper II.

4.5.2 Human subjects

Benchmarking on human subjects is more challenging than on phantoms because the exact locations of sources are unknown. Usually the limited number of channels in the developing sensor technologies makes it difficult and time-consuming to perform a full-head mapping and source localization process. As a result, there is no direct way to benchmark a new MEG technology with the standard MEG at the system level. To overcome this obstacle, we introduced a measure G_{OS}, which is the ratio of the peak magnetic field available to on-scalp sensor technologies to that which is available to standard MEG sensors. In principle G_{OS} is a benchmarking parameter at the sensor level, but it also contains the system-level parameter, i.e., the sensor-to-subject standoff distance. The definition of G_{OS} is based on Eq. 4.3 and 4.4:

$$G_{OS} = \frac{B'_{r,max}}{B_{r,max}} = \frac{sin(\theta')}{sin(\theta)}(\frac{r}{r'})^3 \left(\frac{1 - 2\rho cos(\theta) + \rho^2}{1 - 2\rho' cos(\theta') + \rho'^2}\right)^{3/2}, \qquad (4.5)$$

where the prime symbol is used to indicate parameters of the new MEG technology and parameters without the prime symbol are for the standard MEG. In this specific case, we will use the subscripts H and L to refer to the high- and low-T_c cases, respectively).

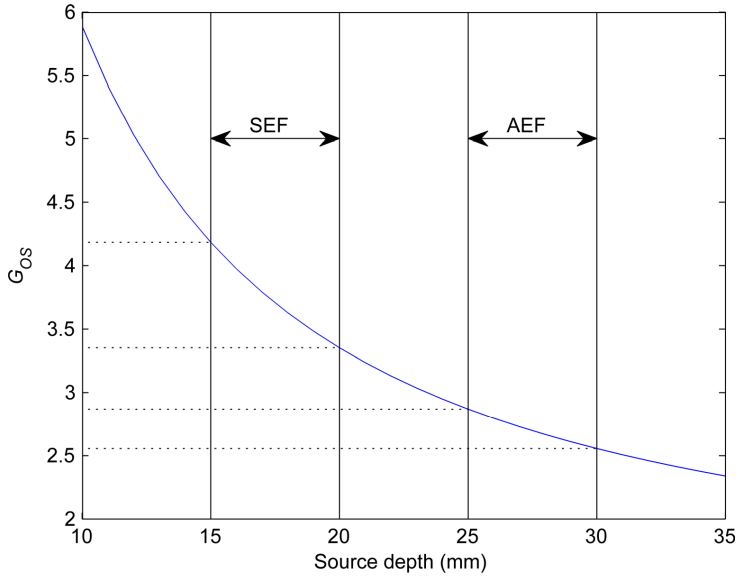

Figure 4.7: Calculated G_{OS} as a function of the source depth.

AEFs and SEFs, two well studied evoked-responses, were chosen for the benchmarking experiments on human subjects. We modeled the N100m (AEF) and the N20m (SEF) components because they are well described in literature and well accounted for by a single ECD. The typical source depths for SEFs and AEFs are indicated as 15–20 and 25–30 mm, respectively. The calculated G_{OS} is plotted as a function of the source depth in Fig. 4.7.

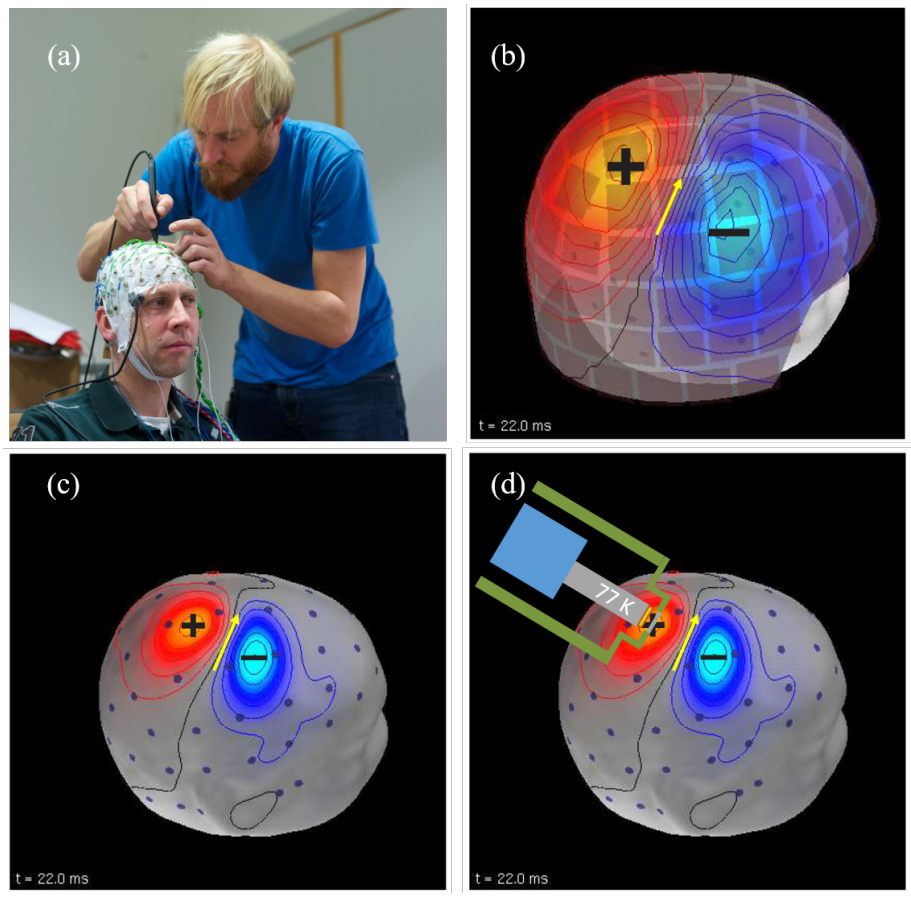

Figure 4.8: Benchmarking procedure. (a) Digitization of the EEG sensor locations on a subject. (b) The magnetic field distribution measured by the whole-head low-T_c MEG. The yellow arrow indicates the extracted ECD. (c) The calculated magnetic field generated by the ECD on the subject's scalp surface. (d) Recording with the high-T_c MEG by aligning it to the peak field locations (positive and negative peaks marked by the plus and minus signs, respectively).

For the SEF recordings, we applied electrical stimuli (10% below minimum thumb-twitching current (applied in constant-current mode)) to the median nerve with a repetition frequency of 2.8 Hz and a duration of 200 μs. For the AEF recordings, we applied auditory stimuli (1000 Hz tone) once per second with 400 ms duration. The details for these two stimulus paradigms can be found in appended paper III. The experiments were in compliance

with national legislation and the code of ethical principles (Declaration of Helsinki).

The benchmarking procedure for each stimulus paradigm is illustrated in Fig. 4.8. First, the EEG sensor locations (75 electrodes) on the subject's head were registered using a 3-D digitizer and the electrode cap remained on the subject's head throughout the experimental procedure (Fig. 4.8a). Then the spatial distribution of the magnetic field recorded with the low-T_c MEG sensors was plotted in 3-D at the peak latency of the SEF (around 20 ms) or AEF (around 100 ms), together with the 3-D rendered head surface and electrode positions (Fig. 4.8b). The corresponding ECD was determined and the positive and negative peak field positions on the subject's scalp were identified and marked (Fig. 4.8c). High-T_c MEG recordings on the marked positive and negative peak field positions were taken in sequence (Fig. 4.8d).

All data were bandpass filtered at 0.1–1320 Hz and sampled at 4 kHz. The post-processing procedure included a Butterworth bandpass filter at the relevant signal frequency range (1–60 Hz for AEFs and 1–500 Hz for SEFs) and a discrete Fourier transform (DFT) filtering process to remove power line interference. The filtered signals were segmented into trials according to the stimuli triggers and a visual inspection was executed to remove bad trials containing disturbances and artifacts. Disturbances can come from mechanical vibrations, power line interference (50/60 Hz), large metallic objects in motion (e.g., trams). Artifacts can come from heart beats, eye movements, eye blinks, movements, breathing and muscle activity of the subject. After removing bad trials, the rest of the good trials were averaged.

Fig. 4.9 and Fig. 4.10 are highlighted from appended paper III, which show the comparisons of recorded signals from the high- and low-T_c SQUID-based MEG systems. The simultaneous EEG recordings verified that the evoked responses are equivalent in all three MEG recordings (the "low-T_c", the "on-scalp positive peak," and the "on-scalp negative peak") for each stimulus paradigm. The average measured G_{OS} was 2.7 for AEF N100m (deep sources) and matched the expected range shown in Fig. 4.7 (Fig. 4.9). The SEF N20m responses (shallow sources), on the other hand, did not match the expectation. G_{OS} was well outside of the predicted range and also a biphasic activation was observed in the high-T_c recordings while a (typical) monophasic stimulus-induced activation was seen in the low-T_c recordings (Fig. 4.10). These features beyond the prediction of the ECD model indicate that SEFs are worthy of further study with high-T_c SQUID-based or other on-scalp MEG systems. Along the way, we developed a benchmarking protocol that can be used for other promising on-scalp MEG sensor technologies that is described in appended paper III.

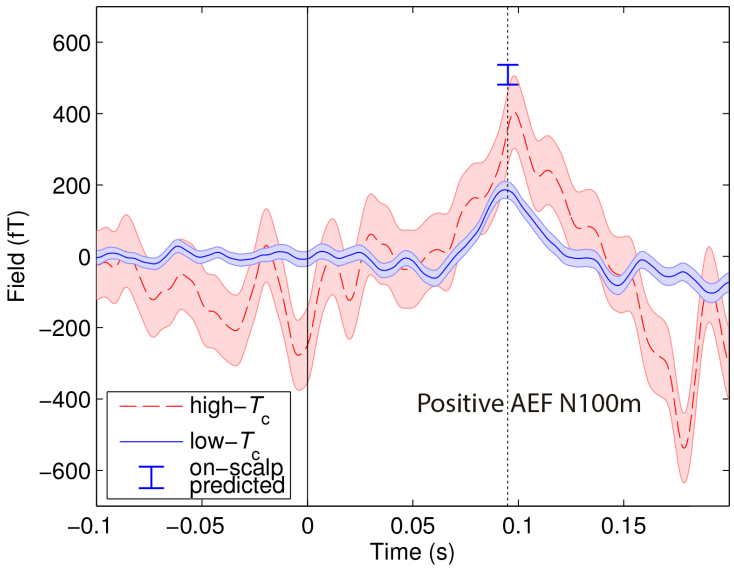

(a)

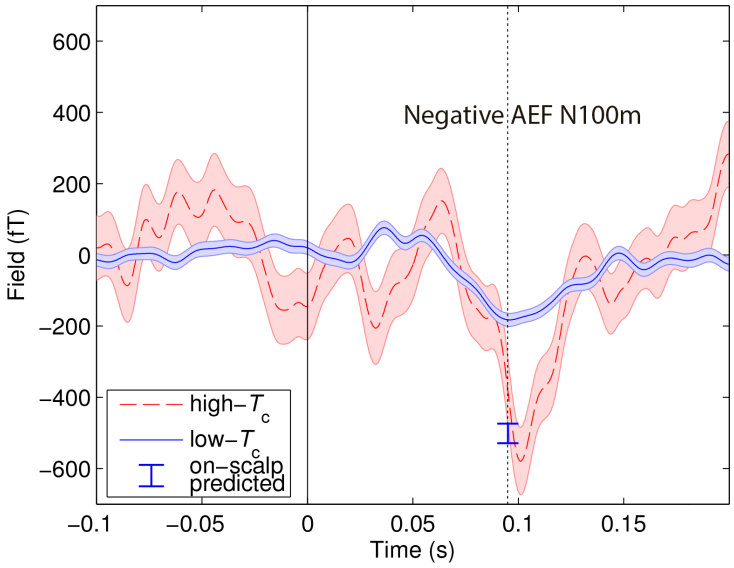

(b)

Figure 4.9: Recorded high- (red, dashed) and low-T_c (blue) SQUID time traces for the (a) positive (averaged over 458 trials) and (b) negative (averaged over 463 trials) AEF N100m peaks. The corresponding ± 1 standard errors are illustrated with shadows around the traces. The vertical black solid lines indicate the stimulus trigger at 0 ms and the vertical dotted lines indicate the positive/negative N100m peaks at 95 ms. The vertical blue bars indicate the range in expected field values for an on-scalp MEG sensor for the N100m AEF peak.

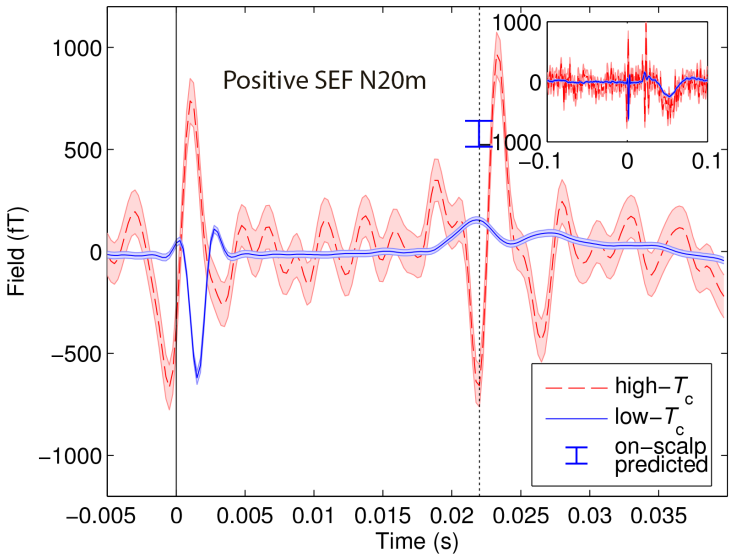

(a)

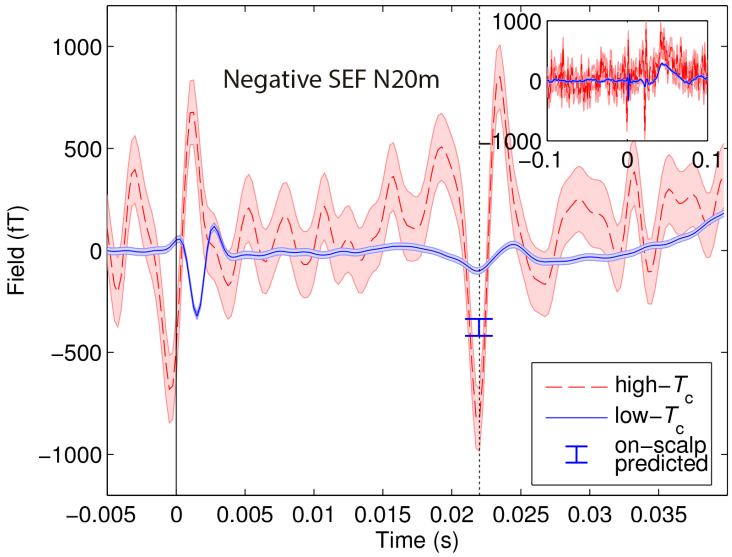

(b)

Figure 4.10: Recorded high- (red, dashed) and low-T_c (blue) SQUID time traces for the (a) positive (averaged over 583 trials) and (b) negative (averaged over 579 trials) SEF N20m peaks. The corresponding ± 1 standard errors are illustrated with shadows around the traces. The vertical black solid lines indicate the stimulus trigger at 0 ms. The ringing in both the high- and low-T_c traces near the 0 ms time point is from the stimulus artifact. The vertical blue bars indicate the range in expected field values for an on-scalp MEG sensor for the N20m SEF peak. The insets show the zoom-out time traces.

CHAPTER 5

Summary and outlook

High-T_c (YBCO) dc SQUID magnetometers based on bicrystal grain boundary junctions and nanowire junctions were developed and characterized. With the aim to substitute traditional low-T_c SQUID sensors the state-of-the-art MEG systems and enable on-scalp MEG applications, a variety of coupling approaches to increase the magnetic field sensitivities of SQUID magnetometers were studied. A magnetic flux noise of 5 $\mu\Phi_0/\sqrt{\text{Hz}}$ down to 10 Hz and an effective area of 0.24 mm^2 were achieved with single-layer bicrystal grain boundary junction SQUID magnetometers with a 9 mm $\times$ 9 mm pickup loop, which resulted in a magnetic field sensitivity of 40 fT/$\sqrt{\text{Hz}}$. These devices were employed in constructing the high-T_c SQUID-based MEG system that was used in the benchmarking MEG experiments. In the case of nanowire-based high-T_c SQUID magnetometers, the challenges and limits in the coupling due to the high junction inductances and thin SQUID washers were investigated and addressed. A two-level coupling approach including both a galvanically coupled pickup loop and an inductively coupled flux transformer was implemented, which brought the effective area of nanowire-based devices up to 0.46 mm^2. With a magnetic flux noise level of 55 $\mu\Phi_0/\sqrt{\text{Hz}}$, the best magnetic field sensitivity we achieved was 240 fT/$\sqrt{\text{Hz}}$ down to 10 Hz (two orders better than the highest value previously reported on nanowire-based devices in the literature [58]). Such a sensitivity is not yet adequate to compete with the low-T_c SQUIDs or other on-scalp sensor technologies. However, with the obtained knowledge and based on simulation and some preliminary experimental results, a magnetic field sensitivity of down to $\sim$10 fT/$\sqrt{\text{Hz}}$ can be projected in a nanowire-based device with thicker washer

and without capping gold. Except for the SQUID itself, SQUID electronics with a flux modulation scheme instead of a direct readout scheme can be used to accommodate the preamplifier noise contribution caused by the small modulation depth $\triangledown V$ in nanowire-based devices. For this purpose, SQUID electronics from Cryoton and Star Cryoelectronics were being considered and tested.

Benchmakring experiments between the single-channel bicrystal high-T_c SQUID-based MEG system and low-T_c SQUIDs in a Elekta Neuromag® TRIUX MEG system (courtesy of NatMEG) were carried out on both head phantoms and human subjects. A systematic benchmarking procedure that is objective, fast, and feasible for application to various on-scalp MEG sensing technologies was established and presented with MEG recordings of auditory and somatosensory evoked fields on one human subject. It was shown that the expected gain of measurable signal amplitude associated with on-scalp sensors could be obtained using high-T_c SQUID magnetometers. While the present single-channel SNR of the high-T_c sensor was not as good as that of the low-T_c counterpart, a dense array of on-scalp sensors with reduced sensor-to-subject distances was theoretically demonstrated to provide a larger total information [23, 29, 137]. A thorough review on the high-T_c SQUID-based biomedical applications including MEG and magnetocardiography (MCG) can be found in a recent publication [35], which indicate the advantages and motivations to develop multi-channel high-T_c SQUID-based MEG systems.

A seven-channel high-T_c SQUID-based MEG system is being built in our group at Chalmers. In this system, seven single-layer thin film SQUID magnetometers with a 9 mm $\times$ 9 mm pickup loop are arranged in a dense hexagonal pattern (the edge-to-edge distance is 2 mm). This cryostat is similar to that of the single-channel system with respect to sensor-to-subject distances of less than 3 mm. We have performed a cross-talk study on different types of feedback solutions and demonstrated that direct injection of feedback current into the SQUID loop can provide high enough coupling for the FLL while presenting a low cross-talk below 0.5% even for the minimal possible separation where the substrates of the SQUIDs are in contact with each other [27]. Once this seven-channel system is ready for use, system-level metrics like the total information, source reconstruction accuracy and spatial resolution will be benchmarked and compared to the theoretical results. The development of high-T_c SQUID MEG sensors, together with the fast development of OPM MEG sensors [24–26, 37], pave the way for a new era of on-scalp MEG applications.

Acknowledgments

Time flies and things change, like the PLD parameters and YBCO film qualities. And yet, my sincerest gratitude to those people who made this thesis work ever possible remains the same.

First of all, I would like to thank my examiner and main supervisor Dag Winkler for giving me the opportunity to work with such an interesting field and for always being patient, inspiring and supportive in guiding me through the research.

Also I wish to thank my co-supervisors, Justin Schneiderman and Alexey Kalabukhov, for teaching me a lot of valuable knowledge and experimental techniques, advising and supporting me in the lab, as well as helping me with article composition.

I am really grateful to Maxim Chukharkin, for all his time and efforts in teaching me clean room techniques, working together with me, encouraging me and telling me that "life is life" and "we have what we have".

Many thanks go to Floriana Lombardi, Thilo Bauch, Riccardo Arpaia, Marco Arzeo and Reza Baghdadi for their great help, nice collaboration and valuable discussion in the work of nanowire-based devices.

Also I would like to thank Daniel Lundqvist, Stephen Whitmarsh, Matti Hämäläinen, Viekko Jousmäki and Robert Oostenveld for all the collaborative work and valuable input in the benchmarking MEG experiments.

I wish to express my gratitude to all the clean room staff, in particular Henrik Frederiksen, Mats Hagberg and Bengt Nilsson, for their tremendous assistance in optimizing the fabrication process.

I want to thank Lars Jönsson for his great technical support in the workshop and Susannah Carlsson, Maria Tremblay and Debora Perlheden for their administrative support.

Special thanks go to Bushra Riaz, Silvia Ruffieux, Christoph Pfeiffer and Sobhan Sepehri for being my friends, teammates and coworkers. PhD experience without you would have been so much more boring.

I am thankful to all the past and present colleagues at QDP for creating the nice atmosphere and environment to work in. I wish to thank all my excellent friends for accompanying and supporting me.

Finally, I want express my warm gratitude to my parents for their love, encouragement and support. Special thanks go to my beloved wife Yao for lighting up my entire life.

Bibliography

[1] R. Hari and R. Salmelin. Magnetoencephalography: From SQUIDs to neuroscience. *Neuroimage*, 61:386–396, 2012.

[2] M. E. Raichle. A brief history of human brain mapping. *Trends Neurosci.*, 32(2):118–126, 2009.

[3] J. T. Cacioppo, L. G. Tassinary, and G. G. Berntson. *Handbook of Psychophysiology*. Cambridge University Press, Cambridge, 2007.

[4] J.-M. Schoffelen and J. Gross. Source connectivity analysis with MEG and EEG. *Hum. Brain Mapp.*, 30(6):1857–1865, 2009.

[5] J. S. George, C. J. Aine, J. C. Mosher, D. M. Schmidt, D. M. Ranken, H. A. Schlitt, C. C. Wood, J. D. Lewine, J. A. Sanders, and J. W. Belliveau. Mapping function in the human brain with magnetoencephalography, anatomical magnetic resonance imaging, and functional magnetic resonance imaging. *J. Clin. Neurophysiol.*, 12(5):406–431, 1995.

[6] C. J. Aine. A conceptual overview and critique of functional neuroimaging techniques in humans: I. MRI/FMRI and PET. *Crit. Rev. Neurobiol.*, 9(2-3):229–309, 1995.

[7] M. Hämäläinen, R. Hari, R. J. Ilmoniemi, J. Knuutila, and O. V. Lounasmaa. Magnetoencephalography—theory, instrumentation, and applications to noninvasive studies of the working human brain. *Rev. Mod. Phys.*, 65(2):413–497, 1993.

[8] P. C. Hansen, M. L. Kringelbach, and R. Salmelin. *MEG: An Introduction to Methods*. Oxford University Press, Oxford, 2010.

[9] M. S. Hämäläinen and J. Sarvas. Realistic conductivity geometry model of the human head for interpretation of neuromagnetic data. *IEEE Trans. Biomed. Eng.*, 36(2):165–171, 1989.

[10] Y. C. Okada, A. Lahteenmäki, and C. Xu. Experimental analysis of distortion of magnetoencephalography signals by the skull. *Clin. Neurophysiol.*, 110(2):230–238, 1999.

[11] D. Cohen. Magnetoencephalography: evidence of magnetic fields produced by alpha-rhythm currents. *Science*, 161(3843):784–786, 1968.

[12] F. London. *Superfluids: Macroscopic Theory of Superconductivity*. Dover, New York, 1961.

[13] B. D. Josephson. Possible new effects in superconductive tunnelling. *Phys. Lett.*, 1(7):251–253, 1962.

[14] R. C. Jaklevic, J. Lambe, A. H. Silver, and J. E. Mercereau. Quantum interference effects in Josephson tunneling. *Phys. Rev. Lett.*, 12(7):159–160, 1964.

[15] A. H. Silver and J. E. Zimmerman. Quantum transitions and loss in multiply connected superconductors. *Phys. Rev. Lett.*, 15(23):888–891, 1965.

[16] D. Cohen. Magnetoencephalography: detection of the brain's electrical activity with a superconducting magnetometer. *Science*, 175(4022):664–666, 1972.

[17] J. Vrba, J. Nenonen, and L. Trahms. Biomagnetism. In *The SQUID Handbook: Applications of SQUIDs and SQUID Systems, Volume II*, pages 269–389. Wiley-VCH, Weinheim, 2006.

[18] D. Cheyne, J. Vrba, D. Crisp, K. Betts, M. Burbank, T. Cheung, A. A. Fife, G. Haid, P. Kubik, S. Lee, J. McCubbin, J. McKay, D. McKenzie, P. Spear, B. Taylor, M. Tillotson, H. Weinberg, E. Basar, and T. Tsutada. Use of an unshielded, 64-channel whole-cortex MEG system in the study of normal and pathological brain function. *Proc. Satellite Symp. on Neuroscience and Technology*, pages 46–50, 1992.

[19] J. Vrba, K. Betts, M. Burbank, T. Cheung, A. A. Fife, G. Haid, P. R. Kubik, S. Lee, J. McCubbin, J. McKay, D. McKenzie, P. Spear, B. Taylor, M. Tillotson, D. Cheyne, and H. Weinberg. Whole cortex, 64 channel SQUID biomagnetometer system. *IEEE Trans. Appl. Supercond.*, 3(1):1878–1882, 1993.

[20] J. E. T. Knuutila, A. I. Ahonen, M. S. Hämäläinen, M. J. Kajola, P. P. Laine, O. V. Lounasmaa, L. T. Parkkonen, J. T. A. Simola, and C. D. Tesche. A 122-channel whole-cortex SQUID system for measuring the brain's magnetic fields. *IEEE Trans. Magn.*, 29(6):3315–3320, 1993.

[21] A. I. Ahonen, M. S. Hämäläinen, M. J. Kajola, J. E. T. Knuutila, P. P. Laine, O. V. Lounasmaa, L. T. Parkkonen, J. T. Simola, and C. D. Tesche. 122-channel SQUID instrument for investigating the magnetic signals from the human brain. *Phys. Scr.*, 1993(T49A):198–205, 1993.

[22] J. Clarke and A. I. Braginski. *The SQUID Handbook: Fundamentals and Technology of SQUIDs and SQUID Systems, Volume I.* Wiley-VCH, Weinheim, 2004.

[23] J. F. Schneiderman. Information content with low- vs. high-T_c SQUID arrays in MEG recordings: the case for high-T_c SQUID-based MEG. *J. Neurosci. Methods*, 222:42–46, 2014.

[24] J. Iivanainen, M. Stenroos, and L. Parkkonen. Measuring MEG closer to the brain: Performance of on-scalp sensor arrays. *Neuroimage*, 147:542–553, 2017.

[25] E. Boto, R. Bowtell, P. Krüger, T. M. Fromhold, P. G. Morris, S. S. Meyer, G. R. Barnes, and M. J. Brookes. On the potential of a new generation of magnetometers for MEG: a beamformer simulation study. *PLoS One*, 11(8):e0157655, 2016.

[26] E. Boto, S. S. Meyer, V. Shah, O. Alem, S. Knappe, P. Kruger, T. M. Fromhold, M. Lim, P. M. Glover, P. G. Morris, R. Bowtell, G. R. Barnes, and M. J. Brookes. A new generation of magnetoencephalography: Room temperature measurements using optically-pumped magnetometers. *Neuroimage*, 149:404–414, 2017.

[27] S. Ruffieux, M. Xie, M. Chukharkin, C. Pfeiffer, A. Kalabukhov, D. Winkler, and J. F. Schneiderman. Feedback solutions for low crosstalk in dense arrays of high-T_c SQUIDs for on-scalp MEG. *Supercond. Sci. Technol.*, 30:054006, 2017.

[28] M. Xie, J. F. Schneiderman, M. L. Chukharkin, A. Kalabukhov, B. Riaz, D. Lundqvist, S. Whitmarsh, M. Hämäläinen, V. Jousmäki, R. Oostenveld, and D. Winkler. Benchmarking for on-scalp MEG sensors. *IEEE Trans. Biomed. Eng.*, 64(6):1270–1276, 2017.

[29] L. M. Andersen, R. Oostenveld, C. Pfeiffer, S. Ruffieux, V. Jousmäki, M. Hämäläinen, J. F. Schneiderman, and D. Lundqvist. Similarities and differences between on-scalp and conventional in-helmet magnetoencephalography recordings. *PLoS One*, 12(7):e0178602, 2017.

[30] Y. Zhang, Y. Tavrin, M. Mück, A. I. Braginski, C. Heiden, S. Hampson, C. Pantev, and T. Elbert. Magnetoencephalography using high temperature rf SQUIDs. *Brain Topogr.*, 5(4):379–382, 1993.

[31] H.-J. Barthelmess, M. Halverscheid, B. Schiefenhovel, E. Heim, M. Schilling, and R. Zimmermann. Low-noise biomagnetic measurements with a multichannel dc-SQUID system at 77 K. *IEEE Trans. Appl. Supercond.*, 11(1):657–660, 2001.

[32] F. Öisjöen, J. F. Schneiderman, G. A. Figueras, M. L. Chukharkin, A. Kalabukhov, A. Hedström, M. Elam, and D. Winkler. High-T_c superconducting quantum interference device recordings of spontaneous brain activity: Towards high-T_c magnetoencephalography. *Appl. Phys. Lett.*, 100(13):132601, 2012.

[33] M. I. Faley, U. Poppe, R. E. Dunin-Borkowski, M. Schiek, F. Boers, H. Chocholacs, J. Dammers, E. Eich, N. J. Shah, A. B. Ermakov, V. Y. Slobodchikov, Y. V. Maslennikov, and V. P. Koshelets. High-T_c dc SQUIDs for magnetoencephalography. *IEEE Trans. Appl. Supercond.*, 23(3):1600705, 2013.

[34] J. Dammers, H. Chocholacs, E. Eich, F. Boers, M. Faley, R. E. Dunin-Borkowski, and N. J. Shah. Source localization of brain activity using helium-free interferometer. *Appl. Phys. Lett.*, 104(21):213705, 2014.

[35] M. I. Faley, J. Dammers, Y. V. Maslennikov, J. F. Schneiderman, D. Winkler, V. P. Koshelets, N. J. Shah, and R. E. Dunin-Borkowski. High-T_c SQUID biomagnetometers. *Supercond. Sci. Technol.*, 30:083001, 2017.

[36] H. Xia, A. Ben-Amar Baranga, D. Hoffman, and M. V. Romalis. Magnetoencephalography with an atomic magnetometer. *Appl. Phys. Lett.*, 89(21):211104, 2006.

[37] T. H. Sander, J. Preusser, R. Mhaskar, J. Kitching, L. Trahms, and S. Knappe. Magnetoencephalography with a chip-scale atomic magnetometer. *Biomed. Opt. Express*, 3(5):981–990, 2012.

[38] K. Kim, S. Begus, H. Xia, S.-K. Lee, V. Jazbinsek, Z. Trontelj, and M. V. Romalis. Multi-channel atomic magnetometer for magnetoencephalography: A configuration study. *Neuroimage*, 89:143–151, 2014.

[39] K. Kamada, D. Sato, Y. Ito, H. Natsukawa, K. Okano, N. Mizutani, and T. Kobayashi. Human magnetoencephalogram measurements using newly developed compact module of high-sensitivity atomic magnetometer. *Jpn. J. Appl. Phys.*, 54(2):026601, 2015.

[40] D. R. Glenn, K. Lee, H. Park, R. Weissleder, A. Yacoby, M. D. Lukin, H. Lee, R. L. Walsworth, and C. B. Connolly. Single cell magnetic imaging using a quantum diamond microscope. *Nat. Methods*, 12(8):736–738, 2015.

[41] W. P. Halperin. The impact of helium shortages on basic research. *Nat. Phys.*, 10(7):467–470, 2014.

[42] H. Weinstock, editor. *SQUID Sensors: Fundamentals, Fabrication, and Applications*. Kluwer, Dordrecht, 1996.

[43] D. Koelle, R. Kleiner, F. Ludwig, E. Dantsker, and J. Clarke. High-transition-temperature superconducting quantum interference devices. *Rev. Mod. Phys.*, 71(3):631–686, 1999.

[44] R. Dittmann and A. I. Braginski. Processing and manufacture of Josephson junctions. In *Handbook of Superconducting Materials*, pages 843–854. IOP Publishing, Bristol and Philadelphia, 2002.

[45] F. Ludwig, D. Koelle, E. Dantsker, D. T. Nemeth, A. H. Miklich, J. Clarke, and R. E. Thomson. Low noise $YBa_2Cu_3O_{7-x}$–$SrTiO_3$–$YBa_2Cu_3O_{7-x}$ multilayers for improved superconducting magnetometers. *Appl. Phys. Lett.*, 66(3):373–375, 1995.

[46] D. Drung, F. Ludwig, W. Müller, U. Steinhoff, L. Trahms, H. Koch, Y. Q. Shen, M. B. Jensen, P. Vase, T. Holst, T. Freltoft, and G. Curio. Integrated $YBa_2Cu_3O_{7-x}$ magnetometer for biomagnetic measurements. *Appl. Phys. Lett.*, 68(10):1421–1423, 1996.

[47] M. I. Faley, U. Poppe, K. Urban, D. N. Paulson, T. N. Starr, and R. L. Fagaly. Low noise HTS dc-SQUID flip-chip magnetometers and gradiometers. *IEEE Trans. Appl. Supercond.*, 11(1):1383–1386, 2001.

[48] D. Robbes. Highly sensitive magnetometers—a review. *Sens. Act. A, Phys.*, 129(1):86–93, 2006.

[49] J. Schneider, M. Mück, and R. Wördenweber. dc SQUIDs based upon $YBa_2Cu_3O_7$ nanobridges. *Appl. Phys. Lett.*, 65(19):2475–2477, 1994.

[50] D. H. A. Blank, W. Booij, H. Hilgenkamp, B. Vulink, D. Veldhuis, and H. Rogalla. $YBa_2Cu_3O_7$ nano-bridge junctions and dc SQUIDs made by focused ion beam milling. *IEEE Trans. Appl. Supercond.*, 5(2):2786–2789, 1995.

[51] M. V. Pedyash, D. H. A. Blank, and H. Rogalla. Superconducting quantum interference devices based on YBaCuO nanobridges. *Appl. Phys. Lett.*, 68(8):1156–1158, 1996.

[52] S. Nawaz, R. Arpaia, F. Lombardi, and T. Bauch. Microwave response of superconducting $YBa_2Cu_3O_{7-\delta}$ nanowire bridges sustaining the critical depairing current: Evidence of Josephson-like behavior. *Phys. Rev. Lett.*, 110(16):167004, 2013.

[53] Reza Baghdadi, Riccardo Arpaia, Sophie Charpentier, Dmitri Golubev, Thilo Bauch, and Floriana Lombardi. Fabricating nanogaps in $YBa_2Cu_3O_{7-\delta}$ for hybrid proximity-based Josephson junctions. *Phys. Rev. Appl*, 4(1):014022, 2015.

[54] R. Arpaia, M. Arzeo, S. Nawaz, S. Charpentier, F. Lombardi, and T. Bauch. Ultra low noise $YBa_2Cu_3O_{7-\delta}$ nano superconducting quantum interference devices implementing nanowires. *Appl. Phys. Lett.*, 104(7):072603, 2014.

[55] J. Nagel, K. B. Konovalenko, M. Kemmler, M. Turad, R. Werner, E. Kleisz, S. Menzel, R. Klingeler, B. Büchner, R. Kleiner, and D. Koelle. $YBa_2Cu_3O_7$ grain boundary junctions and low-noise superconducting quantum interference devices patterned by a focused ion beam down to 80 nm linewidth. *Supercond. Sci. Technol.*, 24:015015, 2011.

[56] T. Schwarz, R. Wölbing, C. F. Reiche, B. Müller, M. J. Martínez-Pérez, T. Mühl, B. Büchner, R. Kleiner, and D. Koelle. Low-noise $YBa_2Cu_3O_7$ nano-SQUIDs for performing magnetization-reversal measurements on magnetic nanoparticles. *Phys. Rev. Appl*, 3(4):044011, 2015.

[57] M. J. Martínez-Pérez, B. Müller, D. Schwebius, D. Korinski, R. Kleiner, J. Sesé, and D. Koelle. NanoSQUID magnetometry of individual cobalt

nanoparticles grown by focused electron beam induced deposition. *Supercond. Sci. Technol.*, 30:024003, 2017.

[58] M. Arzeo, R. Arpaia, R. Baghdadi, F. Lombardi, and T. Bauch. Toward ultra high magnetic field sensitivity $YBa_2Cu_3O_{7-\delta}$ nanowire based superconducting quantum interference devices. *J. Appl. Phys.*, 119(17):174501, 2016.

[59] M. B. Ketchen and J. M. Jaycox. Ultra-low-noise tunnel junction dc SQUID with a tightly coupled planar input coil. *Appl. Phys. Lett.*, 40(8):736–738, 1982.

[60] H. K. Onnes. The resistance of pure mercury at helium temperatures. *Commun. Phys. Lab. Univ. Leiden*, 12(120):1, 1911.

[61] J. G. Daunt, A. Horseman, and K. Mendelssohn. LXX. Thermodynamical properties of some supraconductors. *Phil. Mag.*, 27(185):754–764, 1939.

[62] J. Eisenstein. Superconducting elements. *Rev. Mod. Phys.*, 26(3):277–291, 1954.

[63] J. R. Waldram. *Superconductivity of Metals and Cuprates*. IOP Publishing, Bristol and Philadelphia, 1996.

[64] W. Meissner and R. Ochsenfeld. Ein neuer Effekt bei Eintritt der Supraleitfähigkeit. *Naturwiss.*, 21(44):787–788, 1933.

[65] F. London and H. London. The electromagnetic equations of the supraconductor. *Proc. R. Soc. London, Ser. A*, 149(866):71–88, 1935.

[66] M. Tinkham. *Introduction to Superconductivity*. McGraw-Hill, New York, 1996.

[67] V. L. Ginzburg and L. D. Landau. On the theory of superconductivity. *Zh. Eksp. Teor. Fiz.*, 20:1064–1082, 1950.

[68] J. Bardeen, L. N. Cooper, and J. R. Schrieffer. Theory of superconductivity. *Phys. Rev.*, 108(5):1175–1204, 1957.

[69] J. G. Bednorz and K. A. Müller. Possible high T_c superconductivity in the Ba-La-Cu-O system. *Z. Phys. B: Condens. Matter*, 64:189–193, 1986.

[70] M. K. Wu, J. R. Ashburn, C. J. Torng, P. H. Hor, R. L. Meng, L. Gao, Z. J. Huang, Y. Q. Wang, and C. W. Chu. Superconductivity at 93 K in a new mixed-phase Y-Ba-Cu-O compound system at ambient pressure. *Phys. Rev. Lett.*, 58(9):908–910, 1987.

[71] A. Schilling, M. Cantoni, J. D. Guo, and H. R. Ott. Superconductivity above 130 K in the Hg-Ba-Ca-Cu-O system. *Nature*, 363(6424):56–58, 1993.

[72] P. W. Anderson and J. M. Rowell. Probable observation of the Josephson superconducting tunneling effect. *Phys. Rev. Lett.*, 10(6):230–232, 1963.

[73] S. Shapiro. Josephson currents in superconducting tunneling: The effect of microwaves and other observations. *Phys. Rev. Lett.*, 11(2):80, 1963.

[74] D. E. McCumber. Effect of ac impedance on dc voltage-current characteristics of superconductor weak-link junctions. *J. Appl. Phys.*, 39(7):3113–3118, 1968.

[75] W. C. Stewart. Current-voltage characteristics of Josephson junctions. *Appl. Phys. Lett.*, 12(8):277–280, 1968.

[76] V. V. Schmidt. *The Physics of Superconductors: Introduction to Fundamentals and Applications*. Springer Science & Business Media, Berlin, 1997.

[77] C. D. Tesche and J. Clarke. dc SQUID: Noise and optimization. *J. Low Temp. Phys.*, 29(3-4):301–331, 1977.

[78] W.-T. Tsang and T. Van Duzer. dc analysis of parallel arrays of two and three Josephson junctions. *J. Appl. Phys.*, 46(10):4573–4580, 1975.

[79] K. Enpuku, G. Tokita, and T. Maruo. Inductance dependence of noise properties of a high-T_c dc superconducting quantum interference device. *J. Appl. Phys.*, 76(12):8180–8185, 1994.

[80] K. Enpuku, H. Doi, G. Tokita, and T. Maruo. Method for improving voltage modulation depth of high T_c dc SQUID with large inductance. *IEEE Trans. Appl. Supercond.*, 5(2):2762–2765, 1995.

[81] K. Enpuku, G. Tokita, T. Maruo, and T. Minotani. Parameter dependencies of characteristics of a high-T_c dc superconducting quantum interference device. *J. Appl. Phys.*, 78(5):3498–3503, 1995.

[82] V. Ambegaokar and B. I. Halperin. Voltage due to thermal noise in the dc Josephson effect. *Phys. Rev. Lett.*, 22(25):1364–1366, 1969.

[83] M. I. Faley, U. Poppe, K. Urban, and R. L. Fagaly. Noise analysis of dc SQUIDs with damped superconducting flux transformers. *J. Phys.: Conf. Ser*, 234(4):042009, 2010.

[84] R. H. Koch, J. Clarke, W. M. Goubau, J. M. Martinis, C. M. Pegrum, and D. J. van Harlingen. Flicker (1/f) noise in tunnel junction dc SQUIDS. *J. Low Temp. Phys.*, 51(1-2):207–224, 1983.

[85] V. Foglietti, W. J. Gallagher, M. B. Ketchen, A. W. Kleinsasser, R. H. Koch, S. I. Raider, and R. L. Sandstrom. Low-frequency noise in low 1/f noise dc SQUID's. *Appl. Phys. Lett.*, 49(20):1393–1395, 1986.

[86] D. Drung. High-T_c and low-T_c dc SQUID electronics. *Supercond. Sci. Technol.*, 16:1320–1336, 2003.

[87] M. J. Ferrari, M. Johnson, F. C. Wellstood, J. J. Kingston, T. J. Shaw, and J. Clarke. Magnetic flux noise in copper oxide superconductors. *J. Low Temp. Phys.*, 94(1):15–61, 1994.

[88] V. O. Kelhä, J. M. Pukki, R. S. Peltonen, A. J. Penttinen, R. J. Ilmoniemi, and J. J. Heino. Design, construction, and performance of a large-volume magnetic shield. *IEEE Trans. Magn.*, 18(1):260–270, 1982.

[89] J. Malmivuo, J. Lekkala, P. Kontro, L. Suomaa, and H. Vihinen. Improvement of the properties of an eddy current magnetic shield with active compensation. *J. Phys. E*, 20(2):151, 1987.

[90] H. J. M. Brake, Wieringa H. J., and H. Rogalla. Improvement of the performance of a mu-metal magnetically shielded room by means of active compensation (biomagnetic applications). *Meas. Sci. Technol.*, 2(7):596–601, 1991.

[91] H. J. M. Terbrake, R. Huonker, and H. Rogalla. New results in active noise compensation for magnetically shielded rooms. *Meas. Sci. Technol.*, 4(12):1370–1375, 1993.

[92] E. Dantsker, S. Tanaka, P.-Å. Nilsson, R. Kleiner, and J. Clarke. Reduction of 1/f noise in high-T_c dc superconducting quantum interference devices cooled in an ambient magnetic field. *Appl. Phys. Lett.*, 69(26):4099–4101, 1996.

[93] E. Dantsker, S. Tanaka, and J. Clarke. High-T_c super conducting quantum interference devices with slots or holes: Low 1/f noise in ambient magnetic fields. *Appl. Phys. Lett.*, 70(15):2037–2039, 1997.

[94] H.-M. Cho, Y. T. Andresen, J. Clarke, M. S. DiIorio, K.-Y. Yang, and S. Yoshizumi. Low-frequency noise in high-transition-temperature superconducting multilayer magnetometers in ambient magnetic fields. *Appl. Phys. Lett.*, 79(15):2438–2440, 2001.

[95] R. H. Koch, J. Z. Sun, V. Foglietta, and W. J. Gallagher. Flux dam, a method to reduce extra low frequency noise when a superconducting magnetometer is exposed to a magnetic field. *Appl. Phys. Lett.*, 67(5):709–711, 1995.

[96] P. Benzi, E. Bottizzo, and N. Rizzi. Oxygen determination from cell dimensions in YBCO superconductors. *J. Cryst. Growth*, 269(2):625–629, 2004.

[97] M. Matsuda, Y. Murayama, S. Kiryu, N. Kasai, S. Kashiwaya, M. Koyanagi, T. Endo, and S. Kuriki. Directly-coupled dc-SQUID magnetometers made of Bi-Sr-Ca-Cu oxide films. *IEEE Trans. Magn.*, 27(2):3043–3046, 1991.

[98] A. H. Miklich, D. Koelle, E. Dantsker, D. T. Nemeth, J. J. Kingston, R. F. Kromann, and J. Clarke. Bicrystal YBCO dc SQUIDs with low noise. *IEEE Trans. Appl. Supercond.*, 3(1):2434–2437, 1993.

[99] D. Koelle, A. H. Miklich, F. Ludwig, E. Dantsker, D. T. Nemeth, and J. Clarke. dc SQUID magnetometers from single layers of $YBa_2Cu_3O_{7-x}$. *Appl. Phys. Lett.*, 63(16):2271–2273, 1993.

[100] L. P. Lee, J. Longo, V. Vinetskiy, and R. Cantor. Low-noise$YBa_2Cu_3O_{7-\delta}$ direct-current superconducting quantum interference device magnetometer with direct signal injection. *Appl. Phys. Lett.*, 66(12):1539–1541, 1995.

[101] R. Cantor, L. P. Lee, M. Teepe, V. Vinetskiy, and J. Longo. Low-noise, single-layer $YBa_2Cu_3O_{7-x}$ dc SQUID magnetometers at 77 K. *IEEE Trans. Appl. Supercond.*, 5(2):2927–2930, 1995.

[102] J. Jaycox and M. Ketchen. Planar coupling scheme for ultra low noise dc SQUIDs. *IEEE Trans. Magn.*, 17(1):400–403, 1981.

[103] A. H. Miklich, J. J. Kingston, F. C. Wellstood, J. Clarke, M. S. Colclough, K. Char, and G. Zaharchuk. Sensitive $YBa_2Cu_3O_{7-x}$ thin-film magnetometer. *Appl. Phys. Lett.*, 59(8):988–990, 1991.

[104] E. Dantsker, F. Ludwig, R. Kleiner, J. Clarke, M. Teepe, L. P. Lee, N. McN. Alford, and T. Button. Addendum: "Low noise $YBa_2Cu_3O_{7-x}$–$SrTiO_3$–$YBa_2Cu_3O_{7-x}$ multilayers for improved superconducting magnetometers" [Appl. Phys. Lett. 66, 373 (1995)]. *Appl. Phys. Lett.*, 67(5):725–726, 1995.

[105] M. I. Faley, S. B. Mi, C. L. Jia, U. Poppe, K. Urban, and R. L. Fagaly. Epitaxial thick film high-T_c SQUIDs. *J. Phys. Conf. Ser.*, 97(1):012164, 2008.

[106] R. Scharnweber and M. Schilling. A new concept for integrated $YBa_2Cu_3O_7$ magnetometers. *IEEE Trans. Appl. Supercond.*, 7(2):3485–3488, 1997.

[107] F. Ludwig, E. Dantsker, D. Koelle, R. Kleiner, A. H. Miklich, and J. Clarke. Multilayer magnetometers based on high-T_c SQUIDs. *Appl. Supercond.*, 3(7-10):383–398, 1995.

[108] R. Gross, P. Chaudhari, M. Kawasaki, M. B. Ketchen, and A. Gupta. Low noise $YBa_2Cu_3O_{7-\delta}$ grain boundary junction dc SQUIDs. *Appl. Phys. Lett.*, 57(7):727–729, 1990.

[109] J. Beyer, D. Drung, F. Ludwig, T. Minotani, and K. Enpuku. Low-noise $YBa_2Cu_3O_{7-x}$ single layer dc superconducting quantum interference device (SQUID) magnetometer based on bicrystal junctions with 30° misorientation angle. *Appl. Phys. Lett.*, 72(2):203–205, 1998.

[110] H. Hilgenkamp and J. Mannhart. Grain boundaries in high-T_c superconductors. *Rev. Mod. Phys.*, 74(2):485–549, 2002.

[111] L. G. Aslamazov and A. I. Larkin. Josephson effect in wide superconducting bridges. *Sov. Phys. JETP*, 41:381–386, 1975.

[112] K. K. Likharev. Superconducting weak links. *Rev. Mod. Phys.*, 51(1):101–159, 1979.

[113] A. A. Golubov, M. Y. Kupriyanov, and E. Il'ichev. The current-phase relation in Josephson junctions. *Rev. Mod. Phys.*, 76(2):411–469, 2004.

[114] L. N. Bulaevskii, M. J. Graf, C. D. Batista, and V. G. Kogan. Vortex-induced dissipation in narrow current-biased thin-film superconducting strips. *Phys. Rev. B*, 83(14):144526, 2011.

[115] T. Van Duzer and C. W. Turner. *Principles of Superconductive Devices and Circuits*. Prentice Hall, Upper Saddle River, 1999.

[116] C. H. Wu, Y. T. Chou, W. C. Kuo, J. H. Chen, L. M. Wang, J. C. Chen, K. L. Chen, U. C. Sou, H. C. Yang, and J. T. Jeng. Fabrication and characterization of high-T_c $YBa_2Cu_3O_{7-x}$ nanoSQUIDs made by focused ion beam milling. *Nanotechnology*, 19(31):315304, 2008.

[117] M. Chukharkin, A. Kalabukhov, J. F. Schneiderman, F. Öisjöen, M. Jönsson, M. Xie, O. V. Snigirev, and D. Winkler. Improvement of ultra-low field magnetic resonance recordings with a multilayer flux-transformer-based high-T_c SQUID magnetometer. *IEEE Trans. Appl. Supercond.*, 23(3):1602704, 2013.

[118] E. H. Brandt and J. R. Clem. Superconducting thin rings with finite penetration depth. *Phys. Rev. B*, 69(18):184509, 2004.

[119] E. H. Brandt. Thin superconductors and SQUIDs in perpendicular magnetic field. *Phys. Rev. B*, 72(2):024529, 2005.

[120] N. Curtz, E. Koller, H. Zbinden, M. Decroux, L. Antognazza, Ø. Fischer, and N. Gisin. Patterning of ultrathin YBCO nanowires using a new focused-ion-beam process. *Supercond. Sci. Technol.*, 23:045015, 2010.

[121] A. A. O. Elkaseh, W. J. Perold, and V. V. Srinivasu. Josephson nanoconstrictions made by AFM plowing of $YBa_2Cu_3O_{7-x}$ films. *J. Appl. Phys.*, 108(5):053914, 2010.

[122] G. Papari, F. Carillo, D. Born, L. Bartoloni, E. Gambale, D. Stornaiuolo, P. Pingue, F. Beltram, and F. Tafuri. YBCO nanobridges: simplified fabrication process by using a Ti hard mask. *IEEE Trans. Appl. Supercond.*, 19(3):183–186, 2009.

[123] K. Kajino, T. Kimura, Y. Horii, M. Watanabe, M. Inoue, and A. Fujimaki. Preparation of narrowed $YBa_2Cu_3O_{7-x}$ nanobridges down to 30 nm with reduced degradation. *IEEE Trans. Appl. Supercond.*, 19(3):178–182, 2009.

[124] R. Arpaia, S. Nawaz, F. Lombardi, and T. Bauch. Improved nanopatterning for YBCO nanowires approaching the depairing current. *IEEE Trans. Appl. Supercond.*, 23(3):1101505, 2013.

[125] S. Nawaz, R. Arpaia, T. Bauch, and F. Lombardi. Approaching the theoretical depairing current in $YBa_2Cu_3O_{7-x}$ nanowires. *Physica C*, 495:33–38, 2013.

[126] M. M. Khapaev, A. Y. Kidiyarova-Shevchenko, P. Magnelind, and M. Y. Kupriyanov. 3D-MLSI: Software package for inductance calculation in multilayer superconducting integrated circuits. *IEEE Trans. Appl. Supercond.*, 11(1):1090–1093, 2001.

[127] M. M. Khapaev. Extraction of inductances of plane thin film superconducting circuits. *Supercond. Sci. Technol.*, 10(6):389–394, 1997.

[128] M. M. Khapaev. Inductance extraction of multilayer finite-thickness superconductor circuits. *IEEE Trans. Microw. Theory Techn.*, 49(1):217–220, 2001.

[129] M. M. Khapaev. Extraction of inductances of a multi-superconductor transmission line. *Supercond. Sci. Technol.*, 9(9):729–733, 1996.

[130] C. Del Gratta, V. Pizzella, F. Tecchio, and G. L. Romani. Magnetoencephalography - a noninvasive brain imaging method with 1 ms time resolution. *Rep. Prog. Phys.*, 64(12):1759–1814, 2001.

[131] H. Berger. Über das Electrenphalogramm des Menschen. *Arch. Physchiatr. Nervenkr.*, 87:527–570, 1929.

[132] S. A. Huettel, Song A. W., and G. McCarthy. *Functional Magnetic Resonance Imaging*. Sinauer Associates, Sunderland, 2004.

[133] D. Budker and M. V. Romalis. Optical magnetometry. *Nat. Phys.*, 3:227–234, 2007.

[134] J. M. Taylor, P. Cappellaro, L. Childress, L. Jiang, D. Budker, P. R. Hemmer, A. Yacoby, R. Walsworth, and M. D. Lukin. High-sensitivity diamond magnetometer with nanoscale resolution. *Nat. Phys.*, 4(10):810–816, 2008.

[135] M. Pannetier, C. Fermon, G. Le Goff, J. Simola, and E. Kerr. Femtotesla magnetic field measurement with magnetoresistive sensors. *Science*, 304(5677):1648–1650, 2004.

[136] J. Luomahaara, V. Vesterinen, L. Grönberg, and J. Hassel. Kinetic inductance magnetometer. *Nat. Commun.*, 5(4872):1–7, 2014.

[137] B. Riaz, C. Pfeiffer, and J. F. Schneiderman. Evaluation of realistic layouts for next generation on-scalp MEG: spatial information density maps. *Sci. Rep.*, 7(1):6974, 2017.

[138] J. Sarvas. Basic mathematical and electromagnetic concepts of the biomagnetic inverse problem. *Phys. Med. Biol.*, 32(1):11–22, 1987.

[139] B. Lutkenhoner. Current dipole localization with an ideal magnetometer system. *IEEE Trans. Biomed. Eng.*, 43(11):1049–1061, 1996.

[140] C. S. Lessard, H.-i Wu, and J. Winston. Localization of current dipole within a sphere by magnetic measurements. *Comput. Methods Programs Biomed.*, 20(1):45–49, 1985.

[141] A. Delorme and S. Makeig. EEGLAB: an open source toolbox for analysis of single-trial EEG dynamics including independent component analysis. *Journal of neuroscience methods*, 134(1):9, 2004.

[142] R. Oostenveld, P. Fries, E. Maris, and J.-M. Schoffelen. FieldTrip: open source software for advanced analysis of MEG, EEG, and invasive electrophysiological data. *Comput. Intell. Neurosci.*, 2011(156869):1, 2011.

[143] R. J. Ilmoniemi, M. S. Hämäläinen, and J. E. Knuutila. The forward and inverse problems in the spherical model. In H. Weinberg, G. Stroink, and T. Katila, editors, *Biomagnetism: Applications and Theory*, pages 278–282. Pergamon, New York, 1985.